This is to certify that the

thesis entitled

TRANSPORT PROPERTIES OF Cd AND W, $Ti_{1+x}S_2$,

AND Al AT LOW TEMPERATURES

presented by

BRENT J. BLUMENSTOCK

has been accepted towards fulfillment
of the requirements for

PhD degree in Physics

Major professor

Date 10/13/80

TRANSPORT PROPERTIES OF Cd AND W, $Ti_{1+x}S_2$, AND Al AT LOW TEMPERATURES

by

Brent J. Blumenstock

A DISSERTATION

Submitted to
Michigan State University
in partial fulfillment of the requirements
for the degree of

Doctor of Philosophy

Department of Physics

1980

gatio

therm

Hall

elect

singl

direc

in W.

sepa

from

from

term

magn

high

in t

ABSTRACT

TRANSPORT PROPERTIES OF Cd AND W, $Ti_{1+x}S_2$,
AND Al AT LOW TEMPERATURES

by

Brent J. Blumenstock

This thesis reports on several very different experimental investigations of low temperature transport properties of solids--the magneto-thermopower of Cd and W single crystals, the electrical resistivity, Hall coefficient and magnetoresistivity of crystalline $Ti_{1+x}S_2$, and the electrical resistivity of polycrystalline Al.

Measurements were made of the magnetothermopower S^a of Cd and W single crystals between 1.5 and 4.2 K in magnetic fields up to 50 kG directed along the (0001) direction in Cd and along the (100) direction in W.

The results did not obey the form $S^a = aT + bT^3$ which prevented a separation of the diffusion from the phonon drag thermopower contributions from being made.

The component ε_{xx} of the thermoelectric tensor for W, derivable from these S^a measurements, was found to be consistent with theory in terms of its temperature and magnetic field dependence.

At the lowest temperatures, S^a showed no sign of saturating in magnetic fields up to our limiting field of 50 kG as was expected from high field semi-classical theory. This apparent discrepancy is resolved in this thesis where a re-examination of the theory reveals that it had

been

fiel

depe

exam

stre

coef

x < (

using

with

is co

is th

deper

was f

chiom

sampl

at lo

Blocn

scatt

regim

the n

at low

(

reveal

over t

been misinterpreted. The result is that for metals in large magnetic fields directed along a high symmetry direction, the magnetic field dependence of the individual elements of the transport tensors (for example σ_{yx}) can contain both even and odd powers of the magnetic field strength B.

Measurements were made of the electrical resistivity, the Hall coefficient and the magnetoresistance of $Ti_{1+x}S_2$ single crystals with $x < 0.06$ over the temperature range of 1.5 to 100 K.

The carrier concentration n, derived from our Hall coefficient data using a single carrier model, was found to increase slightly (~3-10%) with decreasing temperature.

The residual resistivity $\rho(T=0)$ was found to vary as $n^{1/3}$ which is consistent with the idea that the source of the carriers in $Ti_{1+x}S_2$ is the excess Ti atoms.

In contrast to the higher temperature data where the temperature dependent part of the resistivity, defined as $\rho_1(T) = \rho(T) - \rho(T=0)$, was found to vary as T^m where m increases from 1.85 to 2.3 as the stoichiometry of the samples increase, $\rho_1(T)$ was found to vary as T^3 for all samples below ~30 K. A temperature dependence higher than T^2 is expected at low temperatures due to electron-phonon scattering but the simple Bloch-Grüneisen theory predicts T^5 not T^3. Simple electron-phonon scattering is also not consistent with the fact that ρ_1, in the T^3 regime, was found to vary as $n^{-0.46}$. The mechanism(s) responsible for the nominal T^2 dependence at higher temperatures or for the T^3 dependence at lower temperatures remain unknown.

Our preliminary magnetoresistance studies of these $Ti_{1+x}S_2$ systems reveal that the magnetoresistance is largely temperature independent over this temperature range and is strongly sample dependent.

cryst

lorgi

ducti

seen

exten

is fo

Measurements were made of the electrical resistivity of a polycrystalline Al sample over the temperature range of ~0.08 to 4.2 K using longitudinal magnetic fields up to ~300 Gauss to destroy the superconducting state. Our results indicate that the T^2 temperature dependence seen in Al, which has been attributed to electron-electron scattering, extends down to ~0.2 K. The magnetic field dependence of this T^2 behavior is found to be negative.

and f

ness

runs

stude

the n

like

stat

and W

am a

disc

disc

Carl

Steve

Heinz

and

Grate

ACKNOWLEDGMENTS

It is a pleasure to thank Prof. Peter Schroeder for his guidance and friendship throughout the course of my graduate study. His willingness to make personal sacrifices in order to participate in experimental runs is greatly appreciated.

I would like to formally thank the faculty, staff, and graduate students of the Michigan State University Physics Department for all the help they have given me during my stay. More specifically, I would like to thank Mr. Richard Hoskins for his fine job of building my cryostat and Ms. Delores Sullivan for typing this manuscript.

I would like to thank Prof. Robin Fletcher for the use of his Cd and W crystals and for his help in their experimental preparation. I am also thankful to Dr. Fred Kus and Prof. Carl Foiles for many useful discussions concerning the field reversal problems of the LAK theory discussed in this thesis.

For the use of the $Ti_{1+x}S_2$ crystals I would like to thank Drs. Carl Kukkonen, William Kaisser, and Theros Logothetis at Ford Motor Co.

For my Al studies, I wish to thank Prof. William Pratt and Dr. Steven Steenwyk for permitting me to use their cryostats, Mr. Vern Heinen for his help in preparing and operating the dilution refrigerator, and Dr. John Rowlands for designing and winding the solenoid.

The financial support of the National Science Foundation is gratefully acknowledged.

appre

oppor

given

Finally, although this medium is woefully inadequate to express my appreciation for everything she has done, I would like to take this opportunity to publically thank my wife, Carol, for the support she has given me throughout my graduate study.

TABLE OF CONTENTS

APPEN

REFER

LIST OF TABLES

Figures

LIST OF FIGURES

Figu

F1

F2

F3

F4

G1

G2

G3

G4

G5

G6

G7

G8

1. INT

Th

section

thermop

4.2 K i

our inv

resisti

x < 0.0

results

talline

Appendi

Th

thermop

Opsal a

magneti

of Lifs

At

directi

CHAPTER I

Cd AND W

1. INTRODUCTION

This thesis is divided into two principle sections. In the first section we report the results of our investigation of the magneto-thermopower of Cd and W single crystals at temperatures between 1.5 and 4.2 K in transverse magnetic fields up to 50 kG. Section II reports on our investigation of the electrical resistivity, the transverse magneto-resistivity, and the Hall coefficient of $Ti_{1+x}S_2$ single crystals for $x < 0.06$ over the temperature range of 1.5 to 100 K. The preliminary results of our investigation of the electrical resistivity of polycrystalline Al over the temperature range of 0.08 to 4 K are reported in Appendix G.

The work on Cd and W was instigated as a result of the magneto-thermopower S^a measurements made on a single crystal of Mo by Fletcher, Opsal and Thaler[1] which showed that S^a failed to saturate in large magnetic fields as predicted using the high field semi-classical theory of Lifshitz, Azbel and Kaganov--the LAK theory.[2,3]

At low temperatures, with the magnetic field along a high symmetry direction, the thermopower in Mo, to a good approximation, is given by

$$S^a \simeq -\rho_{xx}\varepsilon_{xx} + 2\rho_{yx}\varepsilon_{yx} \qquad (1.1)$$

where the transport tensors $\overleftrightarrow{\rho}$ and $\overleftrightarrow{\varepsilon}$ are defined by

$$\vec{J} = \overleftrightarrow{\sigma}\vec{E} + \overleftrightarrow{\varepsilon}\nabla T \tag{1.2}$$

and

$$\overleftrightarrow{\rho} = \overleftrightarrow{\sigma}^{-1} \tag{1.3}$$

For a compensated metal with the magnetic field oriented so that the electron orbits are closed, the LAK theory predicts, to leading order in the magnetic field strength B, that $\rho_{xx} \sim B^2$, $\rho_{yx} \sim B$, $\varepsilon_{xx} \sim 1/B^2$ and $\varepsilon_{yx} \sim 1/B$ which imply, using Equation (1.1), that S^a for Mo should become independent of the magnetic field as the field gets large. However, Fletcher et al. found that S^a did not saturate for their Mo crystal up to their largest obtainable field of 21 kG but instead was increasing rapidly. They argued that this non-saturating behavior was due to the fact that in real systems, perfect compensation can never be achieved due to unavoidable imperfections at some level. Arising from any noncompensation, the LAK theory predicts that ρ_{yx} contains a term which depends upon the cube of the magnetic field strength, that is, $\rho_{yx} \sim aB^1 + bB^3$ and so, no matter how well compensation is achieved (small b), ρ_{yx} will always have a limiting B^3 behavior at sufficiently high fields. Thus the term $\rho_{yx}\varepsilon_{yx}$ contributes a power of B^2 to S^a which accounts for the non-saturating behavior seen in the Mo crystal whose degree of compensation was estimated to be ~0.01%. Because this apparent reconciliation between experiment and theory is critically dependent upon the validity of this argument, we thought it desirable to measure the magnetothermopower of other compensated systems to see if this argument continues to apply.

Cadmium and tungsten were chosen because two single crystals became available to use courtesy of R. Fletcher who had previously made several

tran

to t

S^a d

Cd a

"pur

RRR =

while

purit

tion

at fi

the c

(a fi

study

streng

2. G

I

$\vec{U}$ resp

and

where $\vec{E}$

perature

have bee

transport measurements on them.[4,5,6] These measurements were essential to the analysis of our S^a data and also became, with the addition of our S^a data, a complete set of the transverse transport properties of these Cd and W crystals. The samples had the added benefit of being much "purer" then the Mo sample--the residual resistance ratio RRR = $\rho(300\ K)/\rho(4.2\ K)$ of these Cd and W crystals were nearly 40,000 while the RRR of the Mo sample was ~5,000. Because of their higher purity these crystals should have achieved a higher degree of compensation and thus, one should expect to see saturating behavior in their S^a at fields comparable to those used in the Mo study. And, because we had the capability of making measurements in magnetic fields up to 50 kG (a field 2½ times larger than the largest obtainable fields in the Mo study) we could test the LAK theory over a much larger range of field strengths.

2. GENERAL TRANSPORT

In linear response theory the electrical and heat currents, $\vec{J}$ and $\vec{U}$ respectively, can be expressed in terms of the applied fields as

$$\vec{J} = \overleftrightarrow{\sigma}\vec{E} + \overleftrightarrow{\varepsilon}\nabla T \tag{2.1a}$$

and

$$\vec{U} = -\overleftrightarrow{\pi}\vec{E} - \overleftrightarrow{\lambda}\nabla T \tag{2.1b}$$

where $\vec{E}$ is the electric field vector and ∇T is the gradient of the temperature. The various transport coefficients involved in Equation (2.1) have been given specific names:

$\overleftrightarrow{\varepsilon}$ is the thermoelectric tensor
$\overleftrightarrow{\sigma}$ is the electrical conductivity

$\overleftrightarrow{\pi}$ is the Peltier tensor

and $\overleftrightarrow{\lambda}$ is the thermal conductivity.

Generally these coefficients are tensors of second rank, each tensor consisting of nine elements. This large number of parameters characterizing a particular system can be reduced to a more manageable level by applying symmetry operations. Because W crystallizes into a bcc lattice, its tensors reduce to scalars; Cd has a hexagonal structure and so its tensors reduce to the form

$$\begin{bmatrix} \Sigma_{xx} & 0 & 0 \\ 0 & \Sigma_{xx} & 0 \\ 0 & 0 & \Sigma_{zz} \end{bmatrix} \tag{2.2}$$

where the z-axis is chosen along the c-axis of the crystal.

When a magnetic field is applied these simplifications are no longer valid because the field reduces the symmetry by forcing a reference direction (the field direction) on to the system. In a magnetic field we can still simplify the transport tensors in Equation (2.1) provided the field is along a crystal symmetry direction. As shown in Appendix A, if the field is applied along a 3-, 4-, or 6-fold symmetry axis (taken as the z-axis), then the transport tensors are of the form

$$\begin{bmatrix} \Sigma_{xx} & \Sigma_{xy} & 0 \\ -\Sigma_{xy} & \Sigma_{xx} & 0 \\ 0 & 0 & \Sigma_{zz} \end{bmatrix} \tag{2.3}$$

Thus each tensor consists of only three different elements. The magnetic fields used in this study were along the [0001] and the [001] directions of the Cd and W crystals respectively, so Equation (2.3) can be used.

We have thus reduced the total number of transport tensor elements down from 36 to 12, which can be reduced further because $\overleftrightarrow{\pi}$ and $\overleftrightarrow{\varepsilon}$ are not independent but are related through the Onsager relations (Onsager 1931). As discussed by Ziman,[7] the Onsager relations pertinent to the discussion are

$$\sigma_{ij}(\vec{B}) = \sigma_{ji}(-\vec{B}) \tag{2.4a}$$

$$\lambda_{ij}(\vec{B}) = \lambda_{ji}(-\vec{B}) \tag{2.4b}$$

$$\varepsilon_{ij}(\vec{B}) = \pi_{ji}(-\vec{B})/T \tag{2.4c}$$

Thus there are only nine independent elements corresponding to the three transport tensors $\overleftrightarrow{\sigma}$, $\overleftrightarrow{\lambda}$ and $\overleftrightarrow{\varepsilon}$ which characterize these Cd and W crystals.

From an experimental point of view, Equation (2.1) is not very convenient because it is much more difficult to control the fields ∇T and $\vec{E}$ than it is to control the currents $\vec{J}$ and $\vec{U}$. Thus it is more useful to express the fields as functions of the currents as

$$\vec{E} = \overleftrightarrow{\rho}' \vec{J} - \overleftrightarrow{\varepsilon}' \vec{U} \tag{2.5a}$$

and

$$\nabla T = -\overleftrightarrow{\pi}' \vec{J} - \overleftrightarrow{V}' \vec{U} \tag{2.5b}$$

using a new set of transport coefficients which are more easily measurable in principle. For example, by sending an electric current along the sample ($\vec{J} = J\vec{x}$) with no heat flowing ($\vec{U} = 0$), ρ'_{xx} is determined by measuring the induced voltage drop ΔV along the sample of length Δx using

$$\rho'_{xx} = E_x/J_x \tag{2.6}$$

or

$$\rho'_{xx} \approx -\frac{\Delta V}{I}\frac{A}{\Delta x} \tag{2.7}$$

where the total current I = JA and A is the cross sectional area of the sample.

There is no new physics in these resistivity tensors of Equation (2.5); Equation (2.1) has simply been rewritten. After a little algebra it can be shown that

$$\overleftrightarrow{\rho}'^{-1} = \overleftrightarrow{\sigma} + \overleftrightarrow{\varepsilon}\,\overleftrightarrow{\lambda}^{-1}\,\overleftrightarrow{\pi} \tag{2.8a}$$

$$\overleftrightarrow{\gamma}'^{-1} = \overleftrightarrow{\lambda} + \overleftrightarrow{\pi}\,\overleftrightarrow{\sigma}^{-1}\,\overleftrightarrow{\varepsilon} \tag{2.8b}$$

$$\overleftrightarrow{\varepsilon}'^{-1} = -\overleftrightarrow{\pi} - \overleftrightarrow{\lambda}\,\overleftrightarrow{\varepsilon}^{-1}\,\overleftrightarrow{\sigma} \tag{2.8c}$$

$$\overleftrightarrow{\pi}'^{-1} = -\overleftrightarrow{\varepsilon} - \overleftrightarrow{\sigma}\,\overleftrightarrow{\pi}^{-1}\,\overleftrightarrow{\lambda} \tag{2.8d}$$

where the $^{-1}$ represents the tensor inverse $\overleftrightarrow{\lambda}\,\overleftrightarrow{\lambda}^{-1} = 1$. Equation (2.8) can be inverted to find

$$\overleftrightarrow{\sigma}^{-1} = \overleftrightarrow{\rho}' + \overleftrightarrow{\varepsilon}'\,\overleftrightarrow{\gamma}'^{-1}\,\overleftrightarrow{\pi}' \tag{2.9a}$$

$$\overleftrightarrow{\lambda}^{-1} = \overleftrightarrow{\gamma}' + \overleftrightarrow{\pi}'\,\overleftrightarrow{\rho}'^{-1}\,\overleftrightarrow{\varepsilon}' \tag{2.9b}$$

$$\overleftrightarrow{\varepsilon}^{-1} = -\overleftrightarrow{\pi}' - \overleftrightarrow{\gamma}'\,\overleftrightarrow{\varepsilon}'^{-1}\,\overleftrightarrow{\rho}' \tag{2.9c}$$

$$\overleftrightarrow{\pi}^{-1} = -\overleftrightarrow{\varepsilon}' - \overleftrightarrow{\rho}'\,\overleftrightarrow{\pi}'^{-1}\,\overleftrightarrow{\gamma}' \tag{2.9d}$$

From Equation (2.9) it is easily seen that a lot of experimental work and number manipulation would have to be done in order to compare experiment with theory. All nine parameters, corresponding to the three independent resistivity tensors $\overleftrightarrow{\rho}'$, $\overleftrightarrow{\varepsilon}'$, and $\overleftrightarrow{\gamma}'$ each having three elements, would have to be determined and the algebra indicated by Equation (2.9) to be performed before the result could be compared to a theoretical calculation of a conductivity. Fortunately a significant

amount of this work can be avoided because some of the terms in Equation (2.9) are small for these Cd and W crystals.

It is relatively straightforward to experimentally determine $\overleftrightarrow{\sigma}$ and $\overleftrightarrow{\lambda}$ by measuring the adiabatic (no heat flow) electrical resistivity $\overleftrightarrow{\rho}'$ and the thermal resistivity $\overleftrightarrow{\gamma}'$ because the thermoelectric correction terms $\overleftrightarrow{\varepsilon}'$, $\overleftrightarrow{\gamma}'^{-1}\overleftrightarrow{\pi}'$ and $\overleftrightarrow{\pi}'$, $\overleftrightarrow{\rho}'^{-1}\overleftrightarrow{\varepsilon}'$ are generally small, ($\lesssim 1\%$ for these Cd and W crystals) which implies that

$$\overleftrightarrow{\sigma}^{-1} = \overleftrightarrow{\rho} \approx \overleftrightarrow{\rho}' \tag{2.10a}$$

and

$$\overleftrightarrow{\lambda}^{-1} = \overleftrightarrow{\gamma} \approx \overleftrightarrow{\gamma}' \tag{2.10b}$$

The thermoelectric tensor $\overleftrightarrow{\varepsilon}$ can be determined from measurements of the Nernst-Ettinghausen coefficient and the thermopower defined as

$$Q^a = -E_y/(\partial T/\partial x) \tag{2.11}$$

and

$$S^a = E_x/(\partial T/\partial x)$$

respectively, subject to the condition of no electrical current flowing ($\vec{J} = 0$). The superscript a represents the adiabatic condition of U_y, $U_z = 0$. Under these conditions Equation (2.1a) becomes

$$\vec{E} = -\overleftrightarrow{\rho}\,\overleftrightarrow{\varepsilon}\,\nabla T \tag{2.13}$$

which implies that

$$Q^a = \rho_{yx}\varepsilon_{xx} - \rho_{xx}\varepsilon_{yx} - (\gamma_{yx}/\gamma_{xx})(\rho_{xx}\varepsilon_{xx}+\rho_{yx}\varepsilon_{yx}) \tag{2.14}$$

and

$$S^a = -\rho_{xx}\varepsilon_{xx} + \rho_{yx}\varepsilon_{yx} + (\gamma_{yx}/\gamma_{xx})(\rho_{xx}\varepsilon_{yx}+\rho_{yx}\varepsilon_{xx}) \tag{2.15}$$

Thus values for ε_{yx} and ε_{xx} can be extracted from measurements of Q^a and S^a provided ρ_{xx}, ρ_{yx}, γ_{xx}, and γ_{yx} are known. Actually the situation is much better in determing ε_{yx} because for compensated metals

$$\rho_{yx} << \rho_{xx} \tag{2.16}$$

$$\gamma_{yx} << \gamma_{xx} \tag{2.17}$$

and

$$\varepsilon_{yx} >> \varepsilon_{xx} \tag{2.18}$$

which means that

$$Q^a \approx \rho_{xx}\varepsilon_{yx} \tag{2.19}$$

Boltzmann Formulation

The various transport tensors in Equation (2.1) can be evaluated using semi-classical transport theory based upon the Boltzmann transport equation. We will assume that the many body conduction electron problem in a crystalline solid has already been solved for the quasi-particle eigenstates $\psi_{\vec{k}}(\vec{r})$ where, as discussed by Ziman,[7] each eigenstate is characterized by a wave vector $\vec{k}$ whose allowed values form a discrete spectrum in reciprocal space. For each $\vec{k}$ value a range of energy eigenvalues $\varepsilon_n(\vec{k})$ are possible where n labels the band index. Each electronic state is uniquely described by $\vec{k}$, n and the electronic spin. (Hereafter the band index will not be written explicitly.) The crystal momentum $\hbar\vec{k}$ of an electron in state $\vec{k}$ responds to an external

force

where

where

F

descri

distri

phase

spatia

solid.

$d\vec{k}\ d\vec{r}$

distri

velocit

scatter

Boltzma

Under s

equation

force $\vec{F}$ as

$$\hbar\dot{\vec{k}} = \vec{F} \tag{2.20}$$

where $\dot{\vec{k}} = d\vec{k}/dt$. The velocity of the electron is

$$\vec{v} = \nabla_k \varepsilon(\vec{k})/\hbar \tag{2.21}$$

where ∇_k is the gradient operator in reciprocal space

$$\text{i.e.} \quad \frac{\partial}{\partial k_x}\hat{x} + \frac{\partial}{\partial k_y}\hat{y} + \frac{\partial}{\partial k_z}\hat{z} \ .$$

Following Blatt,[8] the conduction electrons are describable using a statistical scheme in terms of a probability distribution function $f(\vec{k},\vec{r},t)$ where the number of electrons in the phase space element $d\vec{k}\ d\vec{r}$ is defined to be $f(\vec{k},\vec{r},t)\ d\vec{k}\ d\vec{r}/4\pi^3$. The spatial dependence allows for temperature non-uniformity throughout the solid. Since the number of electrons in a small volume of phase space $d\vec{k}\ d\vec{r}$ changes not only because of an explicit time dependence in the distribution function $(\partial f/\partial t)$, but also because of the electron's velocity $(\vec{v})$, the influence of external forces $(\hbar\dot{\vec{k}})$, and because of scattering events $(\partial f/\partial t)_c$, the distribution function obeys the Boltzmann equation

$$\frac{df}{dt} = -\dot{\vec{k}}\cdot\nabla_k f - \vec{v}\cdot\nabla f + \frac{\partial f}{\partial t} + \partial f/\partial t)_c \tag{2.22}$$

Under steady-state conditions with time independent forces the Boltzmann equation reduces to

$$\dot{\vec{k}}\cdot\nabla_k f(\vec{k},\vec{r}) + \vec{v}\cdot\nabla f(\vec{k},\vec{r}) = \partial f/\partial t)_c \tag{2.23}$$

At thermal equilibrium $f(\vec{k},\vec{r})$ becomes equal to the Fermi-Dirac distribution

$$f^0(\vec{k},\vec{r}) = \left(1 + e^{(\varepsilon-\mu(\vec{r}))/k_B T}\right)^{-1} \tag{2.24}$$

where μ is the chemical potential and k_B is Boltzmann's constant. With an applied Lorentz force of

$$\vec{F} = -e(\vec{E} + \vec{v}\times\vec{B}/c) \tag{2.25}$$

Equation (2.23) can be written in a more useful form in terms of the deviation in the distribution function from its equilibrium value

$$g(\vec{k},\vec{r}) = f(\vec{k},\vec{r}) - f^0(\vec{k},\vec{r}) \tag{2.26}$$

as

$$\partial f/\partial t)_c + \frac{e}{\hbar}\left(\frac{\vec{v}}{c}\times\vec{B}\right)\cdot\nabla_k g \simeq -\frac{\partial f^0}{\partial \varepsilon}\vec{v}\cdot\left(e\vec{E}_{eff} + \frac{(\varepsilon-\mu)}{T}\nabla T\right) \tag{2.27}$$

where

$$\vec{E}_{eff} = \vec{E} + \nabla\mu/e \tag{2.28}$$

Experimentally $\vec{E}_{eff}$ is detected, not $\vec{E}$, so $\vec{E}_{eff}$ is the electric field used in Equation (2.1) and will be denoted from now on as $\vec{E}$. (See Ziman[7] p. 383 for more elucidation). Equation (2.27) is known as the linearized Boltzmann equation where only leading order terms have been kept, terms of second order such as ∇g have been dropped.

An arbitrary solution to Equation (2.27) can be written as

$$g(\vec{k},\vec{r}) = \frac{\partial f^0}{\partial \varepsilon}\left(e\vec{E}\cdot\vec{\psi} + (\varepsilon-\mu)\nabla T\cdot\vec{\phi}/T\right) \tag{2.29}$$

in terms of two unknown functions $\vec{\psi}$ and $\vec{\phi}$. Using Equation (2.29) with the collision term expressed as a linear operator $\partial f/\partial t)_c = \hat{w}(f)$, it can

be shown that the equations which the components of $\vec{\psi}$ and $\vec{\phi}$ must satisfy are

$$e/\hbar \left(\frac{\vec{v}}{c}\times\vec{B}\right)\cdot\nabla_k\psi_i + \hat{w}\left(\frac{\partial f^o}{\partial\varepsilon}\,\psi_i\right)\Big/\partial f^o/\partial\varepsilon = -v_i \qquad (2.30a)$$

and

$$e/\hbar \left(\frac{\vec{v}}{c}\times\vec{B}\right)\cdot\vec{v}_k\phi_i + \hat{w}\left((\varepsilon-\mu)\,\frac{\partial f^o}{\partial\varepsilon}\,\phi_i\right)\Big/(\varepsilon-\mu)\,\frac{\partial f^o}{\partial\varepsilon} = -v_i \qquad (2.30b)$$

Once Equation (2.30) is solved for ψ_i and ϕ_i subject to the appropriate boundary conditions the electrical and heat currents are calculable using

$$\vec{J}(\vec{r}) = -\frac{e}{4\pi^3}\int d\vec{k}\;\vec{v}\;g$$

$$= -\frac{e}{4\pi^3}\int d\vec{k}\;\vec{v}\;\left(\frac{\partial f^o}{\partial\varepsilon}\right)(e\vec{E}\cdot\vec{\psi} + (\varepsilon-\mu)\nabla T\cdot\vec{\phi}/T) \qquad (2.31a)$$

and

$$\vec{U}(\vec{r}) = \frac{1}{4\pi^3}\int d\vec{k}\;\vec{v}(\varepsilon-\mu)g$$

$$= \frac{1}{4\pi^3}\int d\vec{k}\;\vec{v}(\varepsilon-\mu)\left(\frac{\partial f^o}{\partial\varepsilon}\right)(e\vec{E}\cdot\vec{\psi} + (\varepsilon-\mu)\nabla T\cdot\vec{\phi}/T) \qquad (2.31b)$$

Comparing Equation (2.31) with Equation (2.1) and using the fact that $\int d\vec{k} = \int d\varepsilon ds/\hbar|\vec{v}|$ where ds is an element of a constant energy surface, one can show that

$$\sigma_{ij} = e^2\,A_{ij}\Big|_{\varepsilon=\mu} \qquad (2.32a)$$

and

$$\lambda_{ij} = L_o\,T\,e^2\,B_{ij}\Big|_{\varepsilon=\mu} \qquad (2.32b)$$

where the Lorenz number L_o is given by $\frac{1}{3}\pi^2\,k_B^2/e^2$ and

wher

and

Expl
ture
obta

hence

and

along

a form

where

$$A_{ij}(\varepsilon) = \frac{1}{4\pi^3} \int_{\varepsilon} \frac{ds}{h} \frac{v_i}{|\vec{v}|} \psi_j \tag{2.33a}$$

and

$$B_{ij}(\varepsilon) = \frac{1}{4\pi^3} \int_{\varepsilon} \frac{ds}{h} \frac{v_i}{|\vec{v}|} \phi_j \tag{2.33b}$$

Exploiting the delta function like properties of $\partial f^o/\partial\varepsilon$ at low temperatures in evaluating integrals over energy using an expansion in $k_B T$ one obtains

$$-\int_0^\infty F(\varepsilon)\, \partial f^o/\partial\varepsilon \, d\varepsilon \approx$$

$$F(\mu) + \frac{\pi^2}{6} (k_B T)^2 \left.\frac{\partial^2 F}{\partial \varepsilon^2}\right|_{\varepsilon=\mu} + O(k_B T)^4$$

hence one can show that

$$\pi_{ij} = L_o e^3 T^2 \left.\frac{\partial}{\partial\varepsilon} A_{ij}(\varepsilon)\right|_{\varepsilon=\mu} \tag{2.34a}$$

and

$$\varepsilon_{ij} = -L_o e^3 T \left.\frac{\partial}{\partial\varepsilon} B_{ij}(\varepsilon)\right|_{\varepsilon=\mu} \tag{2.34b}$$

The general Onsager relation

$$\varepsilon_{ij}(-\vec{B}) = \pi_{ji}(\vec{B})/T \tag{2.34c}$$

along with Equations (2.32a) and (2.34a) imply that

$$\varepsilon_{ij}(-\vec{B}) = L_o e T \left.\frac{\partial \sigma_{ji}(\varepsilon,\vec{B})}{\partial\varepsilon}\right|_{\varepsilon=\mu} \tag{2.35}$$

a form obtained by Averback and Wagner.[9]

In general, the Boltzmann equation can not be solved in closed form; normally its solution is found using numerical methods. However general results for the magnetic field dependence of the transport tensors can be deduced using the theory of Lifshitz, Azbel, and Kaganov[2,3]--the LAK theory.

3. HIGH MAGNETIC FIELD THEORY

The LAK theory searches for a solution to the Boltzmann equation in the high magnetic field limit using an expansion in the inverse of the field 1/B. With the z axis chosen to lie along the field direction and the field oriented such that all electron orbits are closed, the theory predicts, to leading order, that

$$\sigma_{xx}(B) = \frac{A_{xx}^{(2)}}{B^2} + \frac{A_{xx}^{(3)}}{B^3} + \frac{A_{xx}^{(4)}}{B^4} + \ . \ . \ . \qquad (3.1a)$$

and

$$\sigma_{yx}(B) = \frac{A_{yx}^{(1)}}{B} + \frac{A_{yx}^{(2)}}{B^2} + \frac{A_{yx}^{(3)}}{B^3} + \ . \ . \ . \qquad (3.1b)$$

where the coefficients $A_{ij}^{(m)}$ for $m \geq 2$ depend upon the detailed shape of the Fermi surface and upon the detailed form of the scattering operator. On the other hand,

$$A_{yx}^{(1)} = ec(n_e - n_h) \qquad (3.2)$$

where n_e is the number of electrons and n_h is the number of holes. For a perfectly compensated metal $n_e = n_h$ so the leading term in the expansion for σ_{yx} becomes proportional to $1/B^2$.

In an experimental situation, with the magnetic field directed along a symmetry direction so that Equation (2.3) applies, the resistivity tensor derived from inverting the conductivity tensor is

$$\rho_{xx} = \frac{\sigma_{xx}}{(\sigma_{xx}^2 + \sigma_{yx}^2)} \tag{3.3a}$$

and

$$\rho_{yx} = \frac{\sigma_{yx}}{(\sigma_{xx}^2 + \sigma_{yx}^2)} \tag{3.3b}$$

Because $\rho_{yx}/\rho_{xx} << 1$ for compensated metals

$$\rho_{xx} \simeq 1/\sigma_{xx}$$

$$\simeq \frac{B^2}{A_{xx}^{(2)}} \left(1 - \frac{A_{xx}^{(3)}}{A_{xx}^{(2)}B} + \ . \ . \ .\right) \tag{3.4a}$$

and

$$\rho_{yx} \simeq \sigma_{yx}/\sigma_{xx}^2$$

$$\simeq \left(\frac{B^2}{A_{xx}^{(2)}}\right)^2 \left\{\left(A_{yx}^{(2)} - \frac{2A_{xx}^{(3)}A_{yx}^{(1)}}{A_{xx}^{(2)}}\right)\frac{1}{B^2} + \frac{A_{yx}^{(1)}}{B}\right.$$

$$\left. + \left(A_{yx}^{(3)} - 2\,\frac{A_{xx}^{(3)}A_{yx}^{(2)}}{A_{xx}^{(2)}}\right)\frac{1}{B^3} + \ . \ . \ .\right\} \tag{3.4b}$$

The term $A_{yx}^{(1)}/B$ is included in Equation (3.4b) because in practice, perfect compensation is never achieved. However this term is expected to be small for very pure samples. So, in a shorthand notation, the expected resistivity for a compensated metal in the high field limit with

closed orbits is

$$\rho_{xx}(B) = B^2 + B + B^0 + \ . \ . \ . \qquad (3.5a)$$

and

$$\rho_{yx}(B) = (B^3)^{\cdot} + B^2 + B + B^0 + \ . \ . \ . \qquad (3.5b)$$

where the small, if noticeable B^3 term is the result of some slight non-compensation.

In an experimental determination of $\overleftrightarrow{\rho}$, the magnetic field is reversed to eliminate errors caused by measurement probe misalignment. In terms of these measured values ρ^m, the experimentally determined resistivity is given by

$$\rho_{xx}^{exp}(B) = \tfrac{1}{2}(\rho_{xx}^m(B) + \rho_{xx}^m(-B)) \qquad (3.6a)$$

and

$$\rho_{yx}^{exp}(B) = \tfrac{1}{2}(\rho_{yx}^m(B) - \rho_{yx}^m(-B)) \qquad (3.6b)$$

Using the results of Equation (3.5) in Equation (3.6) one might expect that

$$\rho_{xx}^{exp} = B^2 + B^0 + \ . \ . \ . \qquad (3.7a)$$

and

$$\rho_{yx}^{exp} = (B^3) + B + \ . \ . \ . \qquad (3.7b)$$

But this odd power expansion represented by Equation (3.7b) is a poor fit of R. Fletcher's[4,5] data for these W and Cd crystals. He found that much better fits of his ρ_{yx} data were obtained using $\rho_{yx}^{exp}(B) = aB^{1.9}$ for Cd below 3 K, and $\rho_{yx}^{exp}(B) = bB^2 + cB$ for W. This discrepancy between experiment and theory is not due to a fundamental flaw in the basic LAK

theory, but is the result of using an invalid deductive step in applying the theory under field reversal.

It is our contention that the relationships in Equation (3.1) contain no field direction information in the quantity "B". "B" represents only the magnitude of the magnetic field--the field direction information is buried in the calculations determining the coefficients $A_{ij}^{(m)}$.

Conducting two thought experiments will show that simply replacing B by -B in Equation (3.5) to represent a field reversal is not correct. First consider reversing the magnetic field in a continuous manner by reducing the magnetic field strength from an initial value of B_i to zero, reversing the current leads to the magnet, and then increasing the field strength to a magnitude of B_i. Although the field has been reversed in a continuous and certainly valid manner, the representation for σ expressed by Equation (3.1) has not been as fortunate. In fact, the LAK theory breaks down in this field reversal experiment because the theory is only valid at high field strengths as is evident from Equation (3.1) where more and more terms in the expansion series become important as the field strength is reduced until Equation (3.1) loses all meaning at the point B = 0.

One can easily get around this problem of violating the high field condition by performing an alternate thought experiment where the reversal is achieved by rotating the field direction in a continuous manner about an axis perpendicular to the original field direction while maintaining the field strength at a constant high field value B_i. The field has been reversed when this angle of rotation θ has reached 180°. Over the course of this experiment the conditions for the validity of Equation (3.1) have been met, however, the point θ = 180° is rather

unique. At any other value ($0 < \theta < 180$) no one would attempt to insert this directional dependence in the "B"'s of Equation (3.1), but they would correctly try to evaluate new coefficients. Since this direction information is buried in the A_{ij}'s for $0 < \theta < 180$ it is unreasonable to expect the "B"'s to suddenly contain field direction information for the particular value of $\theta = 180°$.

Before examining the LAK theory in more detail to discover how the "B"'s in Equation (3.1) lost their field direction information and where this information now resides, some deceptively simple properties of $\overleftrightarrow{\rho}$ under field reversal will be explored.

First consider the relationship between $\rho_{xx}(B)$ and $\rho_{xx}(-B)$. Figure 3.1a shows an experimental arrangement to determine $\rho_{xx}(B)$ where the crystalline sample, represented by the rectangle, has a crystalline coordinate system $\{x',y',z'\}$ permanently associated with it. (That is, the position of the atoms are given by $\vec{R} = a\hat{x}' + b\hat{y}' + c\hat{z}'$.) A laboratory coordinate system is chosen so that the z axis lies along the magnetic field direction and the x axis lies along the electrical current direction. As a result of this current, a component E of the electric field along the x direction is generated, whose magnitude is related to the current density of J by the resistivity tensor element $\rho_{xx}(B)$. That is

$$\rho_{xx}(B) = E\Big|_{3.1a}\Big/J$$

If the crystal has two-fold symmetry about $\vec{x}'$, rotating the crystal by 180° about $\vec{x}'$ as shown in Figure 3.1b can not change the magnitude nor the direction of this electric field component along $\vec{x}$. That is, the observable parameters can not know that a rotation has been

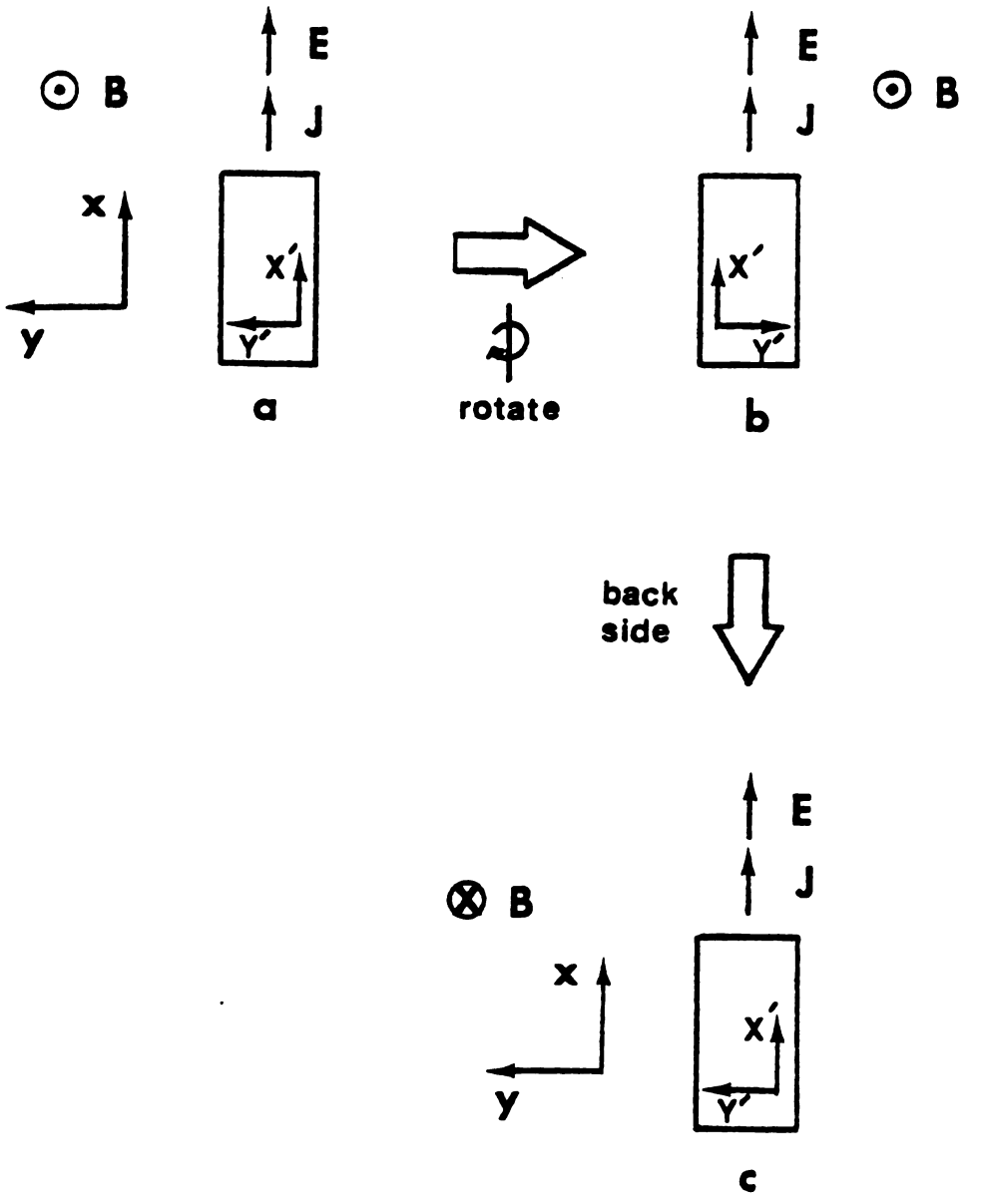

Figure 3.1 Experimental situation for ρ_{xx} measurement.

performed--they can not "see" the artificial labeling axes {x',y',z'}. Thus $E\Big|_{3.1b} = E\Big|_{3.1a}$.

Examining the experimental situation in Figure 3.1b from behind the sample yields the situation shown in Figure 3.1c. Since nothing has changed about the physical system $E\Big|_{3.1c} = E\Big|_{3.1b}$. If we ignore all external references of the laboratory, Figures 3.1a and 3.1c are physically identical except that the magnetic field has been reversed. The ratio between the component of the electric field along $\vec{x}$ in Figure 3.1c to the current density is by definition $\rho_{xx}(-B)$. So $\rho_{xx}(-B) = E\Big|_{3.1c} \Big/ J$ which means that

$$\rho_{xx}(-B) = \rho_{xx}(B) \tag{3.8a}$$

Similar arguments show that

$$\rho_{yx}(-B) = -\rho_{yx}(B) \tag{3.8b}$$

The experimental situation to determine $\rho_{yx}(B)$ is shown in Figure 3.2a where in terms of the component of the electric field along the y axis, $\rho_{yx}(B) = E\Big|_{3.2a} \Big/ J$. Operating on the crystal with the rotation operator produces Figure 3.2b which implies that $E\Big|_{3.2b} = E\Big|_{3.2a}$. The back side view of this situation is shown in Figure 3.2c, which is the experimental situation for determining $\rho_{yx}(-B)$. Since the component of the electric field $E\Big|_{3.2c}$ is equal in magnitude but points in the opposite direction to $E\Big|_{3.2a}$ $\left(\text{i.e. } E\Big|_{3.2c} = -E\Big|_{3.2a}\right)$ then $\rho_{yx}(-B) = E\Big|_{3.2c} \Big/ J = -\rho_{yx}(B)$.

Fig

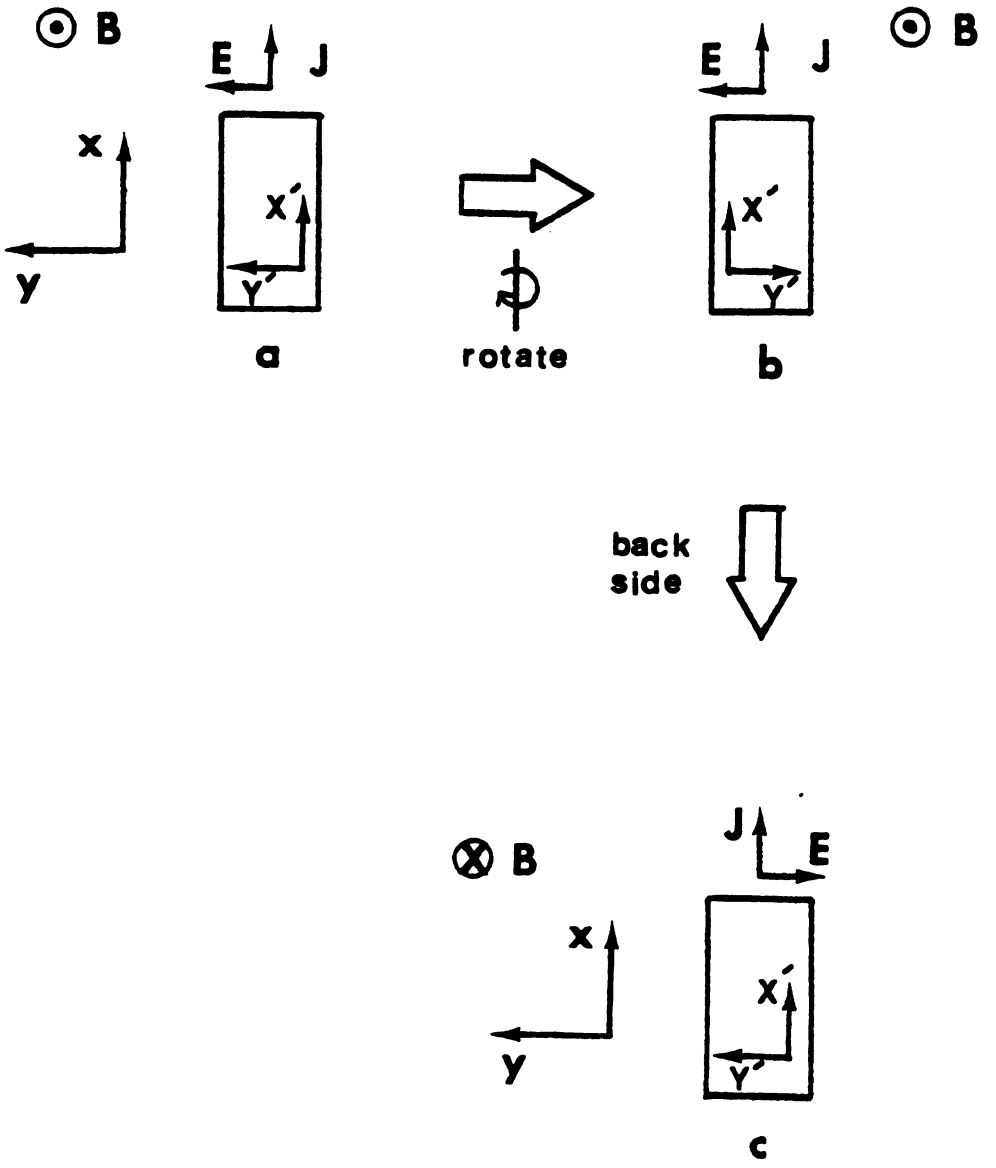

Figure 3.2 Experimental situation for ρ_{yx} measurement.

Equ

if the s

instead

ment use

simple s

has two-

symmetry

upon the

up and d

is certa

along a

Sim

and

as can

derivin

The

referred

while t

Equation

complete

with the

Equation (3.8) can also be shown to be true, in a similar manner, if the system has a two-fold rotational axis about the $\vec{y}'$ direction instead of the $\vec{x}'$ direction. Actually, the rotational symmetry requirement used in deriving Equation (3.8) is not a further restriction for simple systems (systems without a basis) because every Bravais lattice has two-fold rotational axes perpendicular to any three-fold or higher symmetry direction. Ultimately the validity of Equation (3.8) is based upon the fact that the crystal structure can not differentiate between up and down (i.e. between the $\vec{B}$ and $-\vec{B}$ directions). Thus Equation (3.8) is certainly true for all simple metal systems with the magnetic field along a symmetry direction.

Similar relations are true for the conductivity tensor

$$\sigma_{xx}(-B) = \sigma_{xx}(B) \tag{3.9a}$$

and

$$\sigma_{yx}(-B) = -\sigma_{yx}(B) \tag{3.9b}$$

as can be deduced either by using similar arguments to those used in deriving the ρ relations, or by using Equations (3.3) and (3.8).

The relations expressed by Equations (3.8) and (3.9) are commonly referred to as 'the diagonal components are even functions of the field while the off-diagonal components are odd'. It should be noted that Equation (3.9a) is not new, it is one of Onsager's relations and is completely general; Equation (3.9b) is new and should not be confused with the Onsager relation

$$\sigma_{xy}(\vec{B}) = \sigma_{yx}(-\vec{B}) \tag{2.4a}$$

The implications of these relations on the theoretical expressions for $\overleftrightarrow{\sigma}$ from the LAK theory can be very serious. If Equation (3.1) did contain field direction information in the "B"'s then Equation (3.9) demands that

$$A_{xx}^{(odd)} = 0 \tag{3.10a}$$

and

$$A_{yx}^{(even)} = 0 \tag{3.10b}$$

Our contention that the "B"'s contain no directional information implies that Equation (3.10) need not be true and that the field reversal information can be explicitly incorporated in Equation (3.1) as

$$\sigma_{xx}(\pm B) = A_{xx}^{(2)}/B^2 + A_{xx}^{(3)}/B^3 + \ . \ . \ . \tag{3.11a}$$

and

$$\sigma_{yx}(\pm B) = \pm(A_{yx}^{(1)}/B + A_{yx}^{(2)}/B^2 + \ . \ . \ . \ ) \tag{3.11b}$$

At this point it is important to clear up a misconception that appears in the literature concerning the "even" and "oddness" of $\overleftrightarrow{\sigma}$ expressed by Equation (3.9). Because σ_{xx}, for example, is an even function of the magnetic field, it is argued that its expansion must contain only even powers of B, however this is not true because this argument is implicitly assuming that the range of pertinent magnetic field strengths includes B = 0, thus requiring $\overleftrightarrow{\sigma}$ to be analytic and expandable in a Taylor series about B = 0. The expansions for $\overleftrightarrow{\sigma}$ resulting from the LAK theory are not analytic at B = 0, so certain powers of B are not necessarily prohibited.

The

field s

the rang

arises f

bounded

equation

proporti

applicab

an expan

because

for magn

effects

theory's

It

to see w

informat

LAK Theo

In

along ort

with plan

electron

point al

*Ignorin
analytic
because
to become
from pos-
reality.

The question that arises is why is $\overleftrightarrow{\sigma}$ nonanalytic in the magnetic field strength B? The answer is that the LAK theory is analytic over the range of its validity and that any apparent nonanalytic behavior arises for magnetic field strengths outside this range. This range is bounded from below because LAK used as a solution to the Boltzmann equation a series expansion in a small parameter ω_H, which is inversely proportional to the magnetic field strength. This restricts the theory's applicability to high fields in order to ensure the usefulness of such an expansion, as has been previously discussed. The upper bound arises because we are dealing with a semi-classical theory which is valid only for magnetic field strengths sufficiently small that field quantization effects are negligible. Therefore, the problems associated with the theory's nonanalyticity at B = 0 and at $\omega_H = 0^*$ (B = ∞) are not relevant.

It is now appropriate to examine the derivation of the LAK theory to see why the "B"'s in Equation (3.1) contain no field direction information.

LAK Theory

In the presence of a magnetic field, electrons travel in $\vec{k}$ space along orbits given by the intersections of surfaces of constant energy with planes perpendicular to the magnetic field. The position of an electron is describable by the time of rotation t from some arbitrary point along its orbit and by two constants of the motion, the electron's

---

*Ignoring the limitations imposed by quantization effects, the non-analyticity of the LAK theory at $\omega_H = 0$ has no physical significance because for ω_H to get smaller and smaller, to pass through zero, and to become negative means that the magnetic field would have to pass from positive infinity to negative infinity in a manner that escapes reality.

energy ε and the projection of its wave vector k_z along the magnetic field direction. The z axis has been chosen to lie along the magnetic field direction.

From the equations of motion

$$\hbar \frac{dk_x}{dt} = - \frac{e}{c} B V_y \tag{3.12a}$$

$$\hbar \frac{dk_y}{dt} = \frac{e}{c} B V_x \tag{3.12b}$$

$$\hbar \frac{dk_z}{dt} = 0 \tag{3.12c}$$

we obtain

$$(dk_\perp)^2 = (dk_x)^2 + (dk_y)^2$$

$$= \frac{e^2}{\hbar^2 c^2} B^2 V_\perp^2 dt^2$$

or

$$dk_\perp = \left| \frac{e}{\hbar c} B \right| V_\perp dt \tag{3.13}$$

where the symbol $\perp$ represents the magnitude of a vector perpendicular to the magnetic field direction. $dk_\perp$ is an element of length taken along the direction of the electron's trajectory. Integrating Equation (3.13) yields

$$t = \left| \frac{c\hbar}{eB} \right| \int_{k_{\perp o}}^{k_\perp} \frac{dk_\perp'}{V_\perp} \tag{3.14}$$

The period for one complete orbit defines a frequency ω_H as

$$\frac{2\pi}{\omega_H} = \left| \frac{c\hbar}{eB} \right| \oint \frac{dk_\perp'}{V_\perp} \tag{3.15}$$

It should be noted at this stage that ω_H (or "B") contains no field direction information (i.e. ω_H is strictly positive), all directional information was lost in deriving Equation (3.13) where the field strength came in as B^2. The field direction information resides in the choice of the coordinate system to be used in the integrals over $\vec{k}$ space, chosen such that as the electron travels along its orbit, time increases (see Equation (3.14)).

For electrons in the presence of electric and magnetic fields, it is convenient to describe the electronic states using the parameters ε, k_z and the dimensionless quantity

$$\phi = \omega_H \left|\frac{c\hbar}{eB}\right| \int_{k_{\perp o}}^{k_\perp} \frac{dk_\perp'}{V_\perp} \tag{3.16}$$

(As can be seen from Equation (3.15) ϕ varies from 0 to 2π.)

The Boltzmann equation, written in these variables, is

$$\frac{\partial f}{\partial \phi}\dot{\phi} + \frac{\partial f}{\partial k_z}\dot{k}_z + \frac{\partial f}{\partial \varepsilon}\dot{\varepsilon} + \frac{\partial f}{\partial t}\Big)_c = 0 \tag{3.17}$$

If $\vec{E}$ is perpendicular to $\vec{B}$ then the Lorentz force

$$\hbar\dot{\vec{k}} = -(e/c)[\vec{V}\times\vec{B}] - e\,\vec{E} \tag{3.18}$$

implies that

$$\dot{\varepsilon} = -e\,\vec{V}\cdot\vec{E} \tag{3.19a}$$

$$\dot{k}_z = 0 \tag{3.19b}$$

and

$$\dot{\phi} = \omega_H \left|\frac{c\hbar}{eB}\right| \frac{1}{V_\perp}\frac{dk_\perp}{dt} \tag{3.19c}$$

One can show that

$$\left(\frac{dk_\perp}{dt}\right)^2 \approx \frac{e^2B^2V_\perp^2}{c^2\hbar^2}\left[1 - 2\frac{c}{BV_\perp^2}(\vec{V}_\perp\times\vec{E})_z + O(E^2)\right]$$

which means

$$\dot{\phi} \approx \omega_H \qquad (3.19d)$$

where the term $\frac{c}{BV_\perp^2}(\vec{V}_\perp\times\vec{E})_z$ has been neglected. (For a typical metal in a field of 10 kG, this term is smaller than 10^{-7}). Using as the solution to the Boltzmann equation

$$f = f^0 + e\, t_0\, \psi_i\, E_i$$

where t_0 is some characteristic relaxation time (a constant), one finds, keeping only terms to leading order, that the deviations ψ_i from equilibrium must satisfy

$$\frac{\partial\psi_i}{\partial\phi} + \frac{1}{\omega_H t_0}\,\hat{w}(\psi_i) = \frac{V_i}{\omega_H t_0}\frac{\partial f^0}{\partial\varepsilon} \qquad (3.20)$$

where the collision term has been written in terms of some collision operator $\hat{w}(f)$ as

$$\left.\frac{\partial f}{\partial t}\right]_c = \frac{\hat{w}(f)}{t_0} \qquad (3.21)$$

Since LAK were interested in the high field limit, defined as $\omega_H t_0 >> 1$, where the electrons complete several orbits before being scattered, LAK looked for a solution to Equation (3.20) using a power series in $1/\omega_H t_0$:

$$\psi_i = \sum_{m=0}^{\infty} (\omega_H t_o)^{-m} \psi_i^{(m)} \tag{3.22}$$

Substituting Equation (3.22) into Equation (3.20) and equating equal powers of $\omega_H t_o$ one finds that the functions $\psi_i^{(m)}$ must satisfy

$$\frac{\partial \psi_i^{(0)}}{\partial \phi} = 0 \tag{3.23a}$$

$$\frac{\partial \psi_i^{(1)}}{\partial \phi} + \hat{w}(\psi_i^{(0)}) = V_i \frac{\partial f^o}{\partial \varepsilon} \tag{3.23b}$$

$$\frac{\partial \psi_i^{(m)}}{\partial \phi} + \hat{w}(\psi_i^{(m-1)}) = 0 \quad \text{for } m \geq 2 \tag{3.23c}$$

After solving Equation (3.23) for $\psi_i^{(m)}$ subject to the appropriate boundary conditions, the conductivity is given by

$$\sigma_{ij} = - \frac{e^2 t_o}{4\pi^3} \int V_i \, \psi_j \, d^3k \tag{3.24}$$

From Equations (3.15) and (3.22) it is clear that σ_{ij} has the form

$$\sigma_{ij} = \sum_{m=0}^{\infty} (|B|)^{-m} A_{ij}^{(m)} \tag{3.25}$$

where the $A_{ij}^{(m)}$ are dependent upon the specific form of the scattering operator $\hat{w}$ (see Equation (3.23)), upon the band structure (see Equation (3.24)) and upon the specific orientation of the magnetic field relative to the crystal structure (see Equation (3.24)). LAK proceed further and

show $A_{ij}^{(0)} = A_{xx}^{(1)} = 0$ and $A_{yx}^{(1)} = ec(n_e - n_h)$ for closed orbits and thus $\overleftrightarrow{\sigma}$ has the form expressed in Equation (3.1).

In summation, this re-examination of the LAK theory has revealed that the "B"'s in Equation (3.1) contain no field information and should more properly be written as $|B|$. For the field along a three-fold or higher symmetry axis, the requirement that σ_{xx} be an even function of the field while σ_{yx} be an odd function can be explicitly incorporated into the LAK expansion of $\overleftrightarrow{\sigma}$ as)

$$\sigma_{xx}(\pm B) = A_{xx}^{(2)}/B^2 + A_{xx}^{(3)}/B^3 + \ . \ . \ . \qquad (3.11a)$$

and

$$\sigma_{yx}(\pm B) = \pm(A_{yx}^{(1)}/B + A_{yx}^{(2)}/B^2 + \ . \ . \ .) \qquad (3.11b)$$

For compensated systems, these results manifest themselves in the resistivity tensor being of the form

$$\rho_{xx}(\pm B) = a_{xx}B^2 + b_{xx}B + c_{xx}B^0 + \ . \ . \ . \qquad (3.26a)$$

and

$$\rho_{yx}(\pm B) = \pm(a_{yx}B^2 + b_{yx}B + C_{yx}B^0 + \ . \ . \ .) \qquad (3.26b)$$

We have shown that the field reversal arguments supporting Equation (3.10) are invalid, thus all powers of B in Equations (3.11) and (3.26) should be present. In order for ρ_{xx} to contain only even powers of B and ρ_{yx} to contain only odd powers, one must now show that Equation (3.10) is true using some form of symmetry arguments in the derivation of the LAK theory--a result we can find no evidence for.

4. EXPERIMENTAL TECHNIQUE

4.1 Cd and W Samples

The two single crystals of Cd and W used in this study were obtained from R. Fletcher who had made several transport measurements on them[4,5,6]. The only change we made to the crystals was electroplating the ends of the W sample's arms with copper.* By doing this, all attachments to both samples could be made using low melting point solders (Rose's Alloy, Wood's Metal or Cerrolow).

Both crystals had been spark cut to a shape similar to that shown in Figure 4.1. The Cd crystal had a residual resistance ratio ($\rho_{293}/\rho_{4.2}$) of ~39,500. The [10$\bar{1}$0] direction was parallel to its length with ~5°, while the normal to its planar face was within ½° of the [0001] direction. The W crystal had a residual resistance ratio of ~29,000. The [100] direction was parallel to its length to ~1°, while the normal to its planar face was within 0.7° of the [001] direction.

4.2 Cryostat

The cryostat is basically a standard liquid ^{4}He cryostat, designed to operate in the temperature range of 1.5 to 100 K when immersed in liquid ^{4}He. In Figure 4.2 the main features of the cryostat below the liquid ^{4}He level are schematically shown along with the specific sample arrangement used in the thermopower studies.

The pumping line as well as the sides of the 1 K pot were made of stainless steel tubing to provide good thermal isolation from the 4.2 K

---

*A solution of copper sulfate ($CuSO_4 \cdot 5H_2O$ -- 200 g/ℓ) and sulfuric acid (H_2SO_4 -- 75 g/ℓ) was used.[10] The time needed to electroplate the W sample was ~5 minutes at a current of ~20 mA.

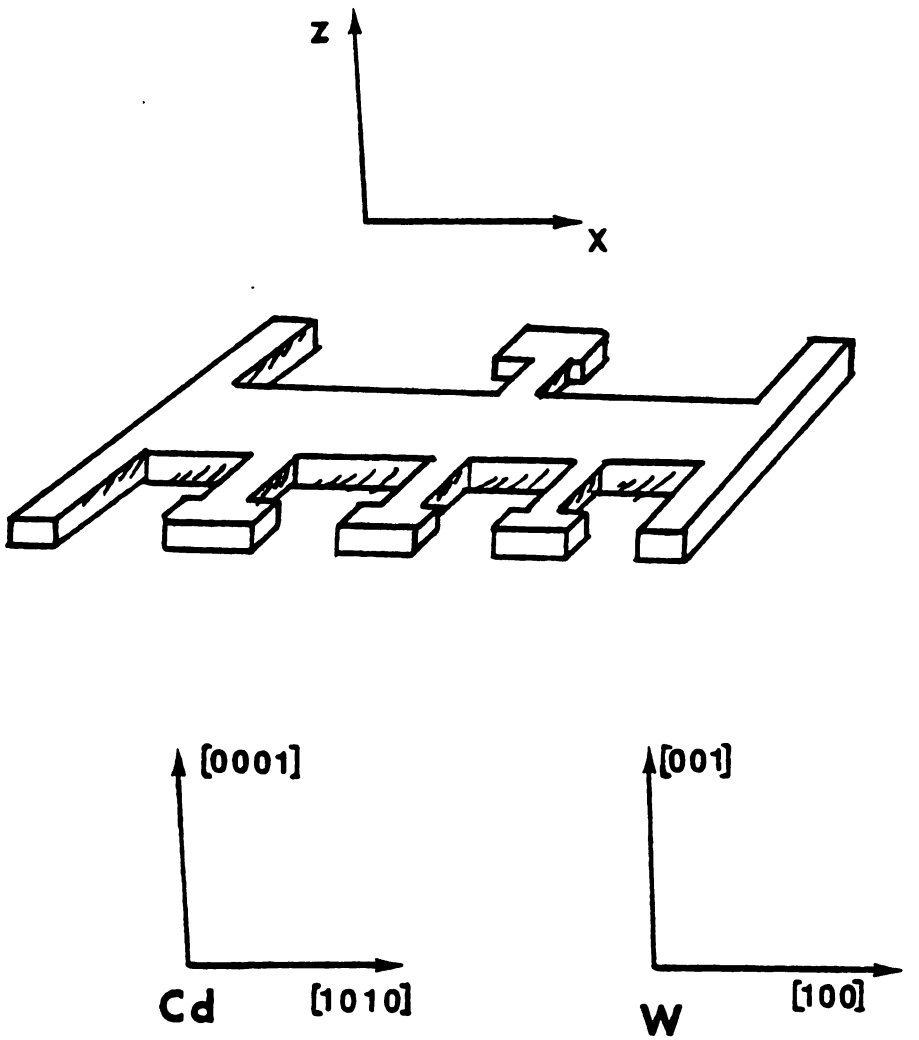

Figure 4.1 Shape of Cd and W crystals.

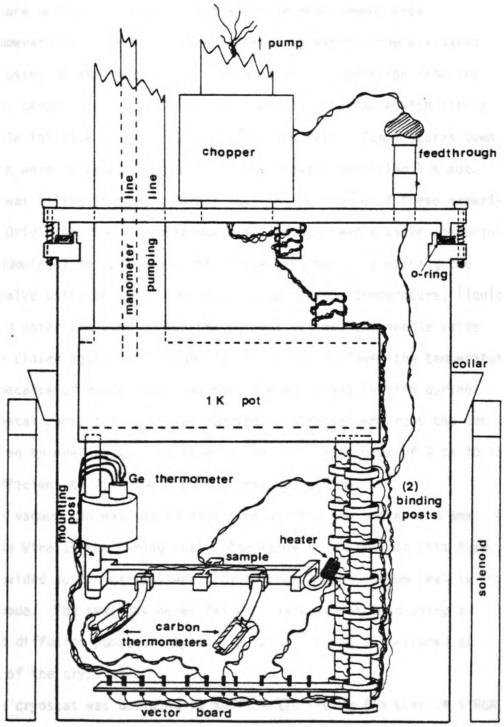

Figure 4.2 Cryostat schematic.

helium bath. The bottom of the pot, the two binding posts below the pot, and the sample mounting post were made of OFHC copper to insure temperature uniformity throughout the sample measurement area.

Temperatures above 4.2 K were achieved by warming the evacuated 1 K pot using an attached heater. Because of the isolation from the ^{4}He bath, temperatures up to 100 K were easily obtainable with little observable increase in the liquid ^{4}He boiling rate. Temperatures down to ~1.5 K were obtained by pumping on the liquid ^{4}He filled 1 K pot. The pot was filled in two different ways in the course of these experiments. Originally the cryostat was built with a needle valve connected to the pumping line just above the flange. By manually opening the needle valve using an extension reaching up to room temperature, liquid ^{4}He would enter the pot. After the pot was filled, the needle valve was then closed again before pumping on the pot to lower the temperature. Later, because of doubts about whether the valve was leaking during experimental runs, the valve was removed. In subsequent runs the pot was filled by over-pressuring it with ^{4}He gas. Pressures of 5 to 10 lbs. were sufficient to fill the pot in a reasonable time.

The vacuum can was sealed each time using a new piece of 3 amp Buss Fuse Wire as the O-ring seal. The large Pb content of this fuse wire provided sufficient malleability so that a good vacuum seal is easily made. The seal has never failed. Vacuums obtained using a standard diffusion pump were typically $<2\times10^{-6}$ mm Hg as measured at the top of the cryostat.

The cryostat was designed to be inserted inside the bore of a RCA superconducting solenoid. This magnet had a linearity of 1% up to its limiting field of 50 kG and had a field homogeneity over the sample

volume of 0.1%. Because of induced emfs associated with any movement of electrical wires with respect to a magnetic field, it is essential that vibrations be minimized. To accomplish this, a collar was attached to the outside of the vacuum can which presses against the top flange of the solenoid when the cryostat is inserted into the solenoid. By "jamming" the cryostat into the magnet in this way the motion of the cryostat with respect to the magnetic field is severely reduced.

The wires coming down from room temperature were first lagged to the ^{4}He bath temperature by wrapping them several times around a copper binding post attached to the top vacuum can flange. The wires were similarly lagged to the top of the 1 K pot before being individually wrapped to the binding posts attached to the bottom of the pot. Finally the wires were connected to pins in a piece of vector board. Connections to various thermometers, heaters, etc. were easily made by soldering to these pins. To minimize unwanted thermal links, most of the wires were manganin wire (~29 Ω/ft). A few wires were copper (~34 AWG) which were used in place of the manganin to avoid unwanted heating when larger currents were needed.

An electrical feedthrough was built on this cryostat to provide electrical connections between the sample area and the main liquid ^{4}He bath area where the chopper resides. This feedthrough was built following the design of A. C. Anderson.[11]

4.3 S^a of Cd and W: Measurements

The Cd and W crystals were transversely mounted relative to the magnetic field direction by soldering their ends into the mounting post with a low melting point solder (Cerrolow). The samples were optically

aligned so that their planar faces were perpendicular to the magnetic field direction to within ¼°. The alignment procedure is outlined in Appendix B.

The thermopower is experimentally measured by producing a temperature difference ΔT along the sample by heating one end of the sample using a heater. The thermopower is given by the resultant voltage difference ΔV between two points along the sample divided by the temperature difference between those two points. That is

$$S^a = \frac{E_x}{\partial T/\partial x}$$

$$\simeq \frac{E_x \Delta x}{\Delta T}$$

So
$$S^a \simeq - \frac{\Delta V}{\Delta T} \qquad (4.1)$$

The voltage measurements in this thermopower study were made using a Superconducting Chopper Amplifier (chopper) and the temperature measurements were made using carbon resistor thermometry. The heater was made by wrapping Evanohm wire around a bent piece of copper wire using cigarette paper as insulation. The resistance of this heater was ~4.9 kΩ. The electrical connections between the sample and the chopper were made with Cu-Ni clad NbTi wire. Because it is superconducting, no thermopower contributions of this wire are encountered.

4.3.1 Carbon Resistors

Temperatures in the large magnetic fields used in these thermopower studies of Cd and W were measured using carbon resistors. A pair of

matched 180 Ω, 1/8 Watt Allen-Bradley carbon resistors were used. This pair was chosen from several resistors each with one side sanded down to the bare carbon to insure good thermal contact to the sample. Because the largest change in resistance of carbon resistors occurs after the first cycling between 4 K and room temperature,[12,13] the resistors were immersed in liquid ^{4}He a few times before the two resistors with the closest resistance values were chosen. These resistors had a resistance of 2.97 kΩ and had a resistance difference of 0.007% at the nominal 4.2 K temperature of liquid He^4.

These sanded resistors were then varnished to copper strips using GE #7031 varnish with a layer of cigarette paper between the copper strip and the sanded face of the carbon resistor. The copper strips were then soldered to the potential arms of the sample. This assembled package provides good thermal contact between the sample and the carbon resistor as well as providing electrical isolation. The electrical leads connecting the resistors to the vector board consisted of ~5 inches of manganin wire whose poor thermal conductivity reduces the heat flow from the sample to the vector board. With no heat flow down these wires, a carbon resistor would be at the same temperature as its sample contact point. For later runs, the thermometer end of this assembly was covered with epoxy cement (Stycast 1266) to insure that the resistor was permanently bonded to the copper strip. No differences were observable in the measurements taken before and after the epoxy treatment.

Temperature Measurement

Because of cycling effects, the carbon resistors were calibrated against a germanium resistance thermometer in zero magnetic field during

each run. The carbons' resistances were measured using an A.C. bridge technique, illustrated in Figure 4.3. Basically a phase sensitive detector (PSD) was used to sense the voltage difference between two arms of a Wheatstone bridge. The oscillator output of the PSD was used as the power source for the bridge. In practice, the variable resistors (decade boxes) were adjusted until a null condition was reached implying that the resistances in the bridge arms were equal. With the selector switch in the "R_C" position, the resistance of the cold carbon resistor R_C was determined taking all lead resistances into account. (The cold carbon is the resistor nearest the mounting post.) In the "ΔR" position, the difference in resistance ΔR between the hot carbon R_H and the cold carbon R_C was determined. The fixed resistor R_A (~1.3 kΩ) was added to insure that this difference between the matched resistors remained a positive quantity. Because of the switch and independent variable resistors, R_C and ΔR could be quickly determined for each data point and the result "stored" on the decade box dials until other measurements had been completed.

The temperatures for these calibrations were determined using a Cryo-Cal germanium resistor which was factory calibrated between 1.5 and 100 K. Below 2 K, the accuracy of the calibration was reported to be 3 mK, increasing to 5 mK below 5 K. The resistance of the germanium resistor in these measurements was determined using a standard four-probe D.C. technique. The voltage generated across this resistor due to a constant D.C. current flowing through it was measured using a digital voltmeter.

For the measurements below ~2 K, the temperature was independently measured by monitoring the vapor pressure of the liquid ^{4}He in the 1 K

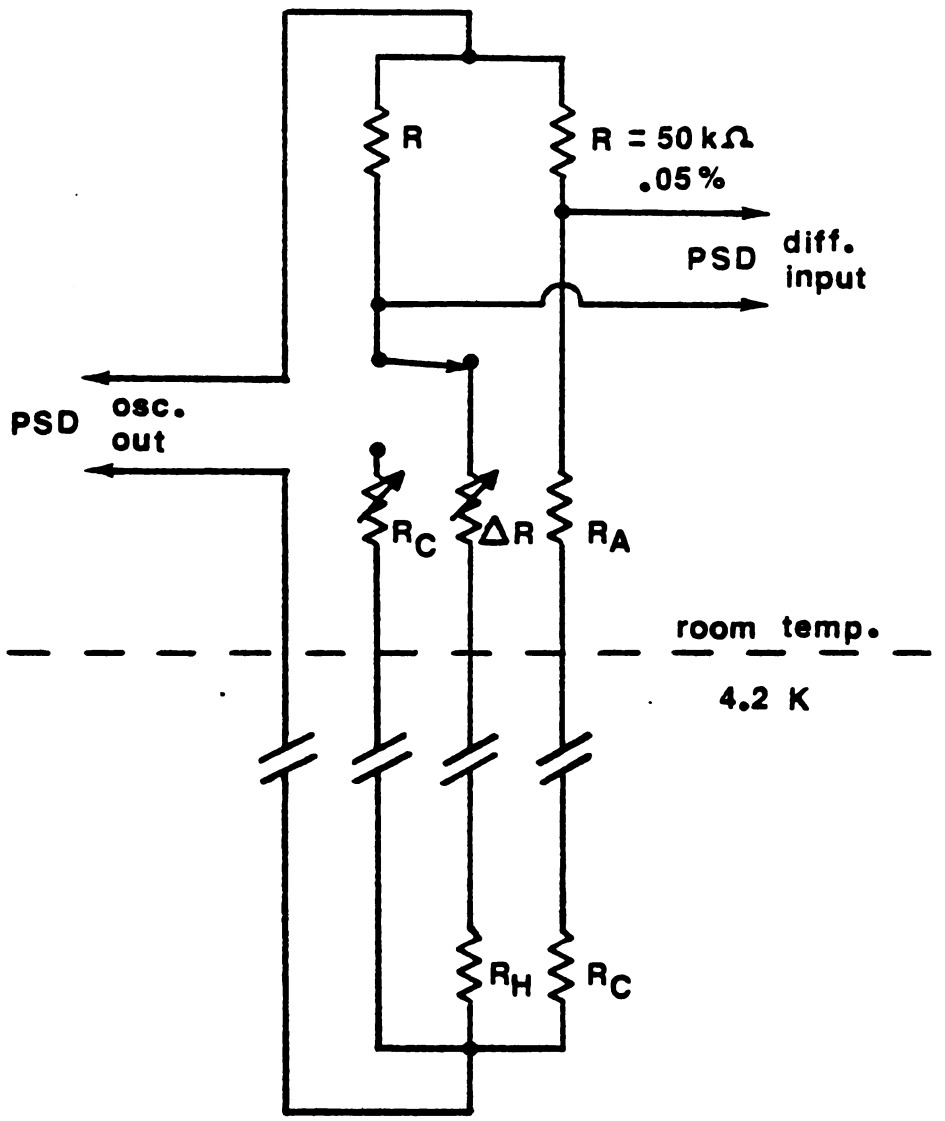

Figure 4.3 Circuit for carbon thermometry.

pot via the manometer line using a MKS Baratron Pressure Meter. The temperature was then determined from the National Bureau of Standards 1958 tables. The differences between the temperatures determined using the vapor pressure technique and using the germanium resistor technique had negligible impact on the experimental results.

The zero field calibration data were taken by controlling the temperature of the 1 K pot using a pressure regulator to adjust the helium pumping rate while the resistance of each carbon resistor was being measured. The data for each resistor were fitted to a modified Clement-Quinnell[14] formula

$$\ell nR = m\left(\frac{\ell nR}{T}\right)^{\frac{1}{2}} + b \qquad (4.2)$$

where m and b are adjustable parameters. The fits were made over three, roughly one degree intervals: 1.5-2.2 K, 2.2-3.2 K, 3.2-4.2 K; with five to ten data points in each interval. At the higher temperatures the errors in the fits were typically less than 0.002 K while below the λ point of He^4, the fits were better than 0.001 K. Because of the magnetoresistance of carbon resistors, temperatures derived using these zero field calibration fits in non-zero magnetic field situations must be corrected.

The temperature correction for the hot resistor is plotted in Figure 4.4 as a function of temperature at various magnetic field strengths. The ordinate is the erroneous temperature, derived from the carbon's resistance in a magnetic field using the zero field calibration fit, minus the actual temperature. This difference is negative because the resistance of carbon resistors increases both as the temperature

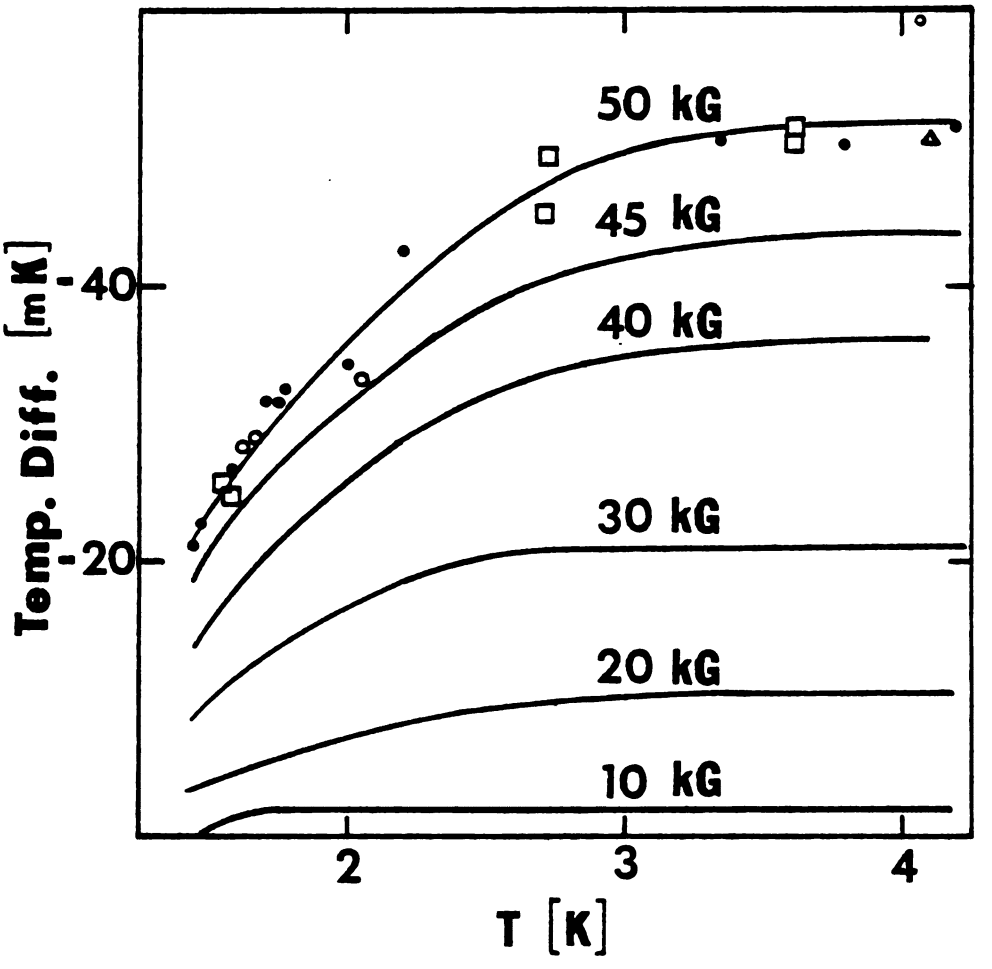

Figure 4.4 Field dependence correction for R_H.

decreases and as the magnetic field increases. Fortunately, unlike their temperature dependence, the magnetoresistance of carbon resistors is recyclable[12,13] as can be seen from the representative 50 kG data which was taken during six separate experimental runs. Data were taken at the different field strengths by maintaining a constant temperature using the pressure regulator. The temperature and field dependence of this temperature correction is consistent with the more extensive magnetoresistance studies of J. R. Pernicone.[12]

From this graph and a similar one for the cold carbon, corrections to the thermopower data were made. Because the temperature differences used in this study were ≤0.100 K at the lower temperatures, corrections to the measured temperature differences were ≤0.003 K, which resulted in corrections to the S^a data of ≤3%. Corrections to the temperature of each data point (taken as the average temperature of the two carbons) could amount up to 0.052 K at the largest field strength.

4.3.2 Superconducting Chopper Amplifier

The voltage measurements in the thermopower studies were made using a Superconducting Chopper Amplifier (chopper). A schematic of the chopper with its supporting electronics is shown in Figure 4.5. This chopper was built following the design of G. J. Edwards.[15] A negative feedback loop was added to the basic system using the ideas of R. Fletcher and M. R. Stinson.[16] Details about the specific components used are listed in Appendix C.

The basic operation of the chopper is the conversion of a D.C. signal to A.C. This conversion is made by the Modulator. The Modulator consists of a piece of NbTi wire which can be heated above its

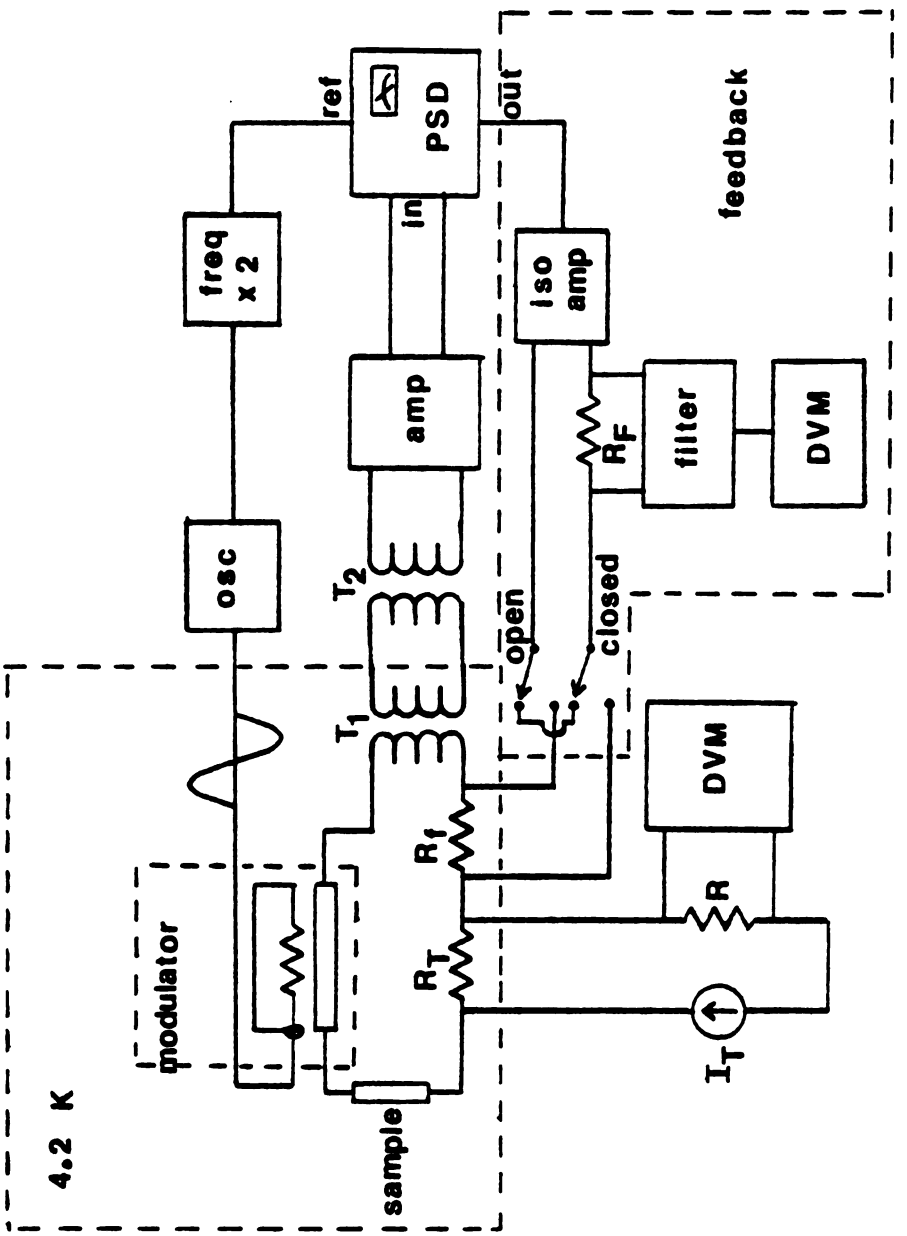

Figure 4.5 Schematic of chopper circuit

superconducting critical temperature using an attached heater. Because of the relatively high resistance of this wire in its normal state, the current flowing around the chopper circuit as the result of a thermal voltage in the sample, is significantly reduced when the NbTi wire is heated. By repeatedly warming and cooling the NbTi wire using an audio oscillator to drive the heater, an A.C. current is produced. This A. C. signal is then amplified using two transformers and an amplifier; and is then detected using a phase sensitive detector (PSD). This chopper system can be operated in any of three modes: Nulling, Amplifying, and Feedback.

Nulling Mode

Operating the chopper system in the nulling mode consists of canceling out the sample voltage V_S with a known voltage generated by passing a current I_T through the standard resistor R_T. Operationally the current I_T is adjusted until the signal detected on the PSD generated by the sample voltage is canceled by the voltage across R_T. When this condition is achieved $V_S = I_T R_T$.

Amplifying Mode

In the amplifying mode, the sample voltage is "read" directly on the PSD knowing the overall amplification of the system. Operationally this is done in two steps. First, the amplification A of the system is measured in terms of the signal level on the PSD generated by a known voltage across R_T. That is A = (signal level)/$I_T R_T$. Then second, the

voltage across the sample is measured by noting the signal level on the PSD with $V_T = 0$. The unknown sample voltage is then given by V_S = (signal level)/A.

Feedback Mode

With the addition of the feedback circuitry to the basic chopper system, the chopper can be operated in the feedback mode. The negative feedback, provided by the feedback current I_F through the liquid ^4He feedback resistor R_f, is generated by the output of the PSD. The purpose of the isolation amplifier is to break the ground loop between a grounded sample and the ground of the PSD. An analysis of the circuit reveals that the voltage V_{R_F} generated across the room temperature feedback resistor R_F is proportional to the voltage across the sample by an effective feedback amplification A_F. That is $V_{R_F} = A_F V_S$. To an excellent approximation

$$A_F \simeq A/(1 + \frac{R_f}{R_F} A) \tag{4.3}$$

where A is the open loop gain of the system. (See Appendix C for more details.) In this study $A\, R_f/R_F \simeq 83$, so $A_F \simeq R_F/R_f$. Because the amplification of the system depends only upon R_F and R_f and is independent of other components, it is very stable. In practice A_F is experimentally measured by using a known voltage across R_T. That is $A_F = V_{R_F}/V_T$. Subsequently any sample voltage is given by $V_S = V_{R_F}/A_F$.

All three modes of operation were used during this thermopower study. Depending upon the specific experimental situation, the advantages and disadvantages of each technique can be evaluated to determine the most advantageous mode.

The main disadvantage (a very severe one) of the amplifying mode is that the amplification of the system must be measured repeatedly because it changes with time and magnetic field.* It is a useful technique however if the sample voltage is changing rapidly with respect to an external parameter. For example, in this study W was found to have magnetothermopower oscillations at low temperatures. Data was taken in the amplifier mode with the magnetic field slowly sweeping to reduce the scatter in the data taken using the nulling technique.

On the other hand, gain instability causes no problems in the nulling mode because the gain must remain constant only over the relatively short time needed to make a measurement. (The field is already constant). However the technique does involve operator participation in adjusting the nulling current. This not only increases the time needed to make a measurement but also contributes to operator fatigue.

The feedback mode has the advantage that it requires no operator involvement--the result is simply read out as a voltage on a digital voltmeter. Also, because the amplification is quite stable, it need only be measured infrequently. An added benefit of using feedback is that the input impedance of the system is increased. A drawback of this method is the possibility of having some positive feedback present--which occurred in this particular system. Because of the particular

*The changes over time are generally believed to be the result of the rather critical dependence of the gain on the Modulator heater power adjustment. The dependence on magnetic field is not well understood.

components and their configuration, oscillations were present in V_{R_F} under steady state conditions--presumably the result of positive feedback. Attempts made to reduce these oscillations by introducing various capacitors along the feedback loop found little success. Because most of the magnetothermopower studies had been completed before the feedback work of Fletcher and Stinson was known, more time spent eliminating these oscillations was not justified. Simply passing the signal through a filter to minimize these oscillations was found to be adequate to complete the magnetothermopower studies. The long time constants needed were a hindrance; therefore, it is recommended that a more satisfactory solution to this problem of positive feedback be found if this system is to be used again.

In operation, the noise level for this chopper system (in any mode) was typically $\sim 2 \times 10^{-11}$ volts for sample resistances of ~5 mΩ which degrades to $\sim 2 \times 10^{-10}$ volts at the highest magnetic field used (50 kG).

An extrapolation of the field profiles of the magnet[17] suggested that the fringing field in the vicinity of the chopper was 600 Gauss for a central field of 50 kG. This would correspond to a change of ≤0.1% in the resistance of the standard resistors used in the chopper.

5. S^a OF Cd AND W: RESULTS AND DISCUSSION

The measurements of S^a for our Cd crystal were made during the course of nine experimental runs for which the crystal was inserted in the cryostat and realigned with respect to the magnetic field direction three separate times. In the first five runs, voltage measurements were made using the chopper in the nulling mode while in the latter four runs, the chopper was used in the feedback mode. Differences between data taken during various runs were not discernable.

As a further check of our measurement systems, we also made measurements of the electrical resistivity ρ_{xx} and the Nernst-Ettinghausen coefficient Q^a of this Cd crystal. In absolute numbers, our results were within 5% of those obtained by R. Fletcher at all temperatures and magnetic fields, which not only confirmed the validity of our measurement techniques but also indicated that the Cd crystal was relatively unchanged since Fletcher's studies.

The measurements of S^a for our W crystal were made during the course of four separate experimental runs. Voltage measurements were generally made using the chopper in the nulling mode, however, because we observed magnetothermopower oscillations, some data points, particularly at low temperatures and high magnetic fields, were taken using the chopper in the amplifier mode.

These magnetothermopower oscillations were significantly larger than the precision of our nulling mode measurements as shown in Figure 5.1 where some S^a data taken near 4.36 K and 50 kG is plotted against the field strength. At lower temperatures, the magnitude of these oscillations become quite comparable to the non-oscillitory component that we were interested in. To reduce the effects of these oscillations, the chopper was operated in the amplifying mode and the output of the PSD recorded on an x-y recorder. An example of the recorded output using this method is shown in Figure 5.2 for T near 1.7 K and for magnetic fields between 35 kG and 40 kG. Data such as this was generated and analyzed in several steps:

1. First, the ΔT heater was turned on to establish a temperature gradient along the sample and then the field was increased at a uniform rate to generate the "S^m" curve.

2. The field was then reduced to its initial value, and with the ΔT heater turned off, the field was swept again to generate the

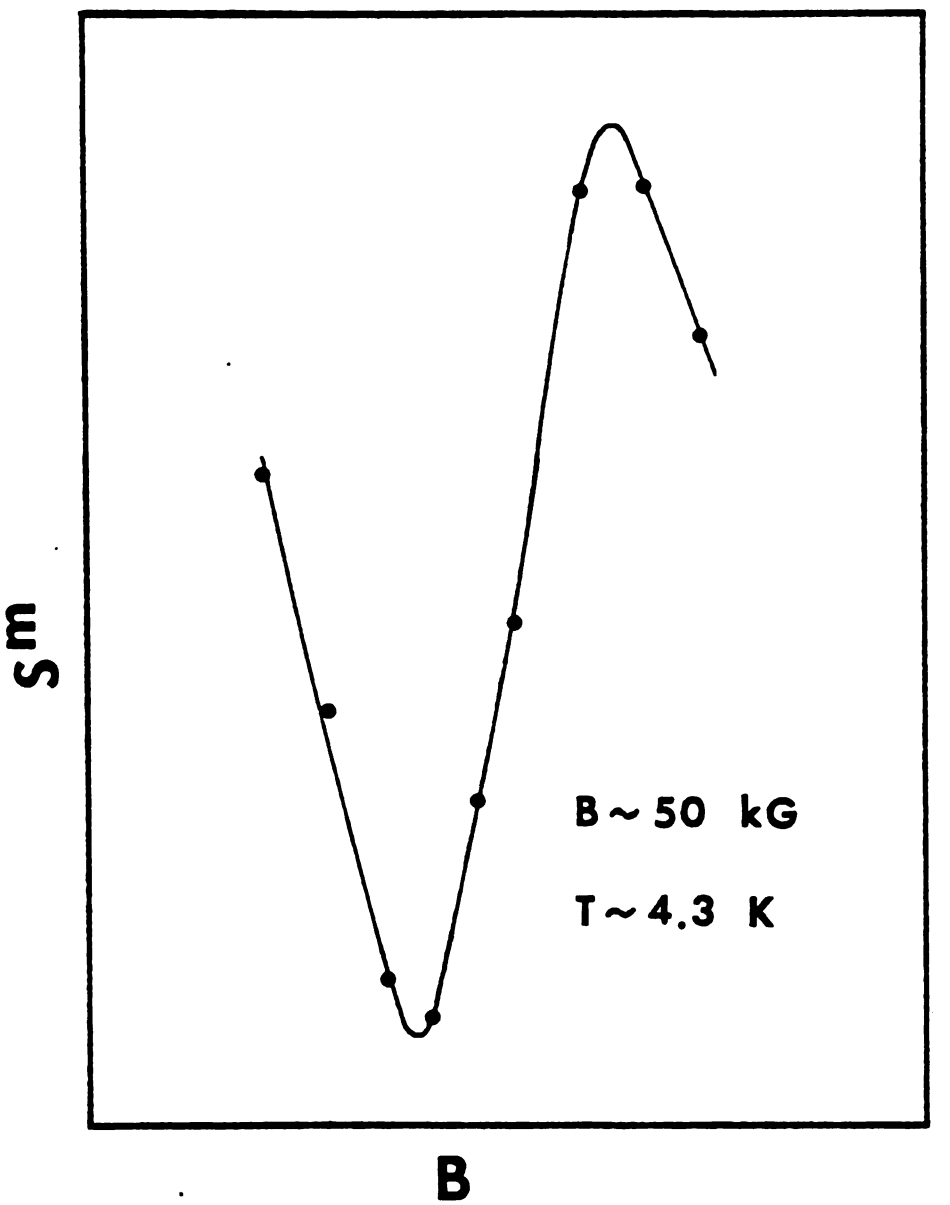

Figure 5.1 S^a oscillations of W--nulling mode

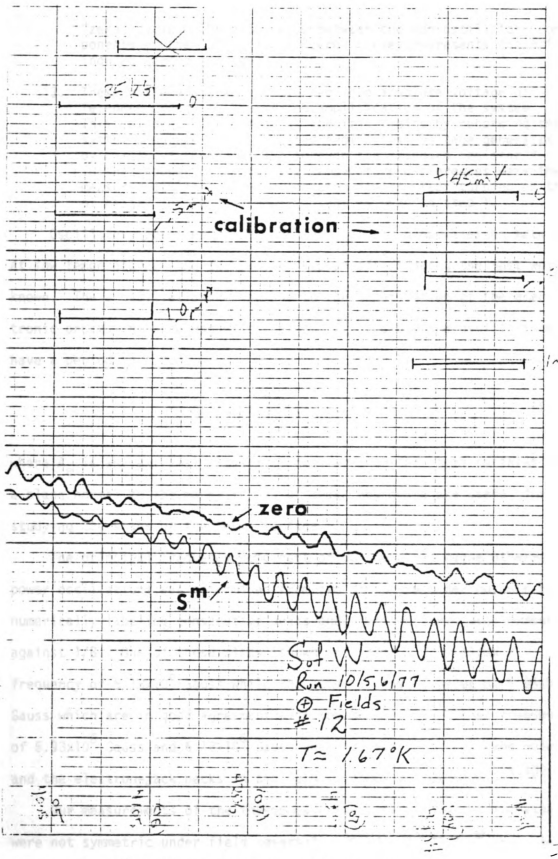

Figure 5.2 S^a oscillations of W--amplifying mode

"zero" curve. The difference between the non-oscillitory components of the "S^m" and the "zero" curves represents the emf induced across the sample.

3. These differences were converted into absolute voltage differences using the calibrated amplification of the system. This calibration was made at specific fields by recording the system's output which resulted from a test voltage generated by passing a known current through the standard resistor R_T in the chopper circuit. The temperature differences were then measured at these same calibration fields after turning on the ΔT heater to the same power output as used in step 1.

Oscillatory phenomena have been seen in many properties of metals at low temperatures--the de Haas-van Alphen effect being the most well known. These oscillations arise due to the quantization of the electronic orbits in large magnetic fields.[18] Because the oscillations have a period in 1/B of

$$\Delta(1/B) = \frac{2\pi e}{\hbar c} \frac{1}{A_e(\varepsilon_f)} \tag{5.1}$$

where A_e is any extremal cross-sectional area of the Fermi surfaces in a plane normal to the magnetic field, these phenomena are useful for studying the shape of the Fermi surface.

The principal frequency component of our observed magnetothermopower oscillations was determined from two of our recorder outputs by numerically labeling consecutive peaks and plotting these peak numbers against 1/B. One of these plots (shown in Figure 5.3) yielded a frequency of 6.18×10^6 Gauss while the other yielded a value of 5.96×10^6 Gauss which are in good agreement with the de Haas-van Alphen frequencies of 5.93×10^6 Gauss and 6.12×10^6 Gauss observed for the third band holes and the electron-jack necks in the Fermi surface of tungsten.[19,20]

Our measurements of the thermopower for both the Cd and W crystals were not symmetric under field reversal, that is, $S^m(B) \neq S^m(-B)$. In

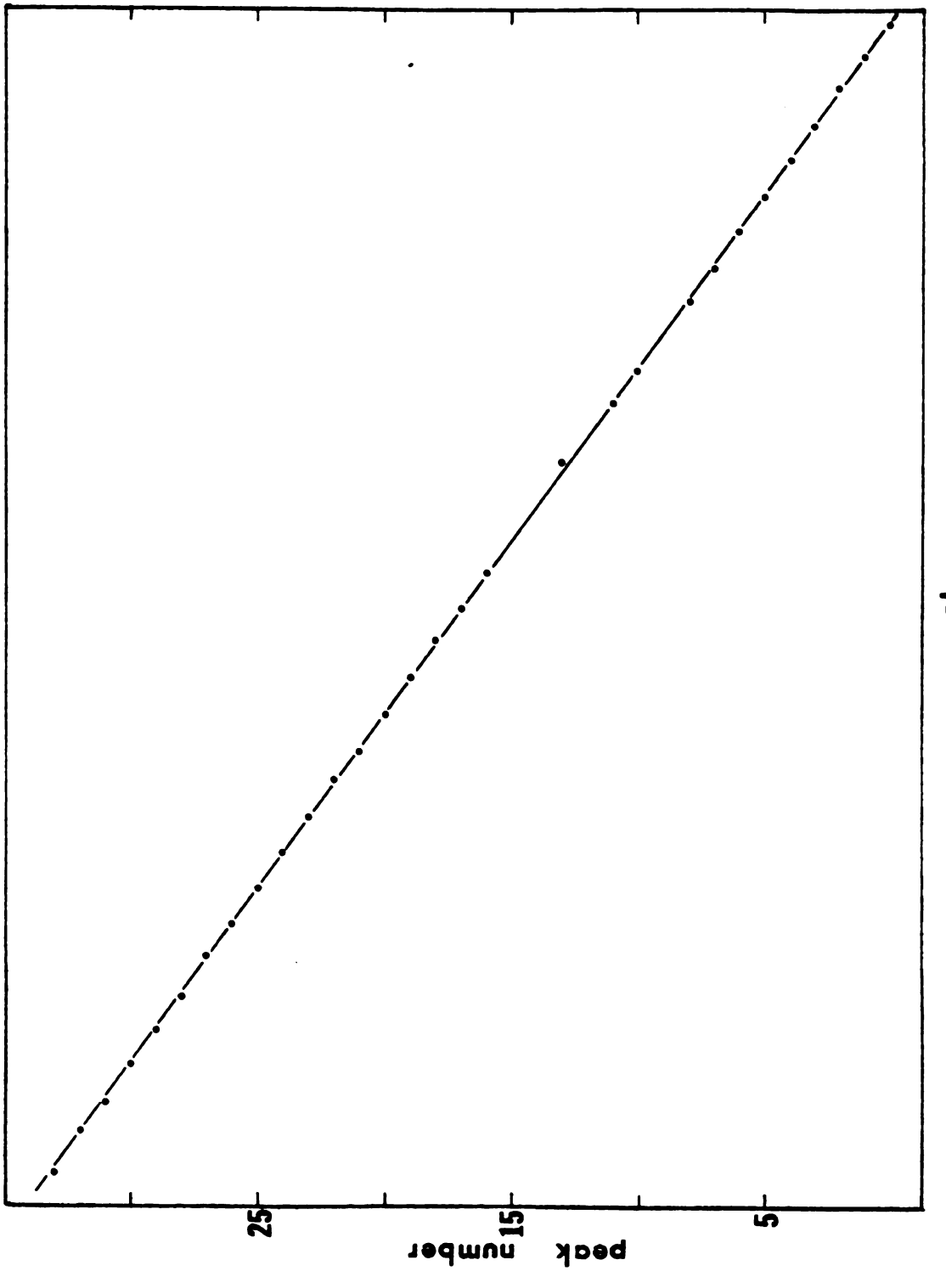

Figure 5.3 Frequency of S^a oscillations

fact, this asymmetry was so severe for the Cd crystal that S^m actually changed sign under field reversal at the lower temperatures as is seen in Figure 5.4. However, the thermopower (S^a) is expected to be symmetric as can be deduced either from Equation (2.15) or by using a similar argument to the one used in proving

$$\rho_{xx}(B) = \rho_{xx}(-B) \tag{3.8a}$$

since S^a can be thought of as the xx component of a transport tensor.

Our first reaction was that the difference between $S^m(B)$ and $S^m(-B)$ arose from ineaxact alignment of the crystal with respect to the magnetic field direction. To check on this possibility, the W crystal was purposely misaligned by ~0.5° prior to one run--the results for S^m were consistent with our other data to within experimental accuracy. This meant that if misalignment was the cause of the asymmetry, then, for some unknown reason, it must be more severe than ~1°.

To check out this possibility, one run for the Cd crystal and two runs for the W crystal were made using a cryostat designed by J. Cleveland to be used in conjunction with a rotatable 20 kG electromagnet. These runs indicated that changes in the magnetic field orientation by as much as 20° resulted in changes of the measured thermopower of ≤20%. Therefore, crystal misalignment with respect to the magnetic field direction was ruled out as the source of the asymmetric behavior of S^m under field reversal.

The next most likely candidate for the source of the asymmetry was misalignment of the measurement probes with respect to the heat current axis. As shown in Appendix D, if the measurement probes were misaligned relative to the heat axis by a small angle θ then a contribution due to

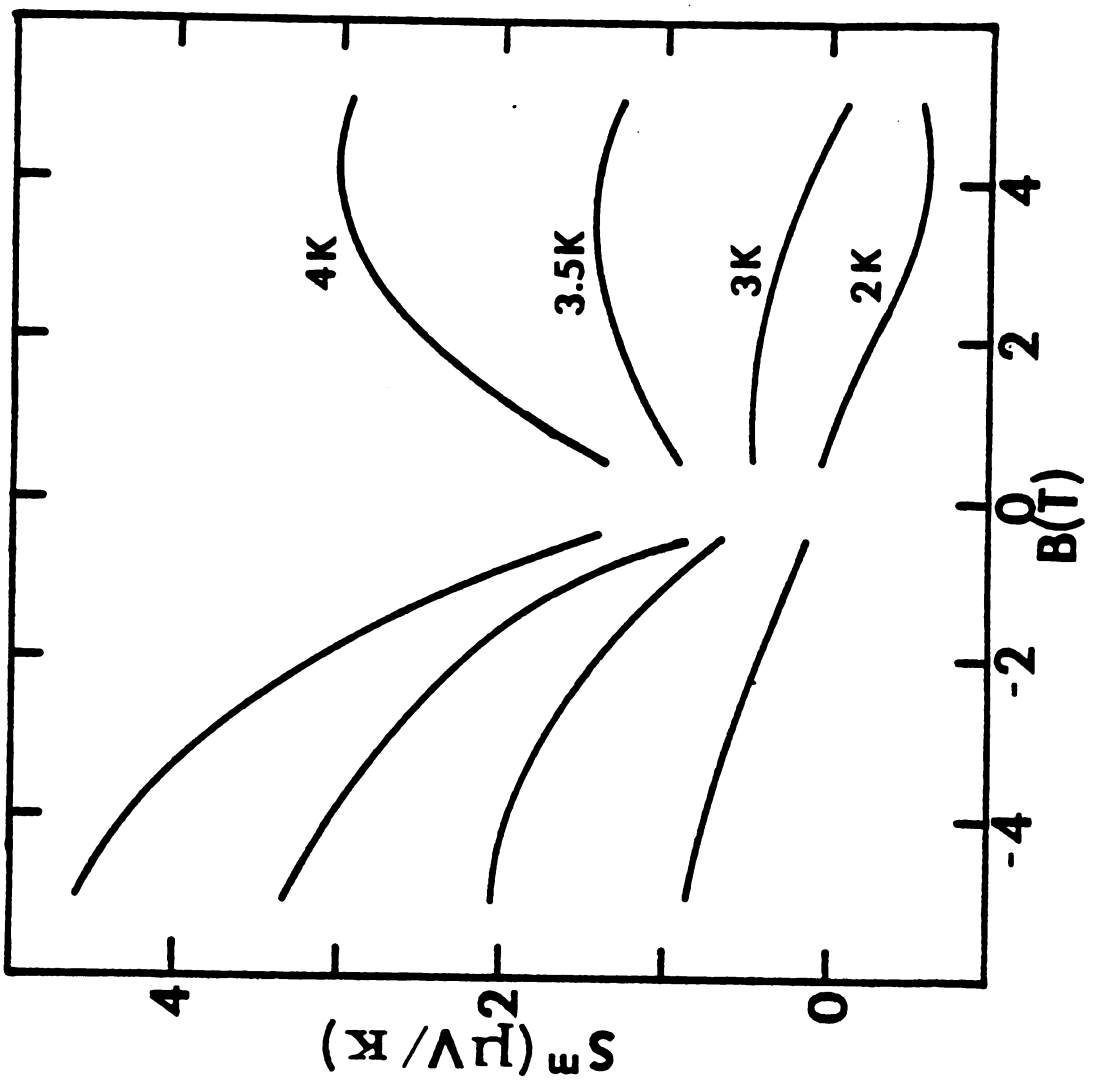

Figure 5.4 S^m of Cd

the Nernst-Ettinghausen coefficient Q^a would show up in our S^a measurements and the measured thermopower would be related to the true thermopower by

$$S^m(B) = S^a(B) - Q^a(B) \tan\theta \tag{5.2}$$

We can take advantage of the fact that

$$S^a(B) = S^a(-B) \tag{5.3a}$$

and

$$Q^a(B) = -Q^a(-B) \tag{5.3b}$$

to calculate the true thermopower from our results of S^m by reversing the field and taking the average

$$S^a(B) = \tfrac{1}{2}[S^m(B) + S^m(-B)] \tag{5.4}$$

If this analysis were correct, we should expect that the asymmetric component of S^m, defined as

$$D(B) = \tfrac{1}{2}[S^m(B) - S^m(-B)] \tag{5.5}$$

to be proportional to Q^a

$$D(B) = -Q^a(B) \tan\theta \tag{5.6}$$

The degree to which Equation (5.6) is obeyed can be seen from Figures 5.5 and 5.6 where our results of D for the Cd and W crystals respectively, are plotted as functions of temperature for various magnetic field strengths. The solid curves in these figures represent Q^a multiplied by a constant--the Q^a values for Cd came from our measurements while the Q^a values for W came from Fletcher's results extrapolated from his highest

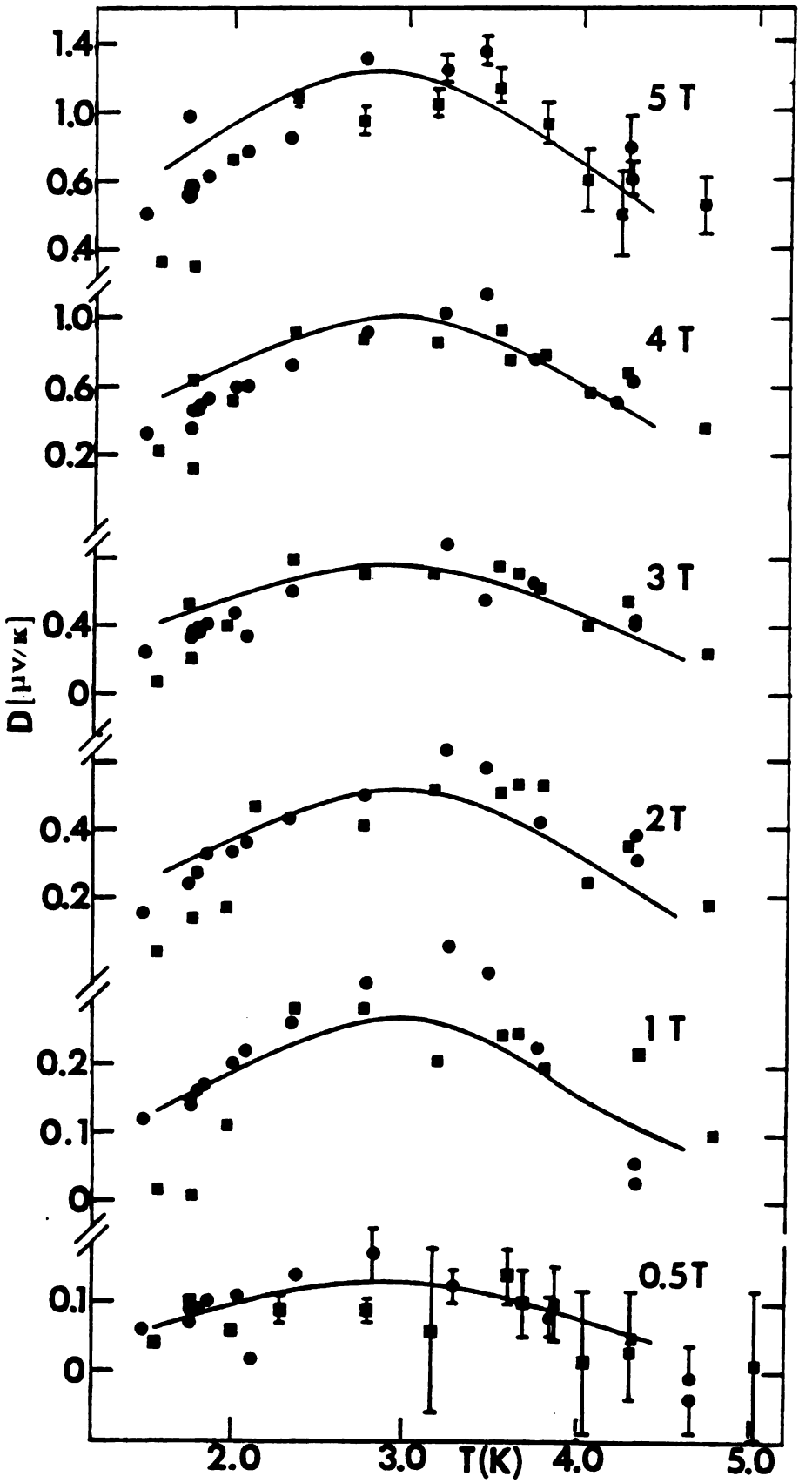

Figure 5.5 D of Cd

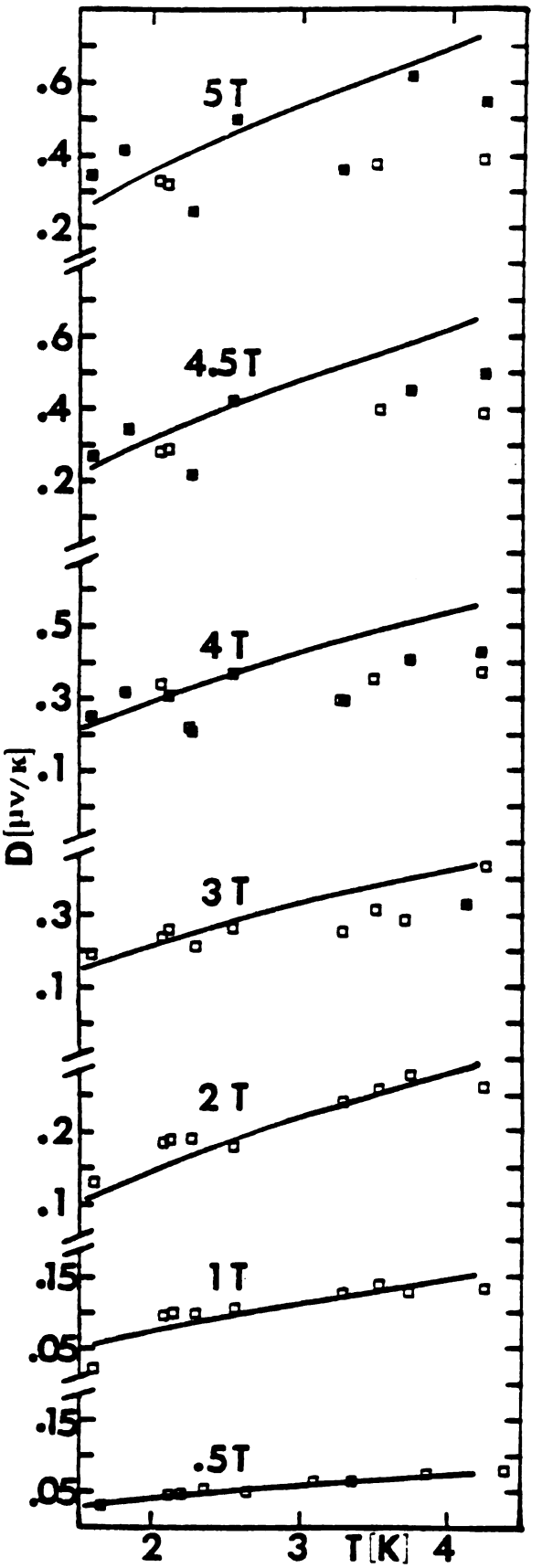

Figure 5.6 D of W

fields of ~35 kG up to 50 kG. The obtained fits are very reasonable, especially at low fields, and the resulting values for θ of 0.86° for the Cd crystal and 0.25° for the W crystal are quite realistic. We therefore believe that the difference between $S^m(B)$ and $S^m(-B)$ is due to probe misalignment and we go on to use Equation (5.4) in determining S^a with confidence. We note in passing that in the Mo studies mentioned earlier, $S^m(B)$ and $S^m(-B)$ were equal to within experimental accuracy. Because of the relatively much smaller Q^a in Mo, the Nernst-Ettinghausen contribution to S^m, for a probe misalignment by as much as 45° (i.e. $\tan\theta = 1$), would amount to only 0.1%; thus it is not surprising that S^m was found to be symmetric under magnetic field reversal.

Shown in Figure 5.7 for Cd and in Figure 5.8 for W are our results for the magnetothermopower, plotted as functions of temperature at various magnetic field strengths.

The next step in the analysis of this S^a data is to investigate the possibility of separating the diffusion from the phonon drag contributions. The traditional method of performing this separation has been to try to fit the data to the form

$$S^a = aT + bT^3 \tag{5.7}$$

where the T and T^3 terms correspond to the diffusion (S^d) and the phonon drag (S^g) thermopower components respectively. Fletcher et al.[1] plotted S^a/T against T^2 for their Mo crystal and were able to separate the contributions S^d and S^g from the resulting linear plots. However, they went on to point out that the T^3 part may include a contribution from the diffusion thermopower due to the temperature variations of the parameters which occur in Equation (2.15). Thus Equation (5.7) should

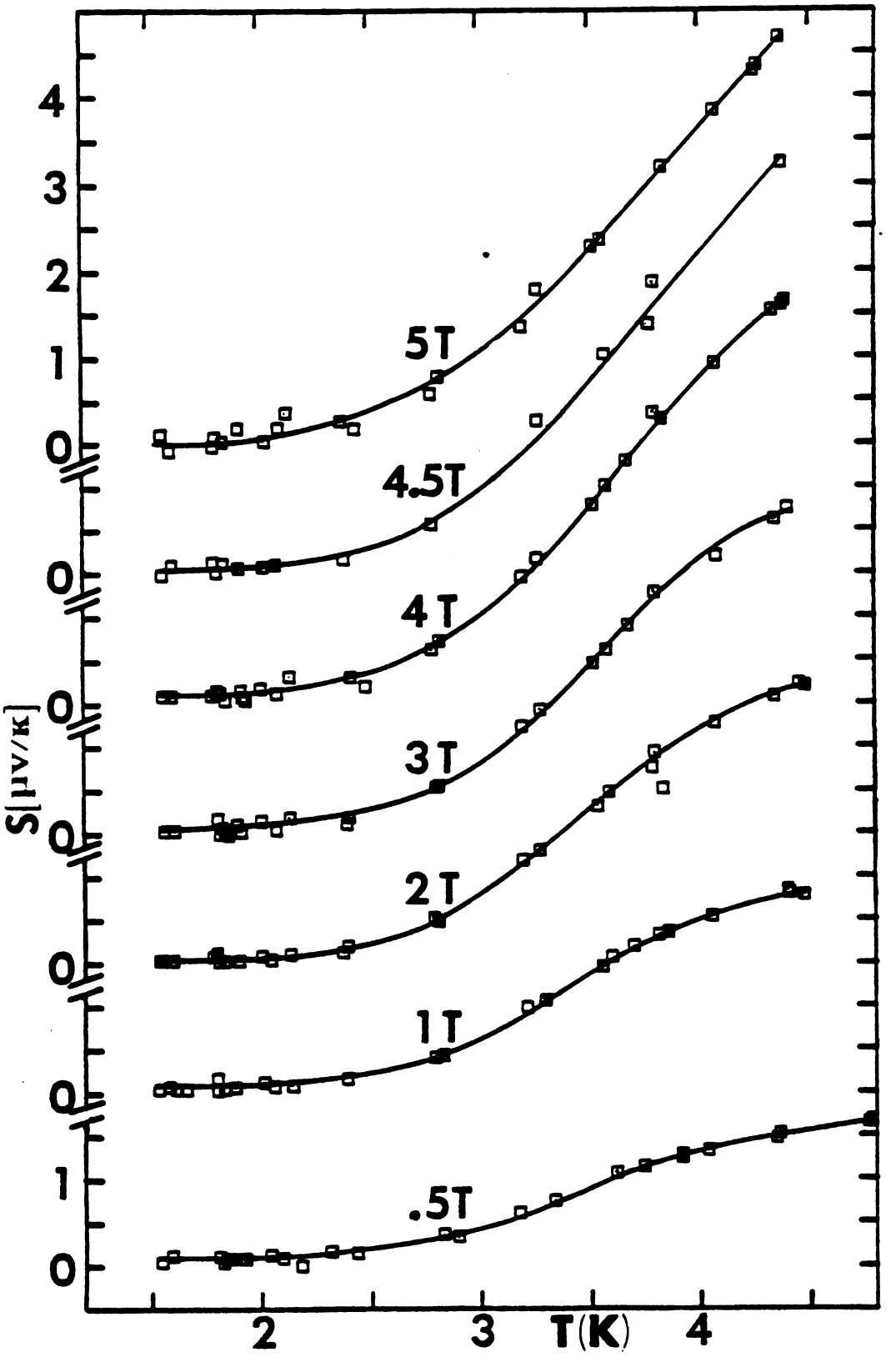

Figure 5.7 S^a of Cd

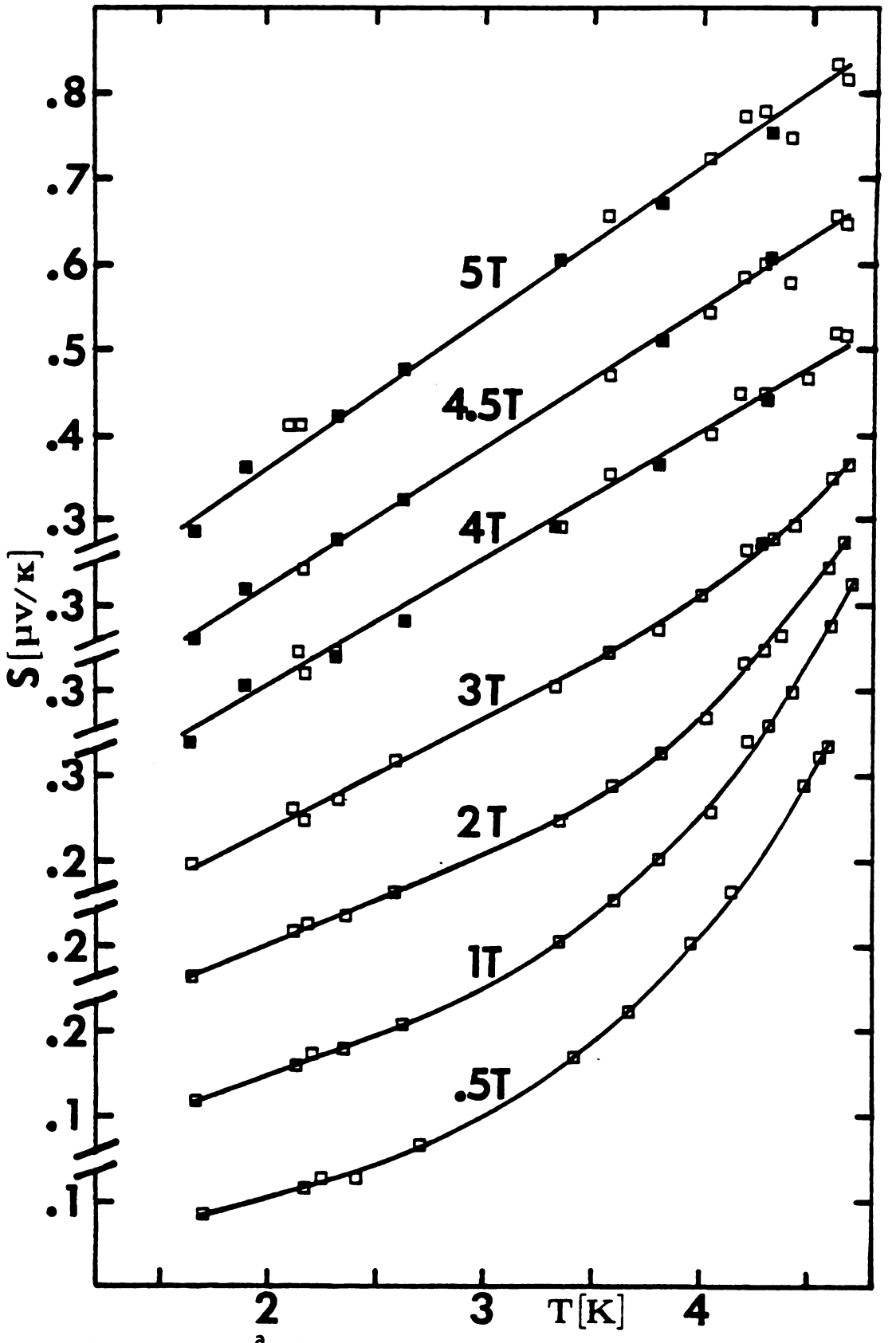

Figure 5.8 S^a of W

be treated with a certain amount of skepticism. Our plots of S^a/T versus T^2 shown in Figures 5.9 and 5.10 for Cd and W respectively, indicate that for these systems Equation (5.7) is not a valid fit.

Since we are primarily concerned with the diffusion thermopower as far as the magnetic field dependence is concerned, the best we can do under the circumstances is to study the extrapolated values of $S^a/T\Big|_{T\to 0}$. Our results are plotted in Figure 5.11 and indicate a linear dependence on the magnetic field. Although this field dependence is not consistent with the saturation of S^a predicted at the start of the investigation, it is consistent with our new interpretation of the high field theory of LAK discussed in Section 3.

The thermopower, given by Equation (2.15), can be written as

$$S^a = -\rho_{xx}\varepsilon_{xx}\left[1 - \frac{\gamma_{yx}}{\gamma_{xx}}\frac{\rho_{yx}}{\rho_{xx}}\right] + \rho_{yx}\varepsilon_{yx}\left[1 + \frac{\gamma_{yx}}{\gamma_{xx}}\frac{\rho_{xx}}{\rho_{yx}}\right] \tag{5.8}$$

For both Cd and W, Fletcher's measurements[4,5,6] indicate that $(\gamma_{yx}/\gamma_{xx})\rho_{yx}/\rho_{xx} \ll 1$, so to a good approximation

$$S^a = -\rho_{xx}\varepsilon_{xx} + \rho_{yx}\varepsilon_{yx}\left[1 + \frac{\gamma_{yx}}{\gamma_{xx}}\frac{\rho_{xx}}{\rho_{yx}}\right] \tag{5.9}$$

The term in parenthesis in Equation (5.9) is complicated at finite temperature, however, for $T \to 0$, $(\gamma_{yx}/\gamma_{xx})(\rho_{xx}/\rho_{yx}) \to 1$. Therefore

$$S^a/T\Big|_{T\to 0} \simeq -\rho_{xx}\varepsilon_{xx}/T + 2\rho_{yx}\varepsilon_{yx}/T \tag{5.10}$$

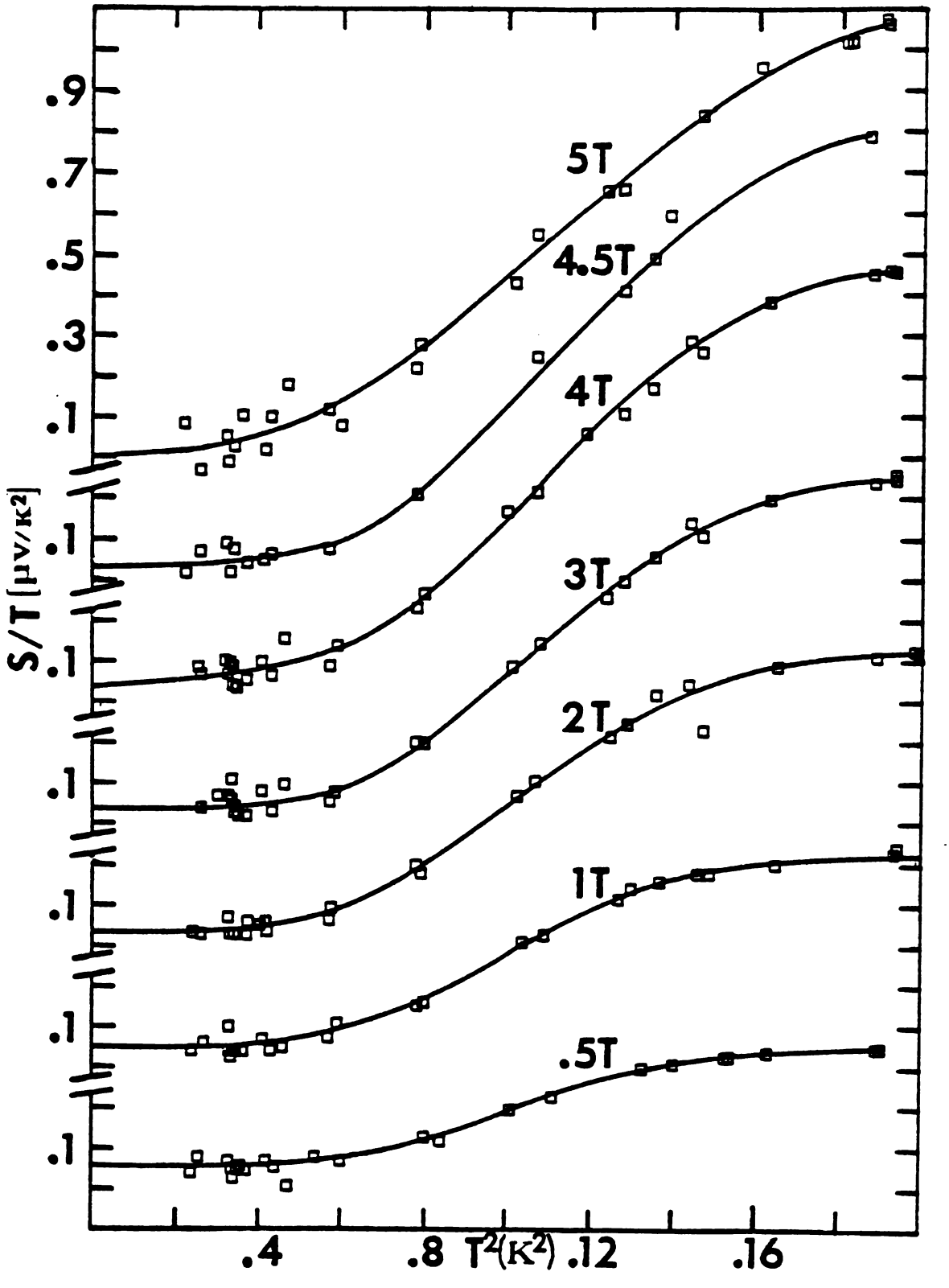

Figure 5.9 S^a/T for Cd

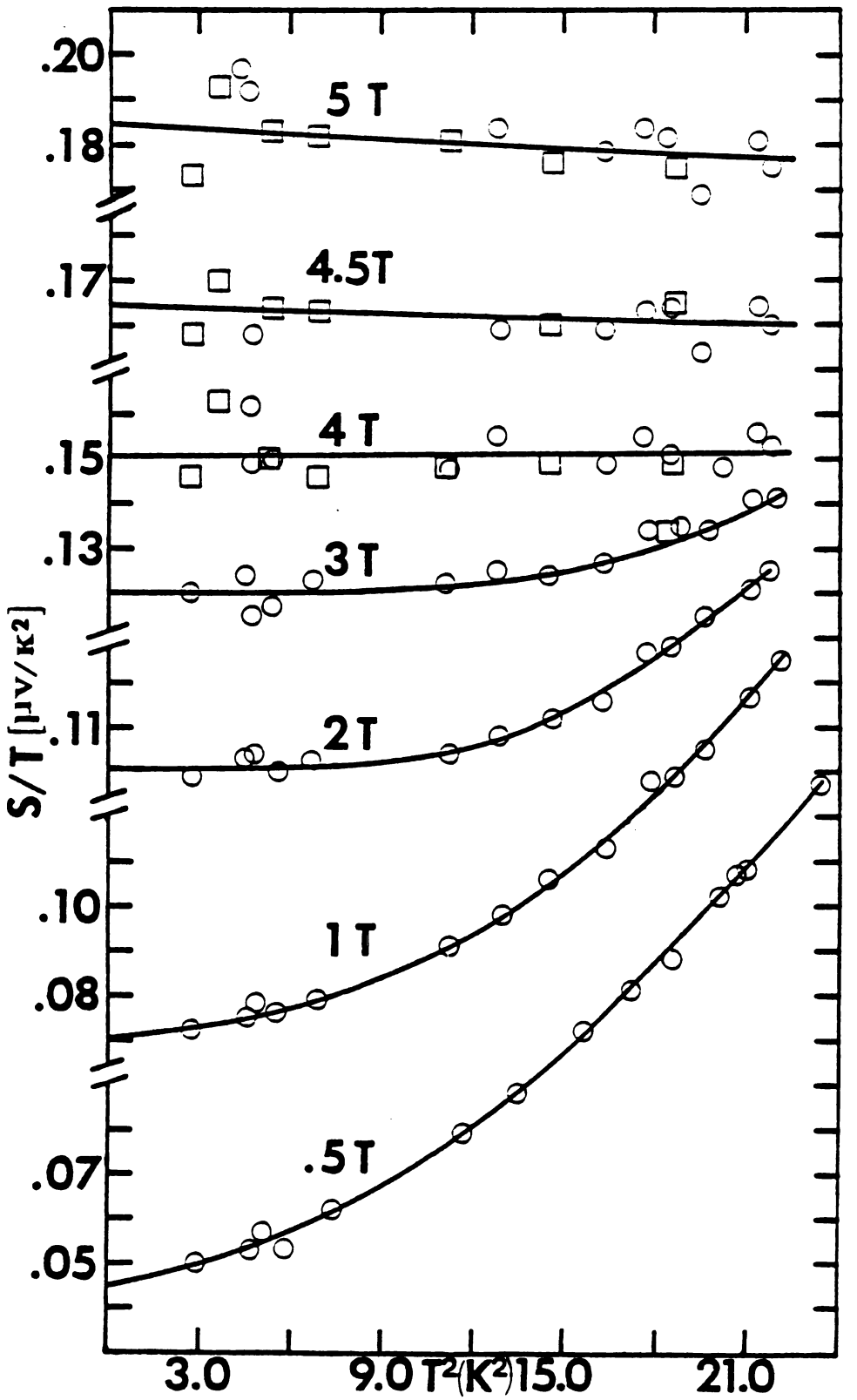

Figure 5.10 S^a/T for W

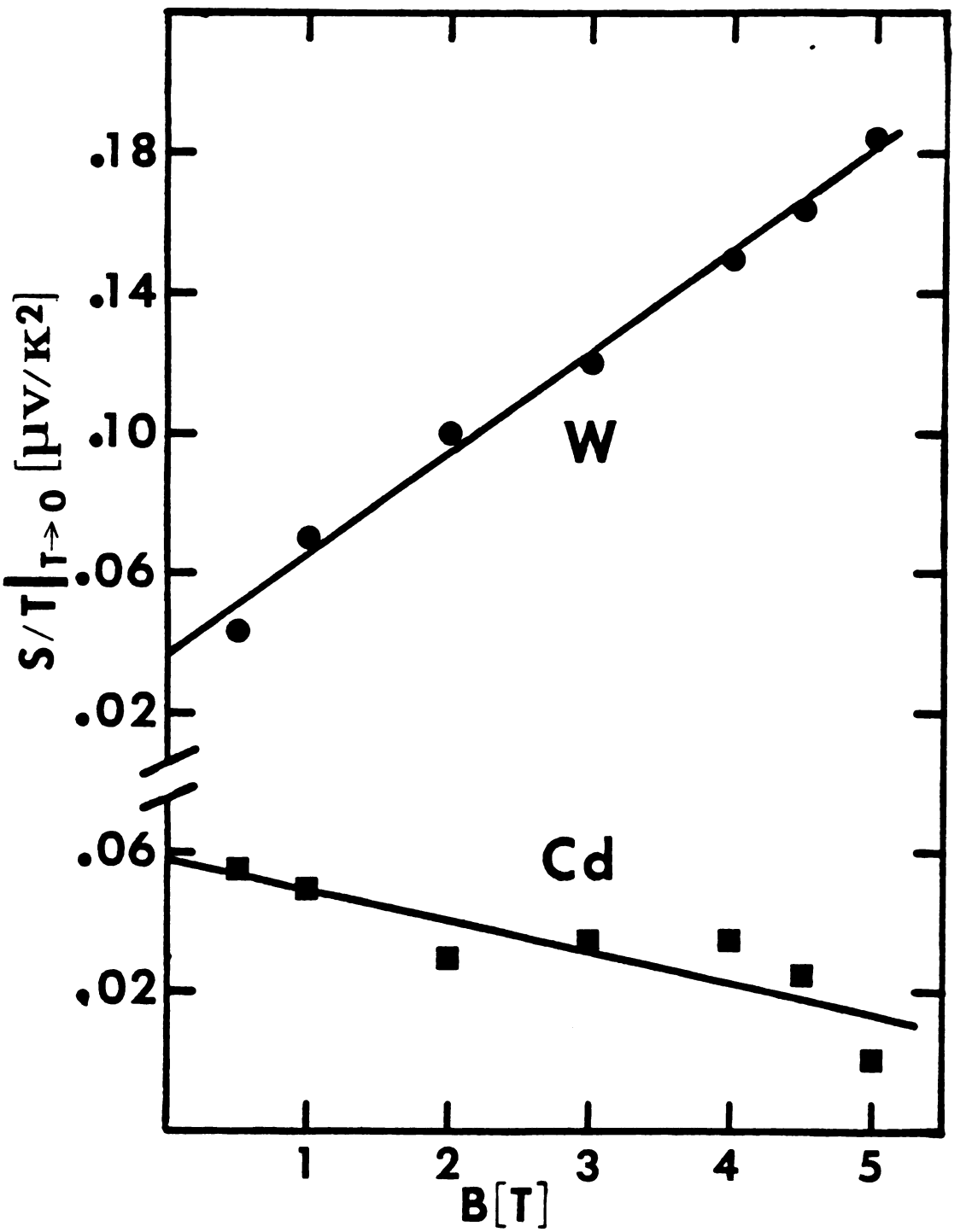

Figure 5.11 $S^a/T\big|_{T\to 0}$ for Cd and W

The LAK theory predicts that ρ_{xx} should show a B^2 magnetic field dependence at high fields and is observed to do so for these Cd and W crystals. From Equations (2.35) and (3.11) the theory also predicts that ε_{xx} should approach a $1/B^2$ behavior. We have extracted values of ε_{xx} for this W crystal from our measurements of S^a and Fletcher's measurements of $\overleftrightarrow{\rho}$, $\overleftrightarrow{\gamma}$ and ε_{yx} using Equation (5.9). Since one expects that ε_{xx} should depend linearly on temperature at low temperatures (see Equation (2.35)), which implies that

$$B^2\varepsilon_{xx} \propto T \tag{5.11}$$

we present our results for ε_{xx} in Figure 5.12 in the form of $B^2\varepsilon_{xx}$ versus T. There is considerable uncertainty in these results arising from the many terms in Equation (5.9), however, they do show that Equation (5.11) is substantially correct in that the data is consistent with parallel straight line fits passing through the origin--particularly at high fields. Therefore we conclude that the first term in Equation (5.10) saturates in high magnetic field.

For the second term in Equation (5.10), Fletcher found experimentally that $\varepsilon_{yx}/T \propto B^{-1}$ as expected from theory. With his other results of $\rho_{yx} \sim -aB^{1.9}$ for Cd below 3 K and $\rho_{yx} \sim bB + cB^2$ for W (a,b,c, are all positive) it is clear that the term $\rho_{yx}\varepsilon_{yx}/T$ is the source of the linear field dependence seen in our $S^a/T\Big|_{T\to 0}$ data.

As discussed in Section 3, this B^2 dependence of ρ_{yx} found experimentally by Fletcher, which appears in our thermopower measurements, is no longer unexpected and is now consistent with the high field theory of LAK. And, no behavior arising from non-compensation was observable for these "pure" samples as expected, i.e. no B^3 term was discernable in the results of ρ_{yx}.

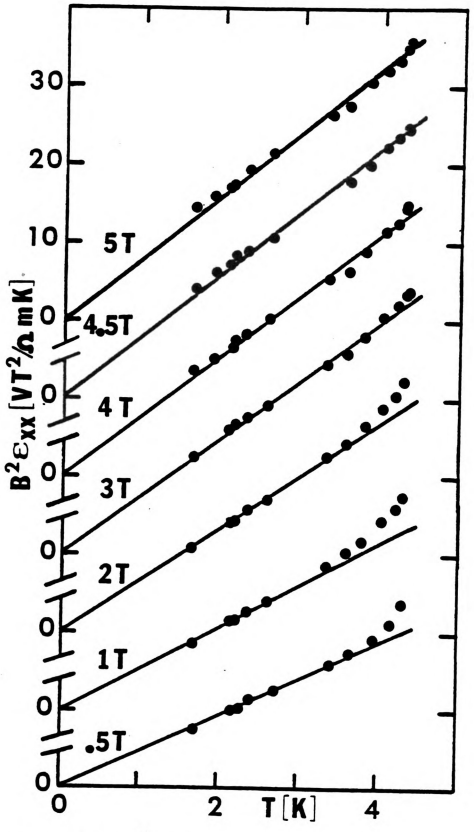

Figure 5.12 $B^2\varepsilon_{xx}$ of W

CHAPTER II

$Ti_{1+x}S_2$

6. INTRODUCTION

The layered compound titanium disulphide (TiS_2) has received considerable attention in recent years, not only because of its potential practical use as the cathode material in lithium-anode intercalation chemistry batteries[21] but also because of the unusual T^2 temperature dependence seen in its a-axis electrical resistivity.

Although it is agreed that TiS_2 exhibits metallic conduction, the origin of the carriers remains controversial. Early investigators considered TiS_2 to be a degenerate semiconductor with extrinsic conduction electrons arising from excess titanium.[22,23] It is well known that TiS_2 tends to grow metal rich and the excess titanium atoms in non-stoichiometric $Ti_{1+x}S_2$ are assumed to be donors, with each Ti atom yielding four electrons to the conduction band.

More recently, with improved materials preparation techniques, it has become possible to prepare highly stoichiometric titanium disulphide. Takeuchi and Katsuta[24] and Thompson et al.[25] have reported the preparation of $Ti_{1+x}S_2$ with $x \leq 0.001$. Investigations have found that even these highly stoichiometric materials exhibit significant conductivity. More specifically, Thompson reported[26] that the resistivity of titanium disulphide depended on temperature as $\rho(T) = a + bT^2$ and

depended on the carrier concentration as $n^{-5/3}$, both of which are characteristic of carrier-carrier scattering.[27] Thompson then concluded that the metallic behavior of titanium disulphide is an intrinsic effect and that TiS_2 is not a semiconductor but is a semimetal. These contradictions to long-held beliefs generated a lot of interest in TiS_2 from other researchers.

Kukkonen and Maldague[28] theoretically examined the semimetal picture of TiS_2 and argued that the carrier-carrier scattering must be electron-hole scattering; both electron-electron and hole-hole scattering are prohibited in TiS_2 because the assumed carrier pockets in TiS_2 are too small and well separated to allow umklapp scattering processes to occur. Furthermore, their investigation predicted that in stoichiometric TiS_2, electron-hole scattering would produce a T^2 behavior of the resistivity for all temperatures, but off stoichiometry ($n_e \neq n_h$), their results predicted a T^2 dependence only at low temperatures, with a slower temperature dependence at higher temperatures.

In opposition to this new semimetal view, the work of other researchers continued to support the semiconductor view of TiS_2. Band calculations have always shown[29,30] an indirect band gap between the p and d bands and second generation calculations[31] with improved treatment of the muffin-tin corrections and basis set are beginning to settle towards the value for this gap of ~+0.5 eV reported from photoemission studies.[32-34] The work of Friend et al.[35] on the pressure dependence of the resistivity and the Hall effect also showed evidence for a band gap in TiS_2. And finally, Wilson[36,37] claimed that the semiconductor model for TiS_2 should not be abandoned because it was actually consistent with the existing data.

Specifically, Wilson argued that anyone attempting to interpret the transport properties of TiS_2 within a semimetallic scheme must first establish that the material is free from defects. Until that time, it is quite reasonable to believe that the source of the residual electrons in stoichiometric TiS_2 (~$2x10^{20}$ electrons/cm^3) is the displacement defects inferred by Takeuchi and Katsuta[24] (vacancy in Ti site/interstitial Ti between the layers). Wilson also claimed that the resistivity data could be explained by Fivaz[38,39] mode homopolar optic phonon scattering. Scattering from the phonons associated with the "breathing" mode of the individual TiS_2 layers results in a temperature dependent resistivity which is approximately T^2 over the temperature range of ~77 to 400 K. (Below 77 K, Wilson asserted that a continuation of the T^2 behavior was not definitive from Thompson's work.)

To try and answer the many questions raised in the literature about TiS_2, a systematic investigation of several physical properties of single crystals of titanium disulphide with varying degrees of non-stoichiometry was begun by Kukkonen et al.[40] at Ford Motor Company. It was our contact with this group that first introduced us to the unusual behavior seen in this system. Because samples of TiS_2 were made available to us courtesy of Kukkonen et al., we decided to repeat and extend down to ~1.5 K the resistivity measurements of Thompson, not only to re-examine the T^2 behavior with an increase in measurement precision, but also to see if this behavior continues below 10 K. Since we also had the capability of introducing magnetic fields, we could measure the magnetoresistivity for the first time and also investigate the dependence of the resistivity on the carrier concentration (derivable from the Hall coefficient) which could then be compared with Thompson's results

suggesting carrier-carrier scattering. In contrast to Thompson's conclusion that TiS_2 is a semimetal, Kukkonen et al. present convincing evidence using their infared reflectivity data that titanium disulphide is a degenerate semiconductor.

7. EXPERIMENTAL TECHNIQUE: $Ti_{1+x}S_2$

7.1 $Ti_{1+x}S_2$ Samples

The single crystals of titanium disulphide used in this study were grown by S. P. Faile at Purdue University using the vapor transport technique with sulfur or iodine as the transport agent. In a typical crystal growth, a charge of TiS_2 powder, either commercially obtained or prepared in-house, was placed at one end of an evacuated quartz tube together with the transport agent. The transport was achieved by establishing a 75-100°C temperature gradient along the tube with the powder at the hot end and growth occurring at the cool end. Highly stoichiometric crystals were obtained when the growth temperature was near 650°C--lower temperatures produced unwanted whiskers of TiS_3 while higher temperatures result in increasingly non-stoichiometric $Ti_{1+x}S_2$. Listed in Table 7.1 are the conditions under which the samples used in this study were grown. Also shown in this table are the carrier concentrations of these samples derived from Hall effect measurements at room temperature using a single carrier model as well as estimates of the stoichiometry x of the samples.*

---

*The values for x were obtained by comparing their c-axis lattice parameters with Thompson's[25] results for the c-axis lattice parameter as a function of x for $Ti_{1+x}S_2$ powder samples. Because of several inconsistencies associated with this procedure at small x, the values for x should not be taken quantitatively but should only be used as an indicator of the relative non-stoichiometry of the various single crystals. (See Kukkonen et al.[40] for a thorough discussion.)

Table 7.1 Characterization of $Ti_{1+x}S_2$ samples

Batch Number	Crystal Number	Growth Conditions	Electron Concentration n	x
164	TS-11 B164 TS-39 B164	Powder from elements sulfur transport growth temp. ~650°C	2.2×10^{20} cm^{-3}	0.006
6	TS-41 B6	Powder from elements sulfur transport growth temp. ~700°C	3.0×10^{20} cm^{-3}	0.008
3	TS-12 B3	Commercial powder iodine transport growth temp. ~700°C	7.5×10^{20} cm^{-3}	0.008
1	TS-40 B1	Commercial powder iodine transport growth temp. ~900°C	34×10^{20} cm^{-3}	0.055

Physically, the samples were in the shape of thin plates, with their c-axes orientated perpendicular to their plate faces. Their thicknesses ranged between 40 and 150 microns while the dimensions of their planar faces were crudely 2 cm x 2 cm.

7.2 Cryostat

To provide both thermal contact and mechanical strength, the crystals were mounted on a sapphire substrate using G.E. varnish. This substrate backing was varnished on to a copper block attached to the cryostat's mounting post (see Figure 7.1). This block had been optically aligned relative to the magnetic field direction to within ¼° (see Appendix B), which means that, in the measurements made in magnetic fields, the field was directed along the c-axis of the $Ti_{1+x}S_2$ crystal.

Four Pt electrical leads (0.006" in diameter) were secured to the saphire backing with ceramic cement before being attached to the crystal using gold paste (Englehard A-1644). The entire length of the Pt wires (~3-6 cm) as well as ~5 cm of the connecting copper wire leads were lagged to the copper block. With this configuration, we are confident that the $Ti_{1+x}S_2$ sample was at the same temperature as our germanium resistance thermometer.

Generally the leads were attached to the sides of the crystals, however, for two samples (TS-11 B164 and TS-12 B3) the leads were attached to the top surface. No effects attributable to these two different lead configurations were observable in our measurements, except possibly, in our magnetoresistance results.

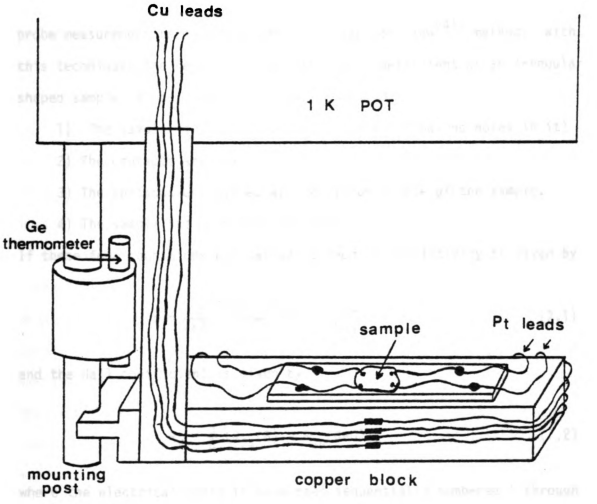

Figure 7.1 Experimental situation for $Ti_{1+x}S_2$ study

7.3 $\rho(T,B)$ and R_H of $Ti_{1+x}S_2$: Measurements

The a-axis electrical resistivity ρ and the Hall coefficient R_H of the titanium disulphide single crystals were measured using the four-probe measurement technique known as the van der Pauw[41] method. With this technique, the resistivity and the Hall coefficient of an irregularly shaped sample can be accurately measured provided:

1) The sample is singly connected. (i.e. it has no holes in it)

2) The contacts are small.

3) The contacts are placed at the circumference of the sample.

4) The sample has a uniform thickness.

If these four conditions are satisfied then the resistivity is given by

$$\rho = \frac{\pi d}{\ell n 2} \frac{(R_{34} + R_{23})}{2} f\left(\frac{R_{34}}{R_{23}}\right) \qquad (7.1)$$

and the Hall coefficient is given by

$$R_H = \frac{d}{B} (R_{24}(B) - R_{24}(B=0)) \qquad (7.2)$$

where the electrical contacts have been sequentially numbered 1 through 4 around the circumference of the sample, d is the thickness of the sample, f(r) is a universal function given by van der Pauw, and R_{ij} is a measured resistance derived from the voltage drop between contacts i and j resulting from a current flowing between the other two contacts--for example, $R_{34} = V_{34}/I_{12}$.

These measurements were made using a lock-in detector as both an A.C. voltmeter and as the A.C. current source. A schematic of the electronics used for the electrical resistivity measurements is shown in

Figure 7.2. A digital voltmeter (D V M) with A.C. voltage capability was used to measure the magnitude of the electrical current flowing through the sample. The output of the PSD was "read" using another DVM. The measurements were conducted using currents of ~1.5 mA at a frequency of 200 Hz. (The results were current and frequency independent to within experimental uncertainty.)

The temperatures at which these measurements were made were determined using the germanium resistor as discussed in Section 4.3. In the studies of the Hall effect and the magnetoresistance (i.e. for measurements in magnetic fields), after a "constant" temperature was obtained by maintaining a constant output from the heater attached to the "one-degree" pot, the temperature was measured in zero field. The voltage measurements in non-zero fields were then made, assuming that the temperature remained constant. Periodically, the field was reduced to zero and the temperature re-measured in order to make corrections to the data due to the small drifts in temperature that occurred. Although these temperature corrections were very small and had a negligible impact on the Hall effect data, they were needed in the analysis of the magnetoresistivity data.

8. $\rho(T,B)$ AND R_H OF $Ti_{1+x}S_2$: RESULTS AND DISCUSSION

8.1 Electrical Resistivity $\rho(T)$

The measurements of the a-axis electrical resistivity ρ for each $Ti_{1+x}S_2$ single crystal were generally made over a time period of approximately 36 hours. Measurements were taken over the temperature range of 77 to 100 K while the system was pre-cooling to nitrogen temperatures, after which, helium was transferred and the measurements over the range

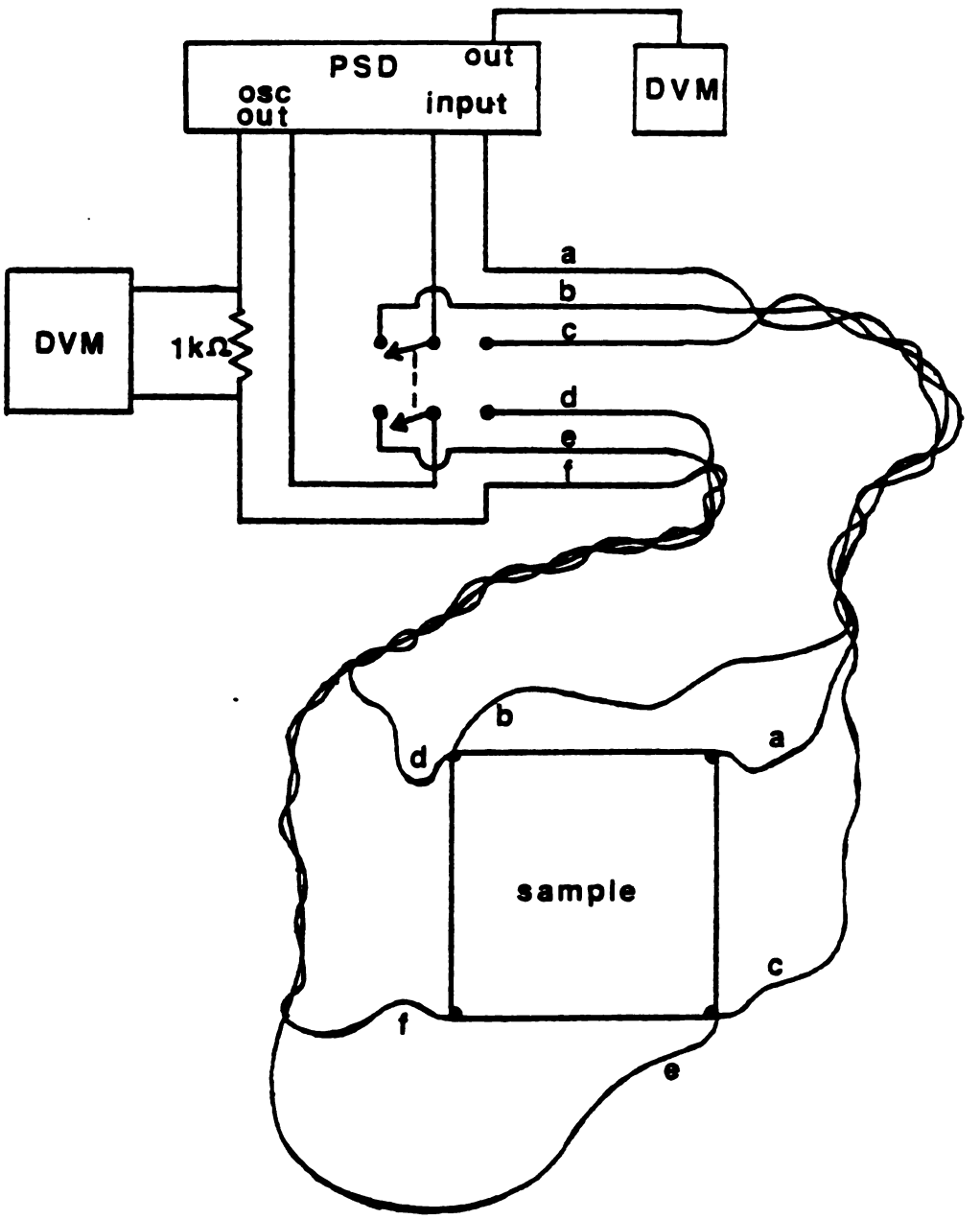

Figure 7.2 Electronics schematic for $Ti_{1+x}S_2$ study

of ~1.5 to ~80 K were taken. The results are shown in Figures 8.1-8.5 where the a-axis electrical resistivity for each sample is plotted against the square of the temperature over the temperature range of ~2 to 100 K. As can be seen, the temperature dependence is not simply T^2 as previously reported,[26] but instead, it depends upon the stoichiometry of the sample. At the higher temperatures, the more stoichiometric samples TS-11 B164, TS-39 B164 and TS-41 B6 depend more strongly on temperature than T^2 while the least stoichiometric sample TS-40 B1 might have a lower dependence than T^2; sample TS-12 B3 has a very nearly T^2 temperature dependence.

These results are consistent with the measurements of Kukkonen et al.[40] on other $Ti_{1+x}S_2$ samples taken from the same batches that our samples came from. They found that their samples did not exhibit a pure T^2 temperature dependence over their range of investigation of 77-700 K. Forcing fits to their data of the form $\rho = \rho_0 + AT^m$, they found that the temperature coefficient m increases with increasing stoichiometry from a low value of 1.85 for the least stoichiometric batch #1 up to a high value of 2.21 for the most stoichiometric batch #164 with $m \simeq 2.03$ for batch #3. Over the range of overlap of 77-100 K, our results are in quantitative agreement with Kukkonen et al.'s results if our results are multiplied by a normalizing factor specific to each sample. This factor presumably arises from our uncertainty in knowing the thickness of each sample (~10-15%).

Further examination of our ρ versus T^2 plots reveals that ρ varies more steeply than T^2 at the lower temperatures. Shown in Figures 8.6-8.10 are our lower temperature data for ρ below 41.5 K. From these plots of ρ versus T^3, it appears as though, at low temperatures, the

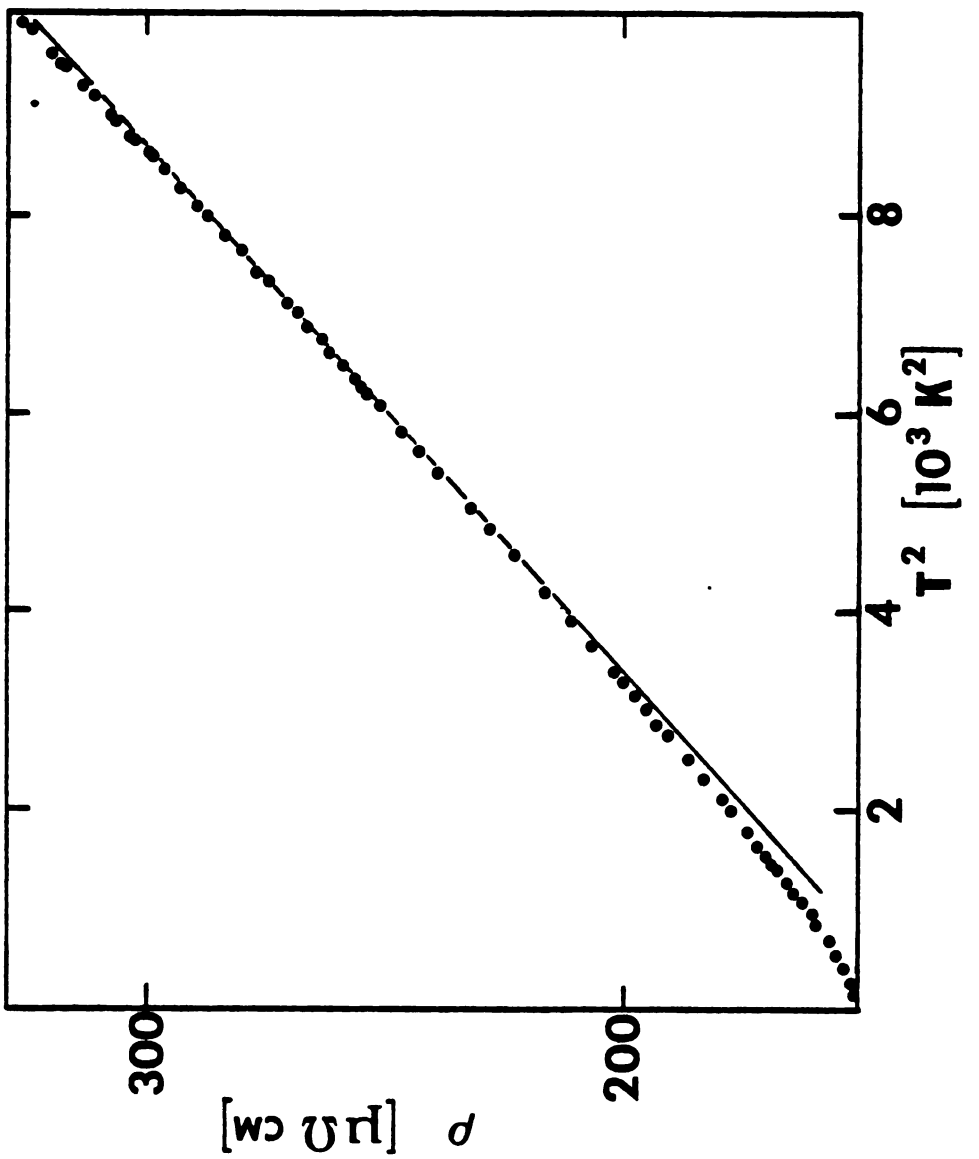

Figure 8.1 $\rho(T)$ vs. T^2 for TS-11 B164

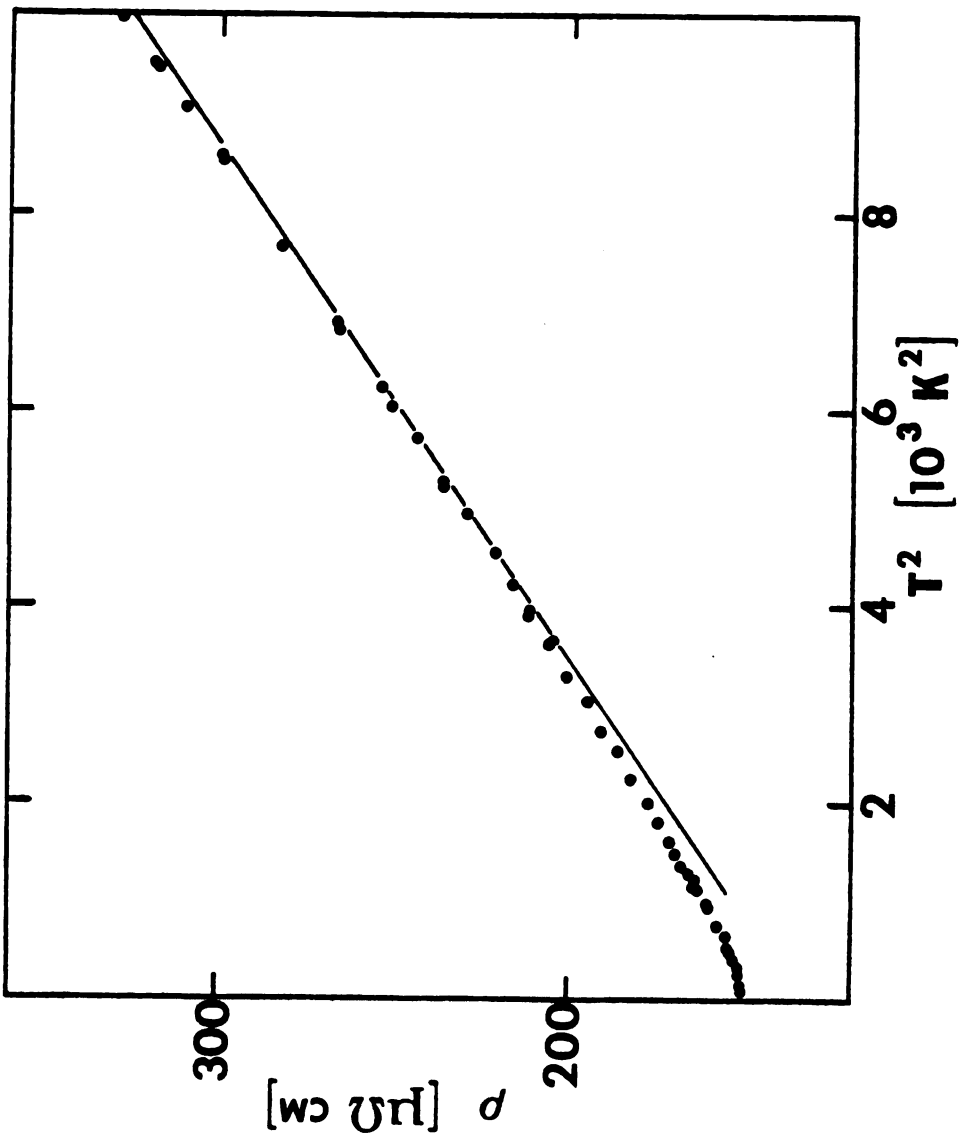

Figure 8.2 $\rho(T)$ vs. T^2 for TS-39 B164

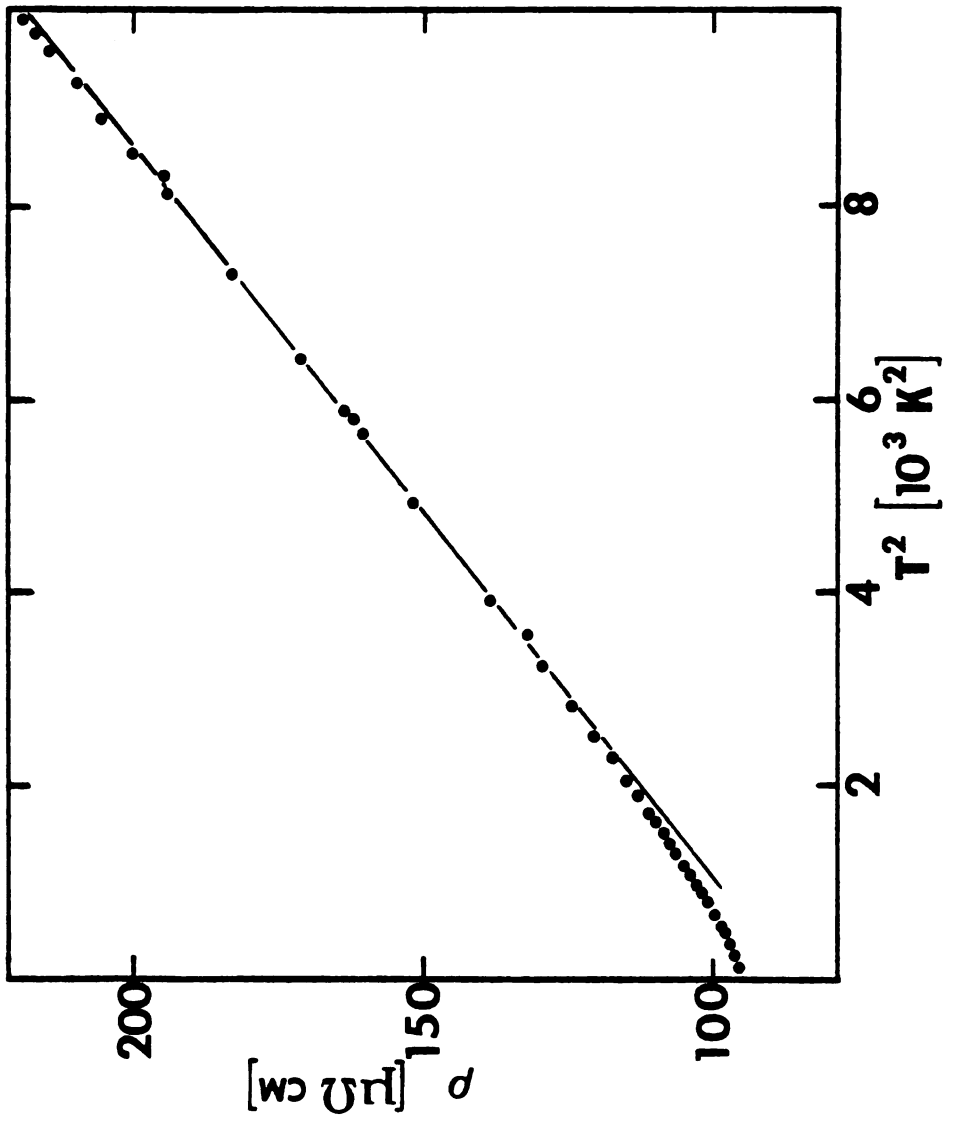

Figure 8.3 $\rho(T)$ vs. T^2 for TS-41 B6

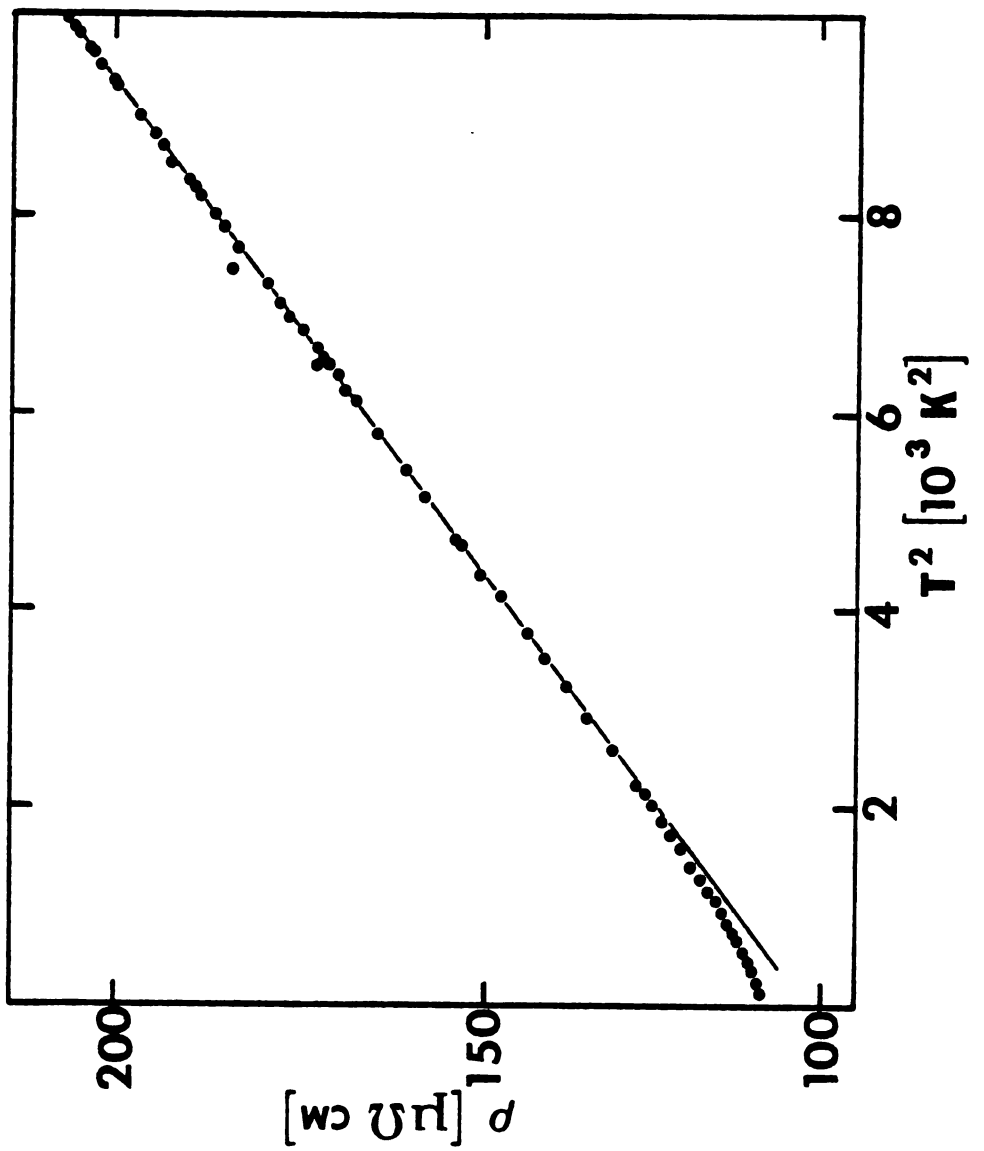

Figure 8.4 $\rho(T)$ vs. T^2 for TS-12 B3

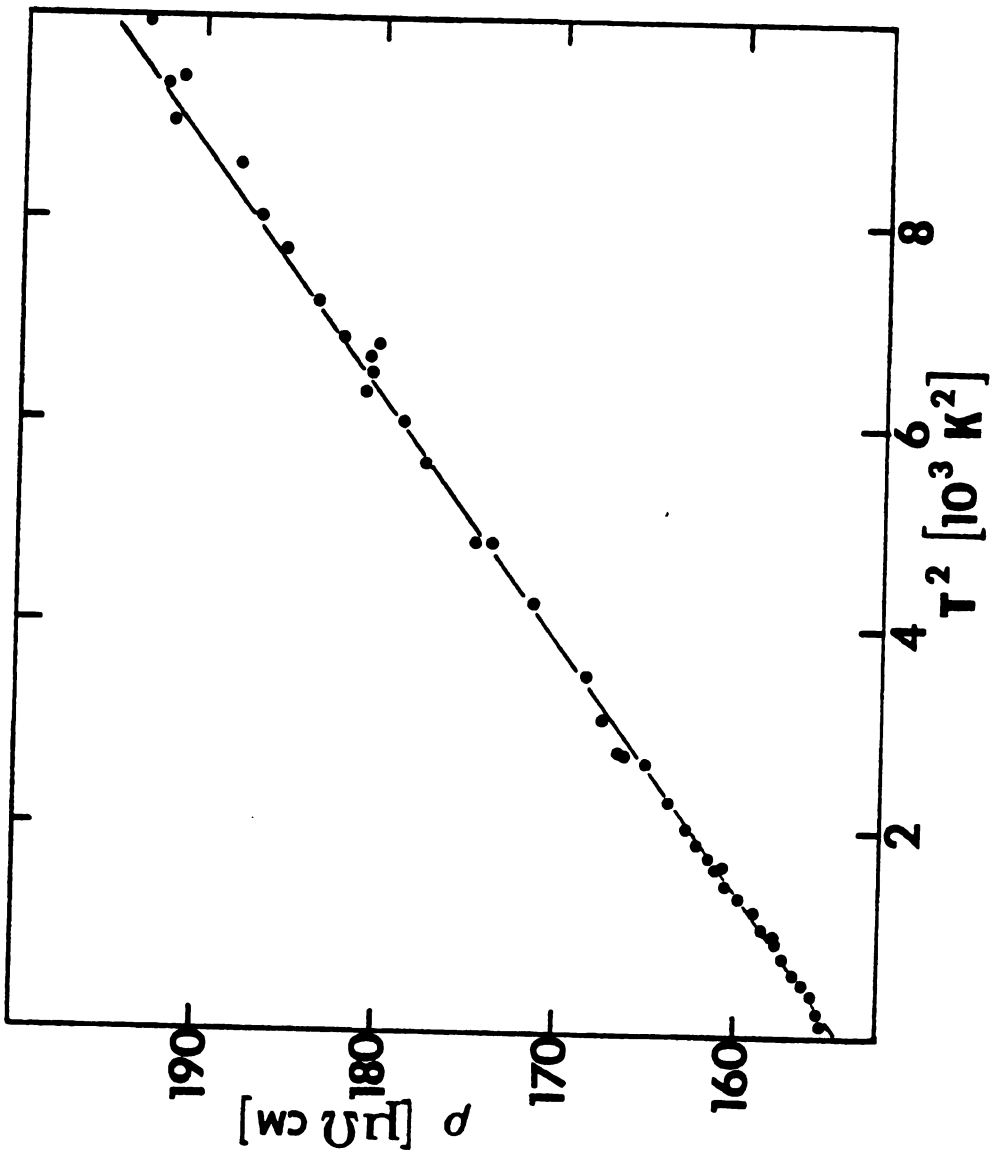

Figure 8.5 $\rho(T)$ vs. T^2 for TS-40 B1

Table 8.1 $\rho(T) = \rho_0 + aT^3$ fits

Sample	ρ_0($\mu\Omega$cm)	a(10^{-3} $\mu\Omega$cm K^{-3}
TS-39 B164	150.20	0.366
TS-11 B164	150.90	0.331
TS-41 B6	95.24	0.250
TS-12 B3	108.65	0.213
TS-40-B1	155-09	0.104

temperature dependence of $Ti_{1+x}S_2$ is very nearly cubic regardless of the stoichiometry of the sample. "Eyeballed" best fits to the data of the form $\rho = \rho_0 + aT^3$ produced the coefficients ρ_0 and a listed in Table 8.1. The solid lines in Figures 8.6-8.10 represent these fits. A further blow up of our ρ data below ~21.6 K is shown in Figures 8.11-8.15, where again ρ is plotted against T^3. These graphs reveal that these same cubic fits remain quite reasonable down to our lowest obtained temperatures of ~1.5 K.

Although this T^3 behavior is independent of the sample stoichiometry, it can be seen from Table 8.1 that there is a systematic trend in the slope "a" of the T^3 dependence--the slope increases with increasing stoichiometry. Also, it appears as though the range of the T^3 behavior increases with increasing stoichiometry as can be seen in Figure 8.16. In this figure the difference between the measured resistivity and the T^3 fit is plotted against T^3. (The temperature dependence of the samples were normalized to sample TS-39 B164 in generating this graph. That is, a change of scale was made so that all the T^3 fits had the same slope.*) The tentative range limits of this T^3 behavior, derived using Figure 8.16, are listed in Table 8.2.

*The data was normalized only for clarity--the results shown in Table 8.2 are unchanged if the original data is used to make a graph similar to Figure 8.16.

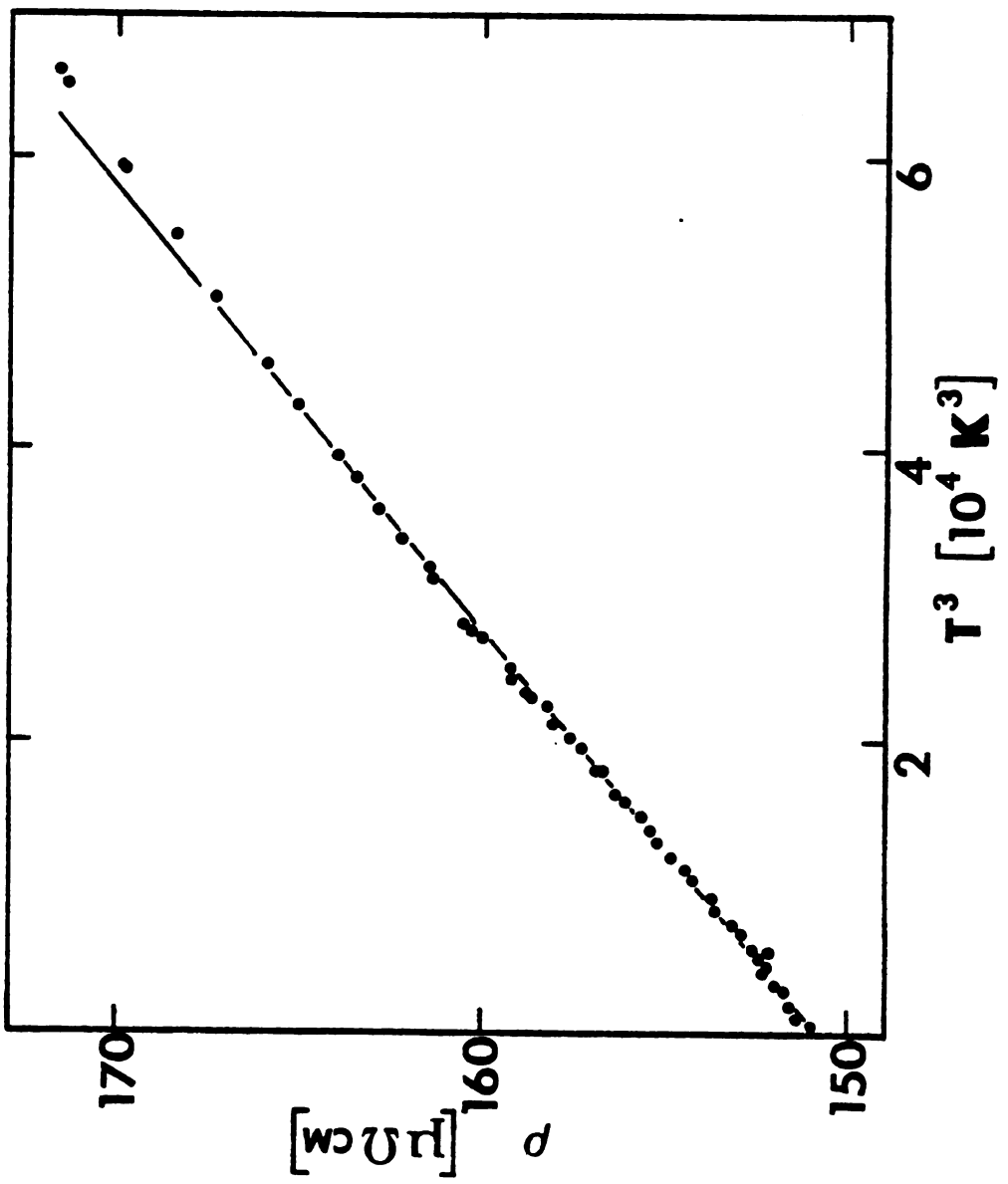

Figure 8.6 $\rho(T)$ vs. T^3 for TS-11 B164

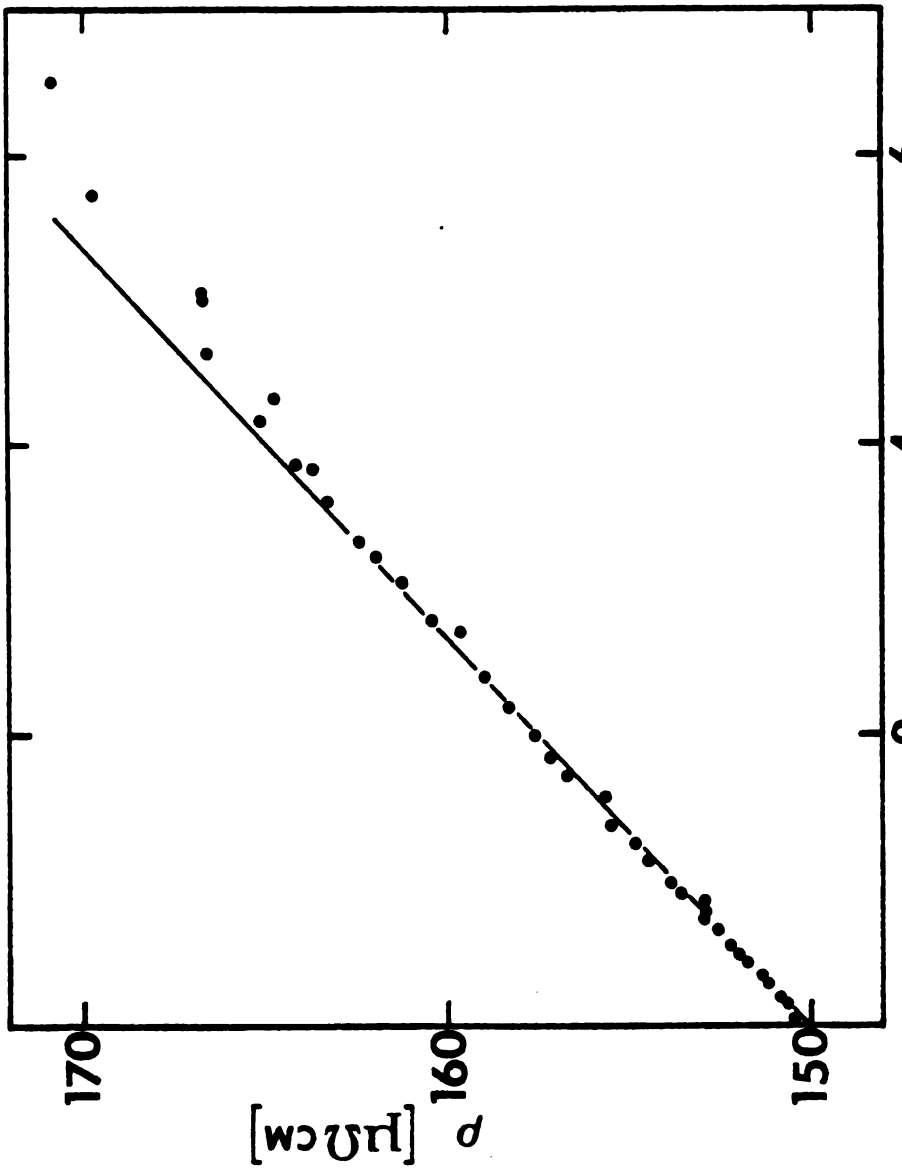

Figure 8.7 $\rho(T)$ vs. T^3 for TS-39 B164

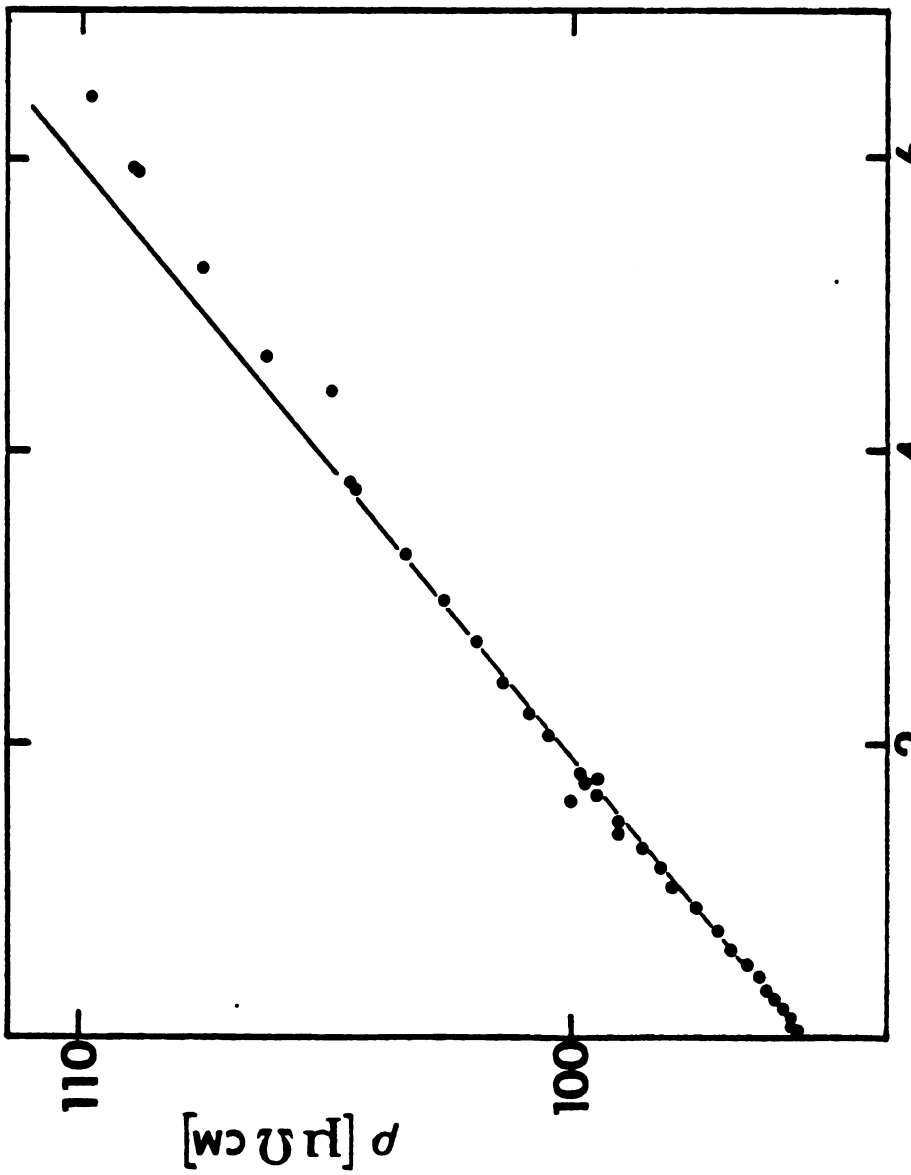

Figure 8.8 ρ(T) vs. T^3 for TS-41 B6

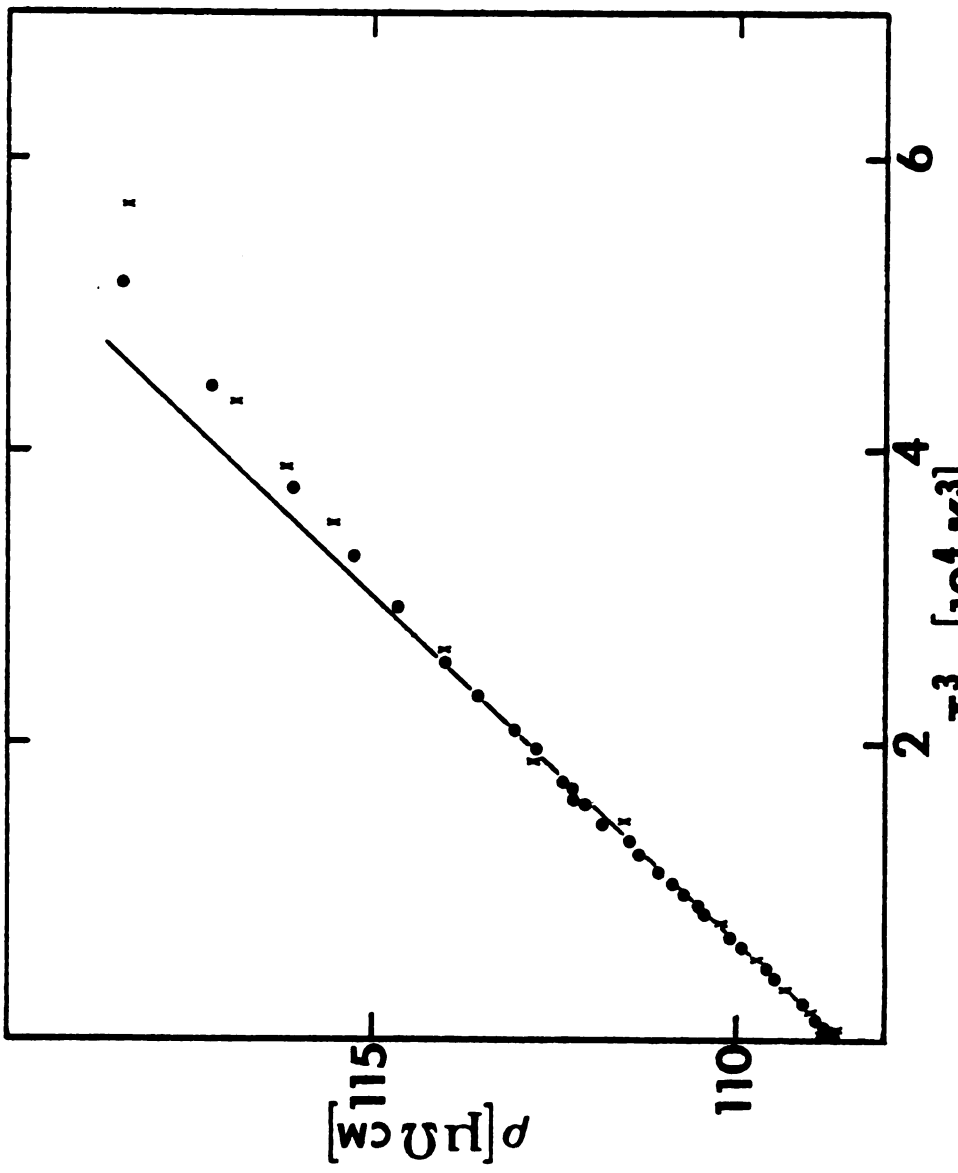

Figure 8.9 $\rho(T)$ vs. T^3 for TS-12 B3

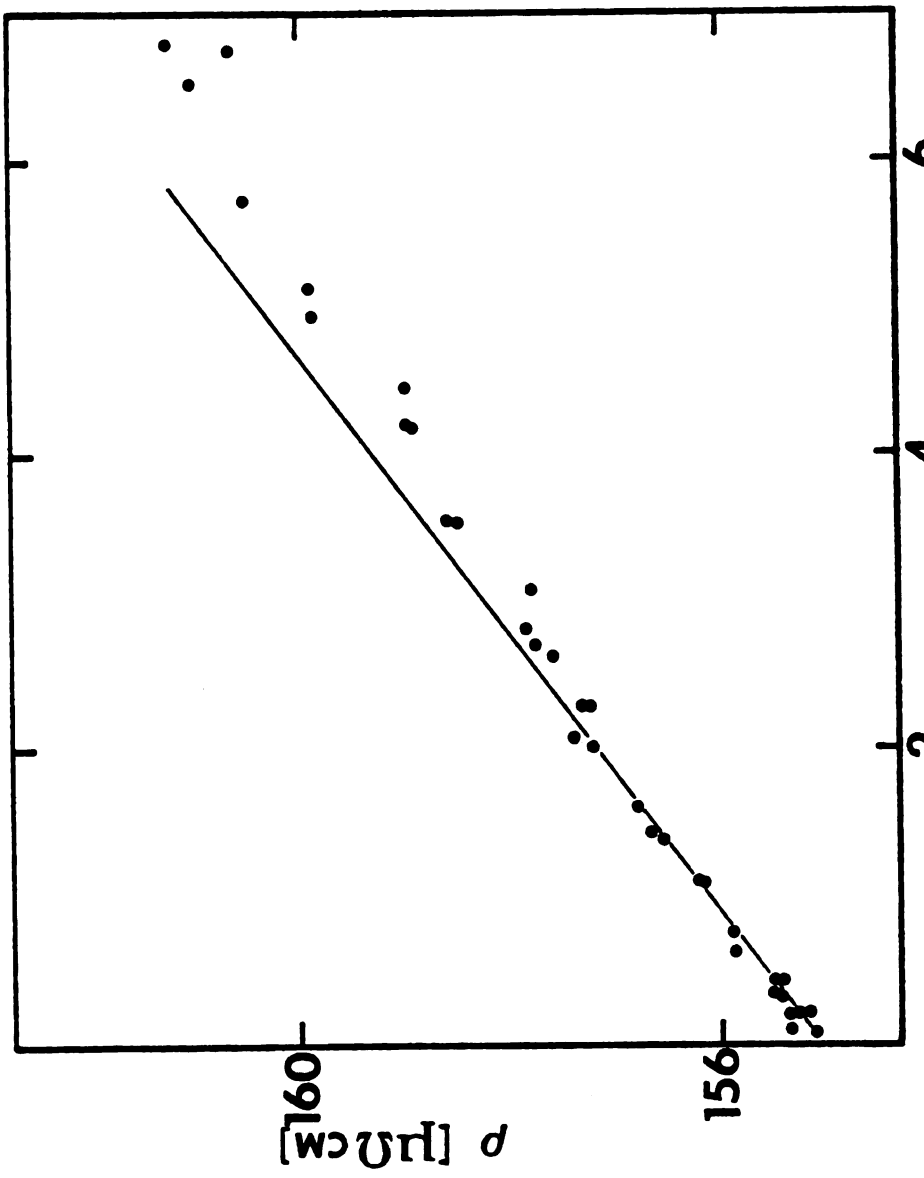

Figure 8.10 ρ(T) vs. T^3 for TS-40 B1

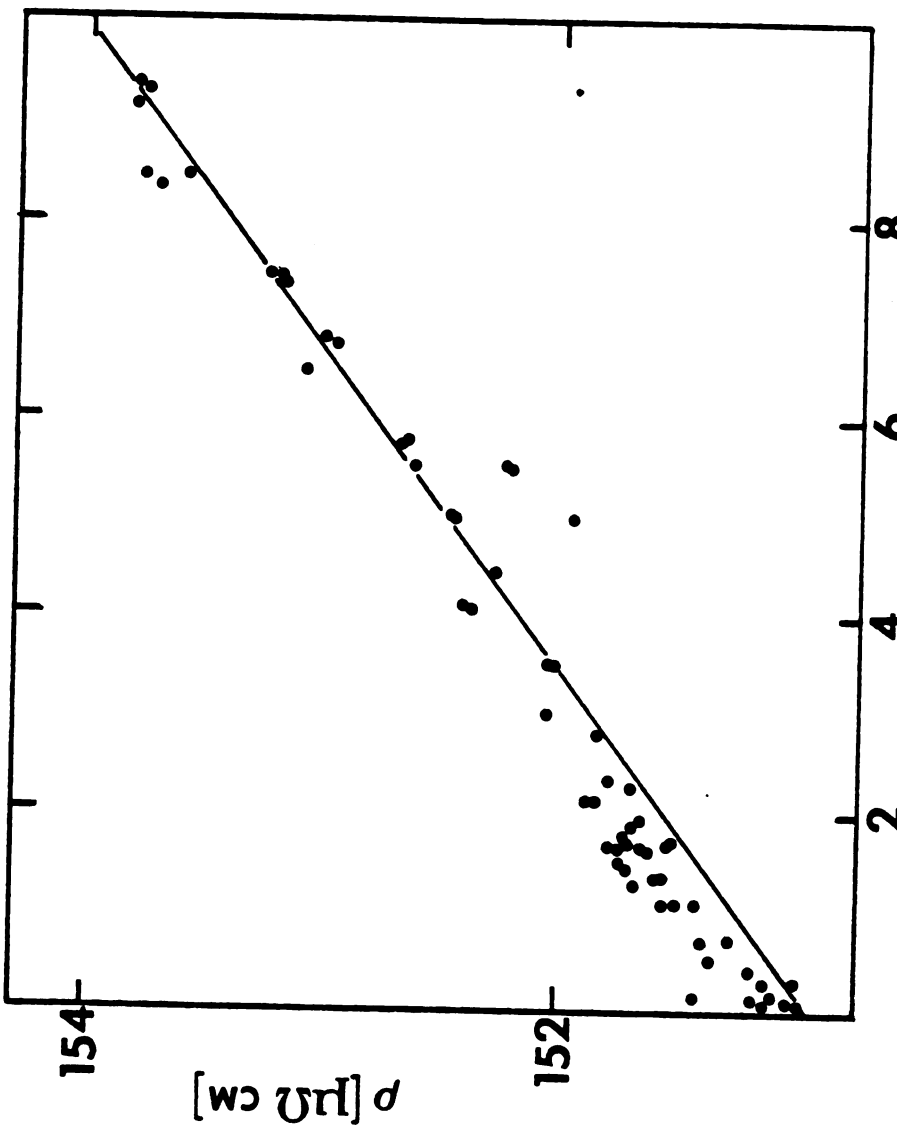

Figure 8.11 ρ(T) vs. T^3 for TS-11 B164 at low T

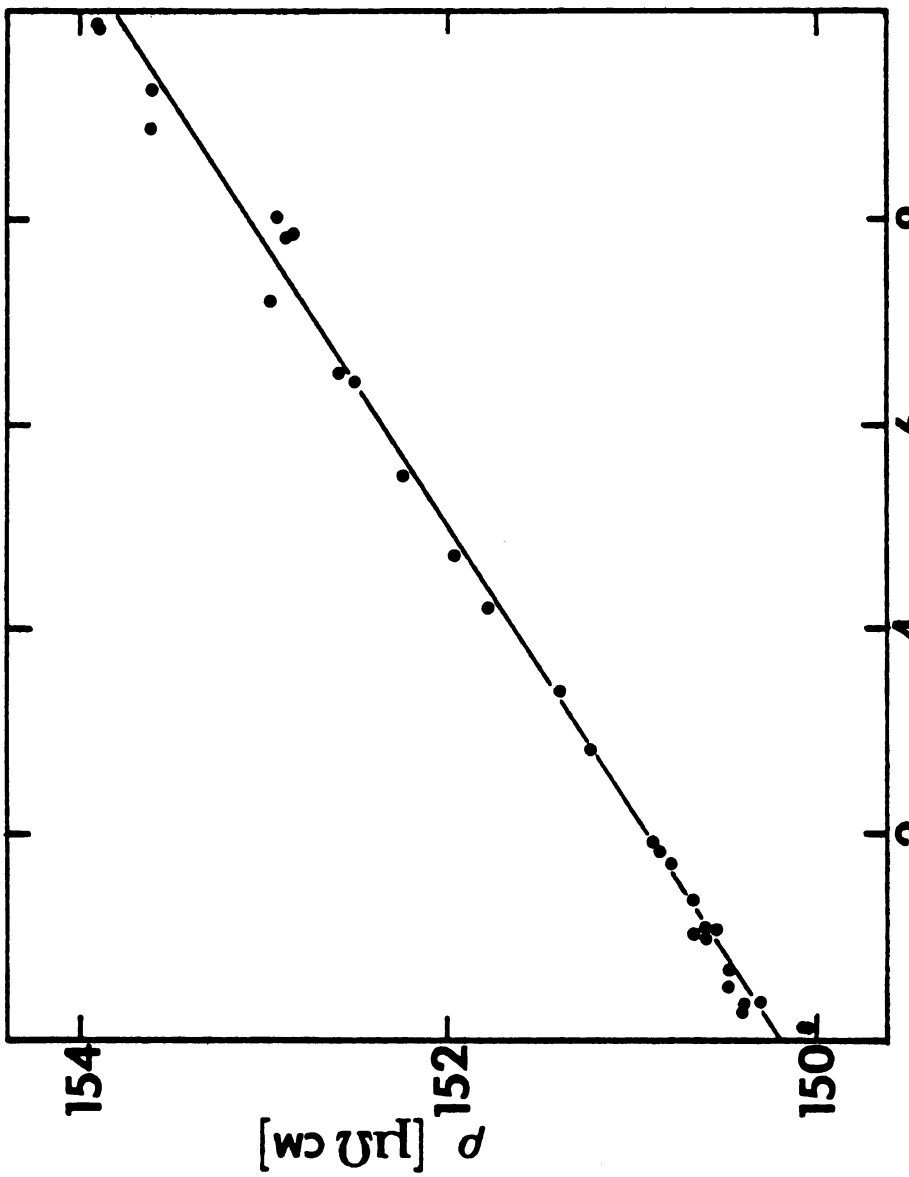

Figure 8.12 $\rho(T)$ vs. T^3 for TS-39 B164 at low T

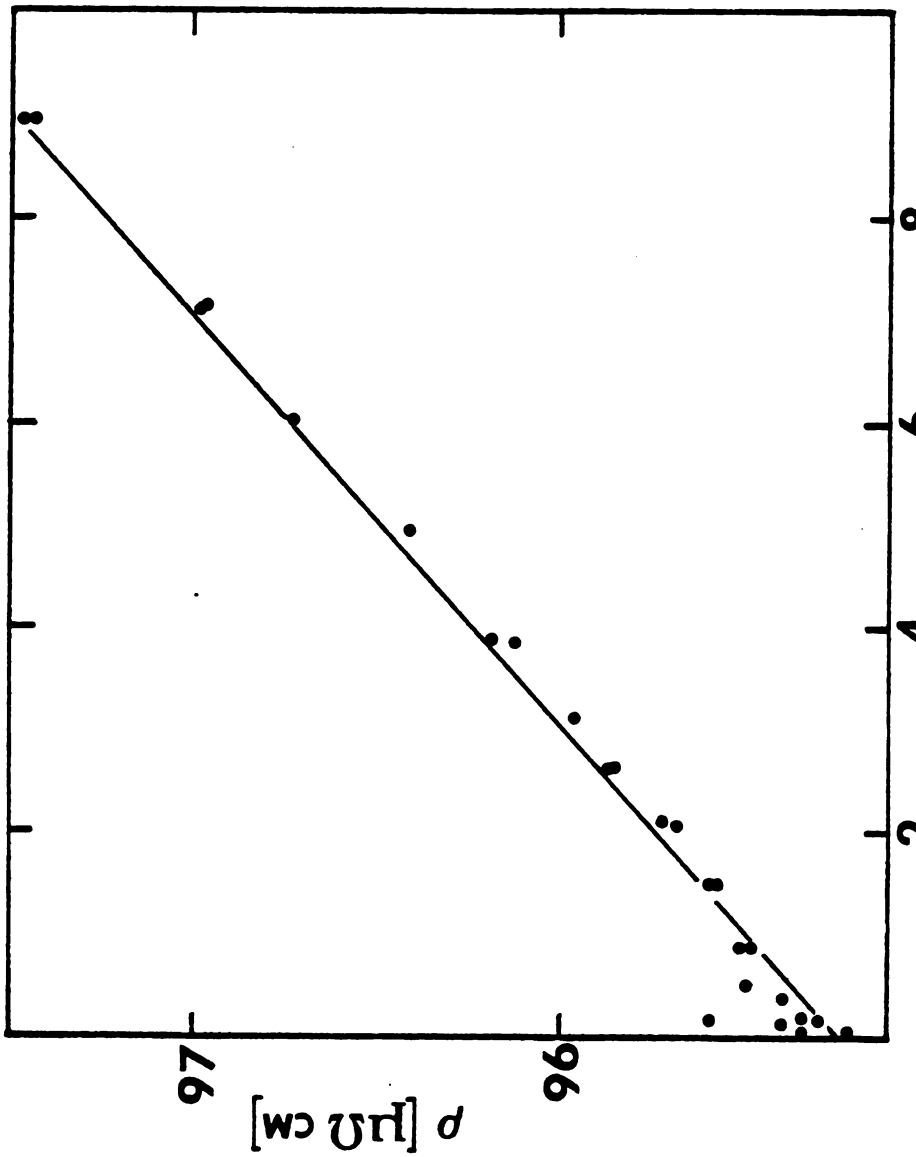

Figure 8.13 ρ(T) vs. T^3 for TS-41 B6 at low T

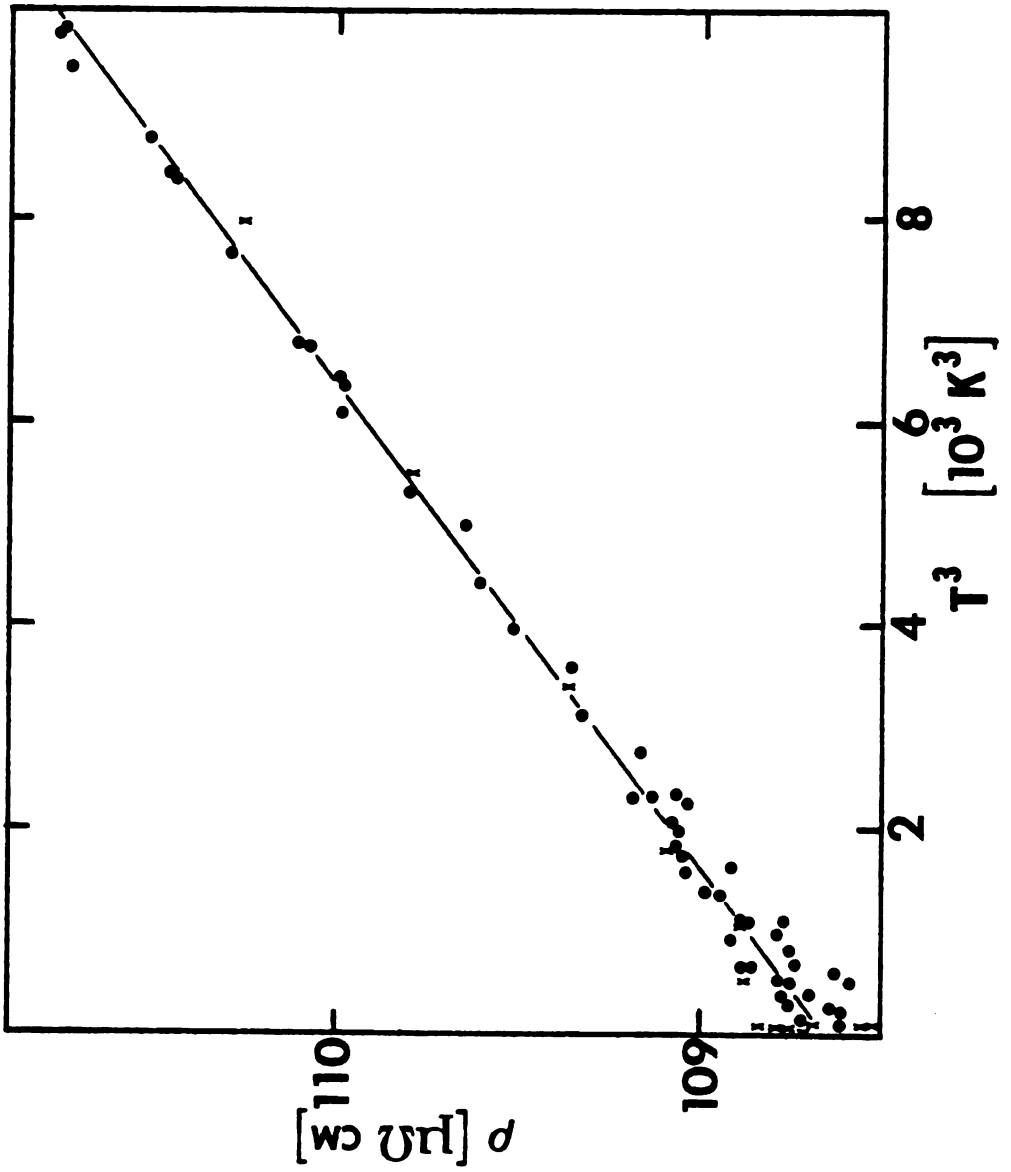

Figure 8.14 ρ(T) vs. T^3 for TS-12 B3 at low T

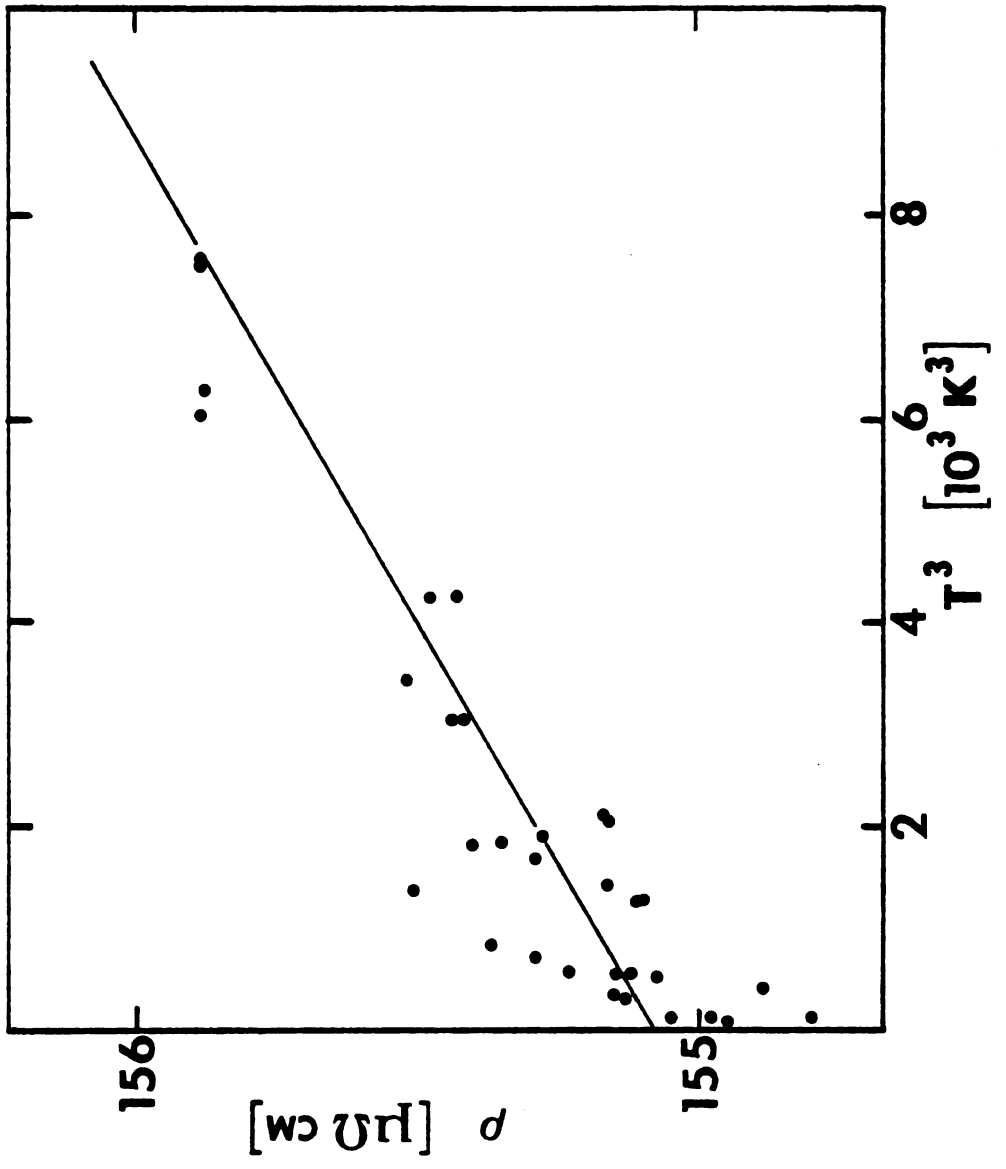

Figure 8.15 ρ(T) vs. T^3 for TS-40 B1 at low T

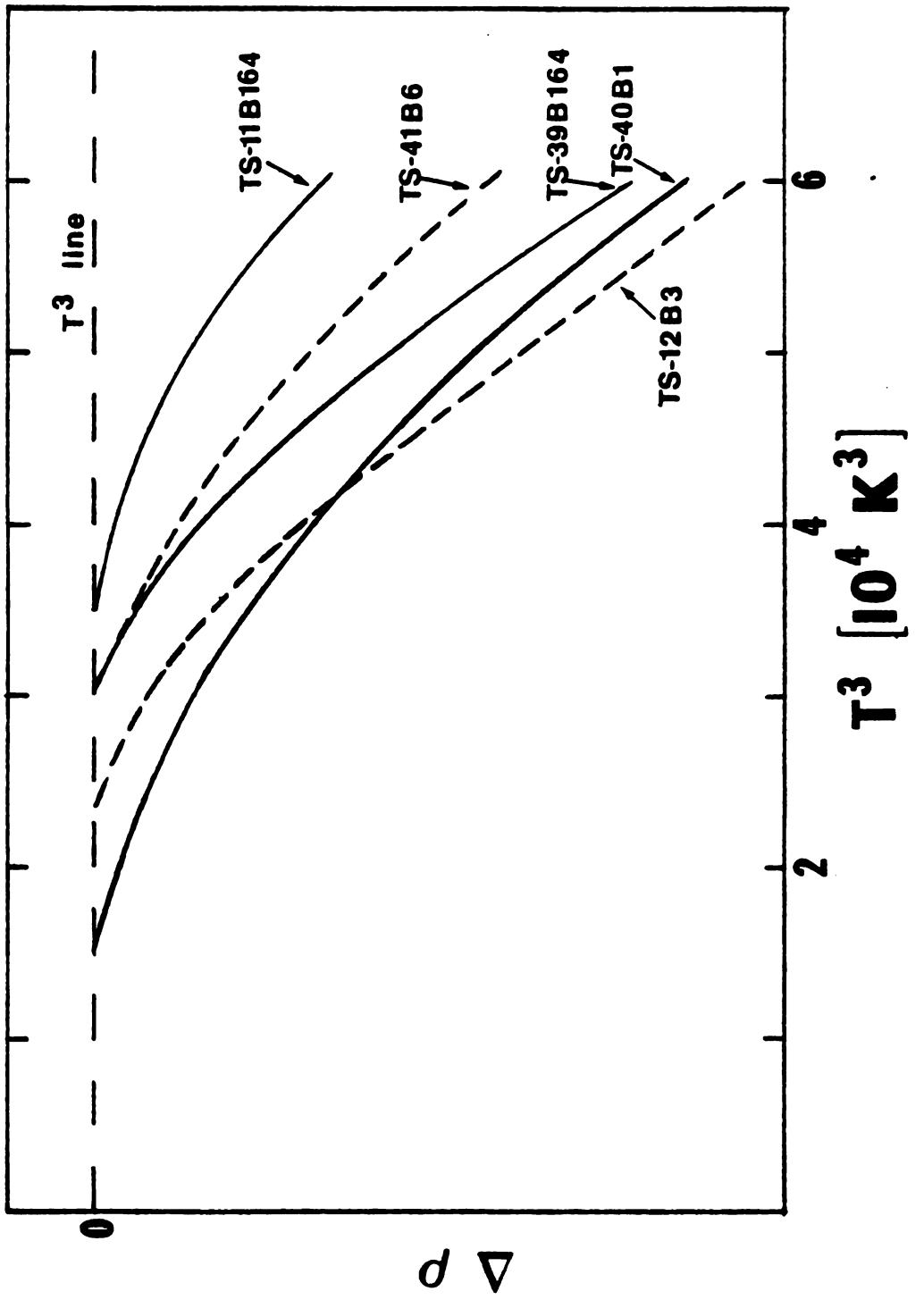

Figure 8.16 Departure from T^3 behavior

Table 8.2 Range of T^3 Behavior

Sample	$\underline{T}$ (K)
TS-11 B164	32.7
TS-39 B164	31.2
TS-41 B6	31.2
TS-12 B3	27.8
TS-40 B1	24.7

It should be noted that the scatter in the resistivity data of Figures 8.6-8.15 is not representative of the precision of these measurements. This scatter appears to be the result of small shifts in the measured residual resistivity ρ_0 that occur over the duration of an experimental run. As discussed in more detail in Appendix D, this problem is most likely an experimental artifact associated with the electrical contacts. The existence of this problem should forewarn any future experimentalists, that its solution must be found before any use can be made of either an increase in temperature capability below 1.5 K or an increase in measurement precision (estimated to be $\lesssim$0.02% in this study--Appendix D).

8.2 Hall Coefficient R_H

From Equation (7.2) the change in the voltage ΔV measured between contacts 2 and 4 for a constant current I flowing through contacts 1 and 3 depends linearly on the magnetic field strength.

$$\Delta V = \frac{R_H I}{d} B \qquad (8.1)$$

Our measurements indicate that the linearity expressed by Equation (8.1) was obeyed to a high degree for samples TS-39 B164 and TS-40 B1 as can be seen from Figure 8.17 where representative data for ΔV taken near $T \simeq 5$ K is plotted against B. For sample TS-41 B6 significant departures from linearity consistently occurred at fields greater than ~15 kG. From our programmed fits using Equation (8.1) to data such as shown in Figure 8.17 we have obtained values of the Hall coefficient R_H over the temperature range of ~4 to ~80 K. However, it is more enlightening to express these results in terms of the carrier concentration n which is given by

$$n = \frac{1}{(R_H e)} \qquad (8.2)$$

using a single carrier model.

The results of our Hall effect measurements are shown in Figure 8.18 where the concentration n of these negatively charged carriers in $Ti_{1+x}S_2$ is plotted against temperature over the temperature range of 4 to 80 K. Our results showing that the carrier concentration increases slightly as the temperature decreases in this regime are consistent with the higher temperature results of Kukkonen et al.[40] who found n to behave in a similar manner over the temperature range of 77 to 300 K. A fit to our data of the form

$$n = n_o - CT \qquad (8.3)$$

produced the values of the coefficients n_o and C listed in Figure 8.18. As can be seen, n increases the fastest for TS-41 B6 at a rate of 0.11%/K while n increases the slowest for TS-40 B1 at a rate of 0.038%/K.

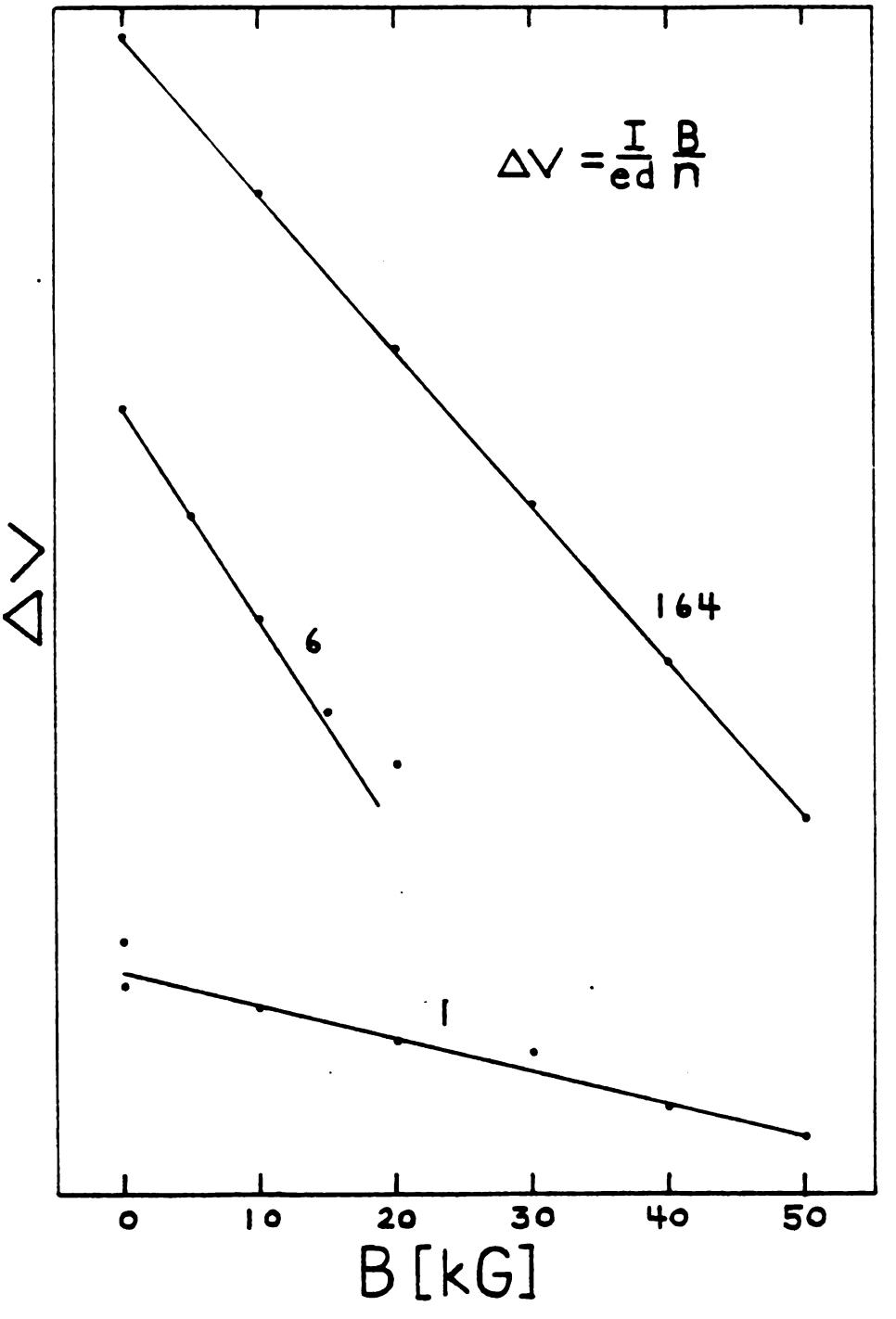

Figure 8.17 Hall voltage vs. B

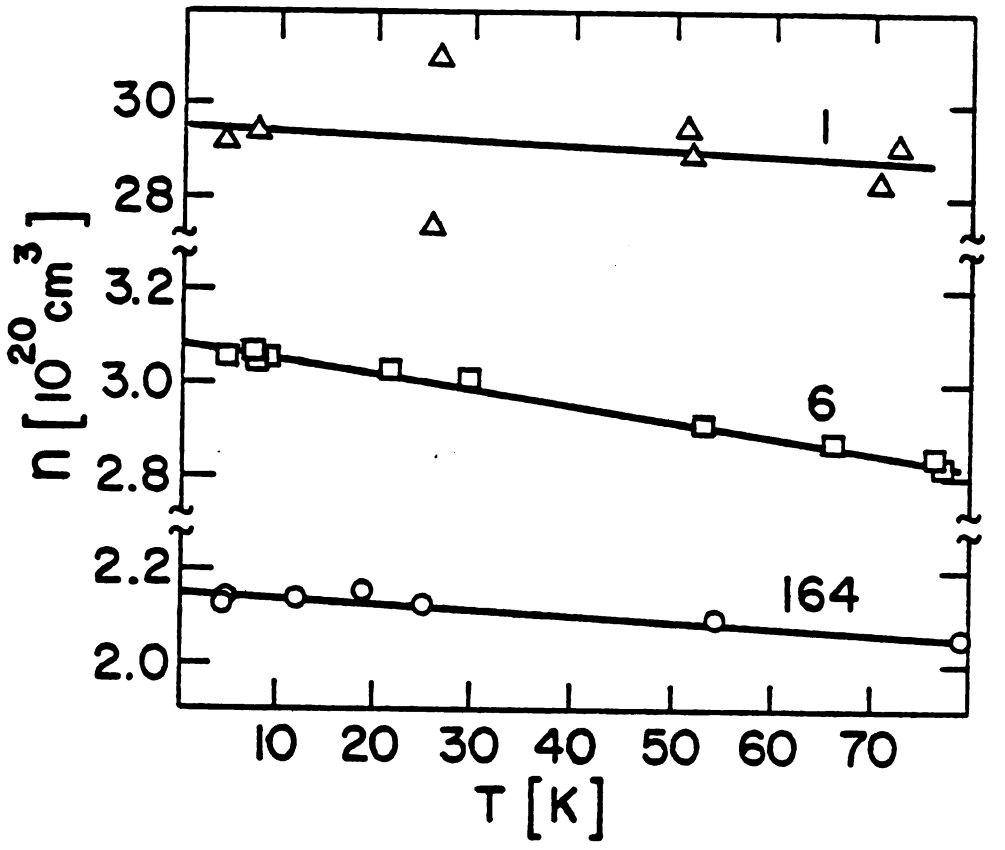

Batch	n_o [10^{20} cm^{-3}]	C [10^{18} cm^{-3} K^{-1}]
164	2.16	.133
6	3.09	.336
1	29.5	1.12

Figure 8.18 n vs. T

8.3 Magnetoresistivity $\rho(B)$

Magnetoresistance measurements were made over the temperature range of 4 to 80 K for samples TS-39 B164, TS-11 B164, TS-41 B6, and TS-40 B1 in magnetic fields up to 50 kG. These results are shown in Appendix G in complete detail, however, a summary of the data is presented in Figure 8.19. Plotted against the field strength are our results for the magnetoresistivity near 5 K, represented by the symbols and solid lines. This effect is relatively small--for sample TS-41 B6 the magnetoresistance amounts to only 3.8% at 50 kG while it amounts to less then 0.5% for the other samples taken from batches #1 and #164. The magnetoresistance is also largely independent of temperature as can be seen from the dotted lines in Figure 8.19 representing the data taken near 80 K.

These results for the magnetoresistivity are somewhat similar to that found in highly doped semiconductor systems which exhibit metal insulator transitions.[42] In those systems, the experimentally observed magnetoresistance is generally negative at low fields, passes through a minimum and becomes positive at higher fields. This behavior is tentatively explained using the idea of two competing mechanisms--a negative contributing mechanism which saturates in higher fields competing with a positive contributing mechanism which dominates in higher fields. This comparison should not be heavily stressed because our magnetoresistivity results for $Ti_{1+x}S_2$ are somewhat limited and are quite tentative in view of the apparent difference in the magnetic field response of samples TS-39 B164 and TS-11 B164 taken from the same batch but with their electrical leads attached to their sides and top surface respectively. This suggests that some of the observed magnetoresistivity may be an experimental artifact associated with the placement of the contacts.

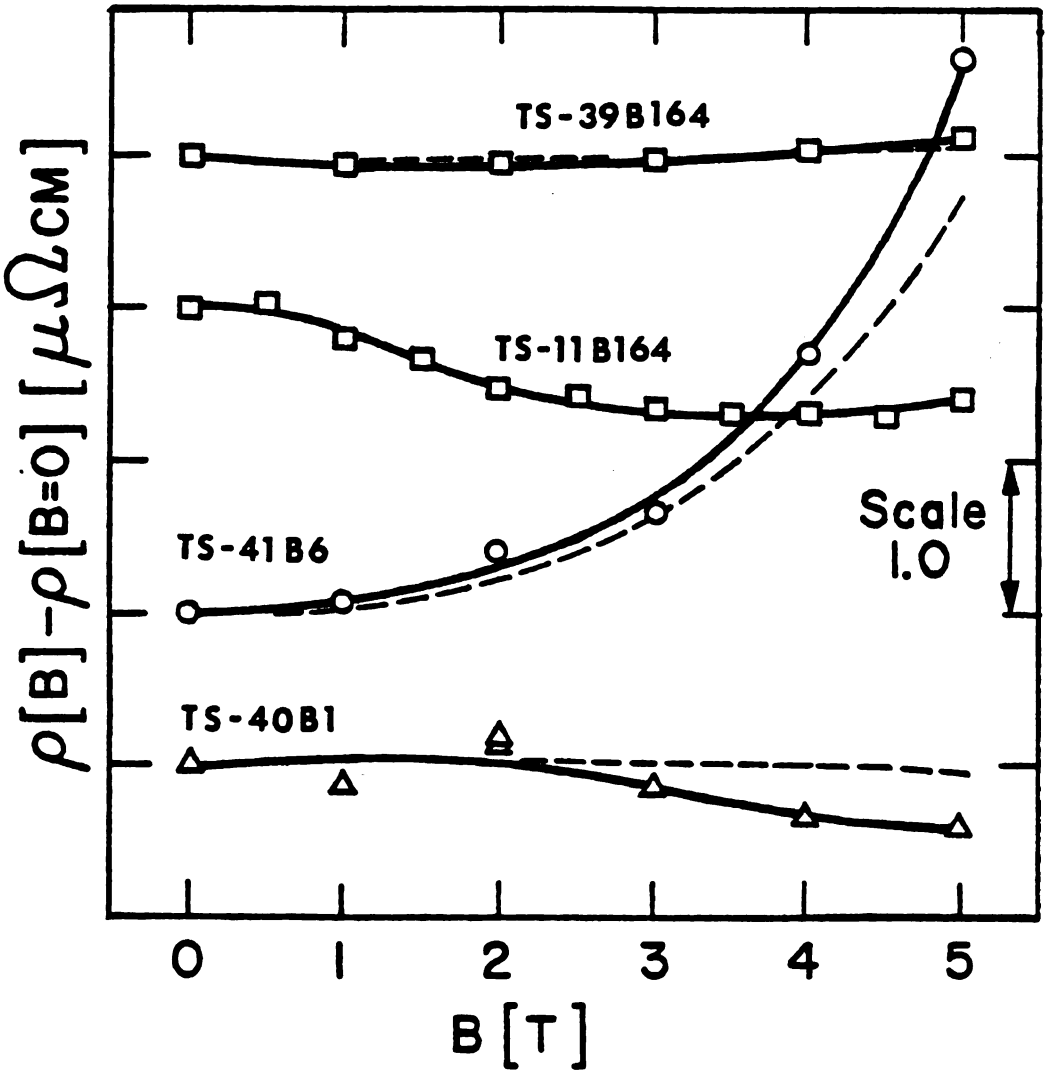

Figure 8.19 $\rho(B)$ of $Ti_{1+x}S_2$

8.4 Scattering Mechanism(s)

Because the carrier concentration is relatively independent of temperature, the unusual temperature dependence of the electrical resistivity must be due primarily to the temperature dependence of the scattering mechanism(s) operating in $Ti_{1+x}S_2$. To try to identify these scattering mechanism(s), it is useful to examine the mobility of the carriers as a function of the carrier concentration at a fixed temperature. Using a single carrier model, the mobility μ is related to the electrical conductivity σ by

$$\sigma = \frac{ne^2\tau}{m} = ne\mu \tag{8.4}$$

where τ is the relaxation time. The mobility, calculable from our resistivity and Hall effect data using

$$\mu = R_H/\rho \tag{8.5}$$

is more reliable then either the Hall coefficient or resistivity data alone when comparing measurements made on different samples. Unlike R_H and ρ which are both linearly dependent on d, μ is independent of the sample thickness.

Using Matthiessen's rule, the mobility can be written in terms of two partial mobilities:

$$\frac{1}{\mu(T)} = \frac{1}{\mu(4.2\ K)} + \frac{1}{\mu'(T)} \tag{8.6}$$

where the residual mobility (taken at 4.2 K) is given by

$$\mu(4.2\ K) = \frac{R_H}{\rho(4.2\ K)} \tag{8.7}$$

and the temperature dependent partial mobility is given by

$$\mu'(T) = \frac{R_H}{(\rho(T) - \rho(4.2\ K))} \tag{8.8}$$

Our results are presented in Figure 8.20 where the logarithm of the residual mobility is plotted against the logarithm of the carrier concentration. Also shown are the high temperature results for $\mu'(T)$ of Kukkonen et al.[40] Our data for $\mu(4.2\ K)$, which arises from temperature independent "impurity" scattering, appears to vary as $n^{-4/3}$ at carrier concentrations above $\sim 10^{21}$ cm^{-3}. This $n^{-4/3}$ dependence can be understood by noting that the scattering rate due to impurities is given by

$$\frac{1}{\tau_{imp}} \propto N_{imp} \langle M^2 \rangle D(\varepsilon_f) \tag{8.9}$$

where N_{imp} is the density of impurities, M is the scattering matrix element whose square gets suitably "averaged" over $\vec{k}$ space, and $D(\varepsilon_f)$ is the density of final states. The experimentally observed relationship of $\mu = e\tau/m \propto n^{-4/3}$ is obtained if M is independent of n (which occurs for impurity scattering), $D(\varepsilon_f)$ is given by the free electron relation $D(\varepsilon_f) \propto n^{1/3}$, and if the scattering impurities are also the source of the carriers ($N_{imp} \propto n$). This latter condition is met in the $T_{i+x}S_2$ system where, at least for the more stoichiometric samples, the source of the carriers is generally thought to be the excess Ti atoms, with each atom contributing its four valence electrons to conduction. In contrast, the results at "finite" temperatures are not as well understood.

The room temperature results of Kukkonen et al. which showed a $n^{-0.27}$ dependence for $\mu'(T)$ is characteristic of electron phonon scattering in nondegenerate semiconductors where $\mu'(T) \propto n^{-1/3}$ but, as they

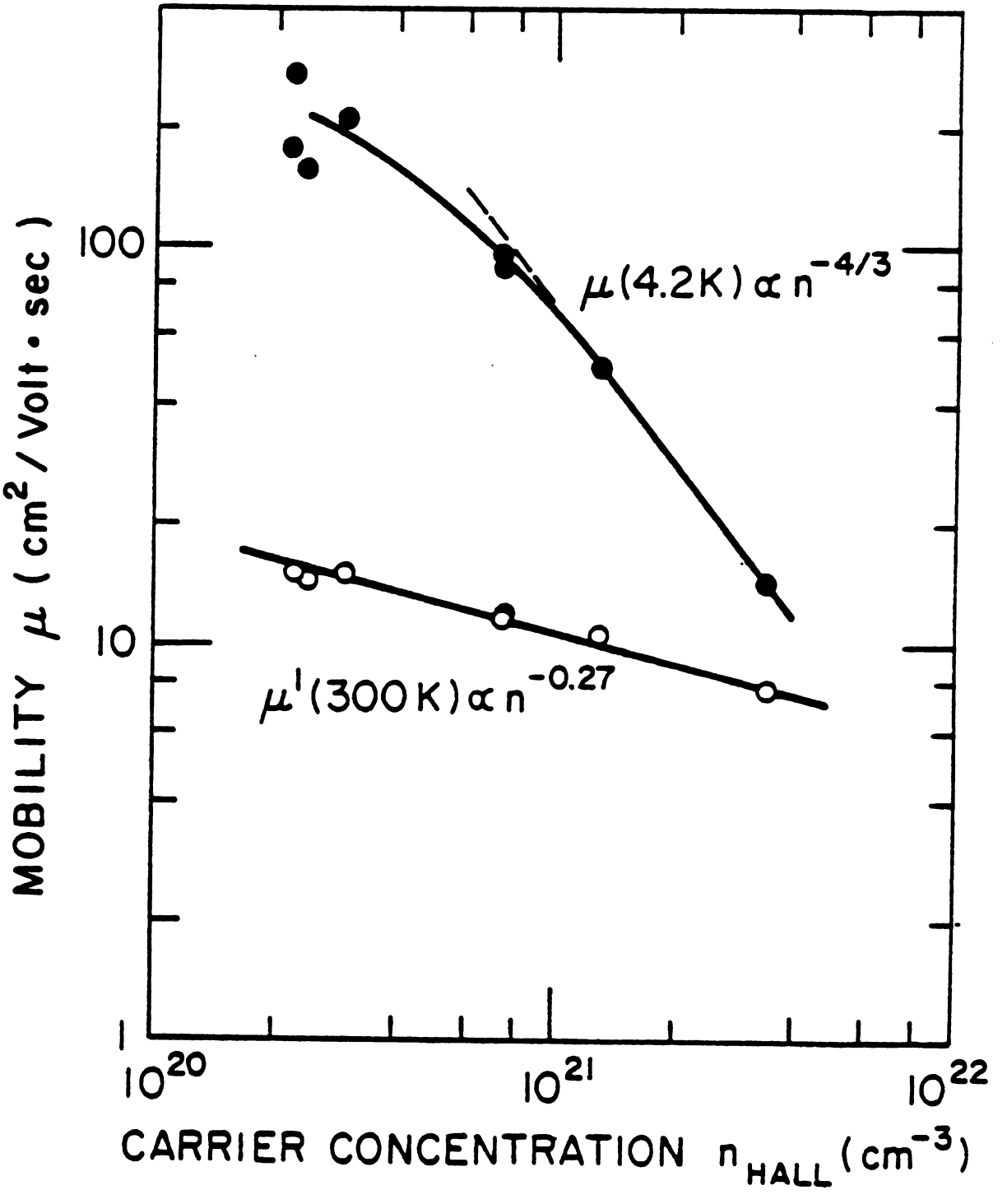

Figure 8.20 μ(4.2 K) and μ'(300 K) vs. n

point out, electron phonon scattering is not consistent with the temperature dependence of the electrical resistivity. Simple acoustic phonon scattering predicts a linear dependence on temperature above about $\theta_D/3$, where the Debye temperature θ_D for TiS_2 is 235 K, and it predicts a T^5 dependence at low temperatures. Electron phonon scattering is also inconsistent with our results for the carrier concentration dependence of $\mu'(T)$ in the T^3 resistance regime. Our results of $\mu'(T)$ are shown in Figure 8.21 where the logarithm of $\mu'(T)$ (arbitrarily calculated at 20 K) is plotted against the logarithm of n, which shows that instead of depending on n as $n^{-1/3}$, $\mu'(T)$ depends as $n^{-0.54}$--a dependence that we can not explain with any mechanism.

As of the present, no one has come up with a satisfactory explanation of the nominal T^2 temperature dependence seen in the electrical resistivity of $Ti_{1+x}S_2$ at high temperatures, nor have we found an explanation for the new T^3 behavior at low temperatures that we have observed.

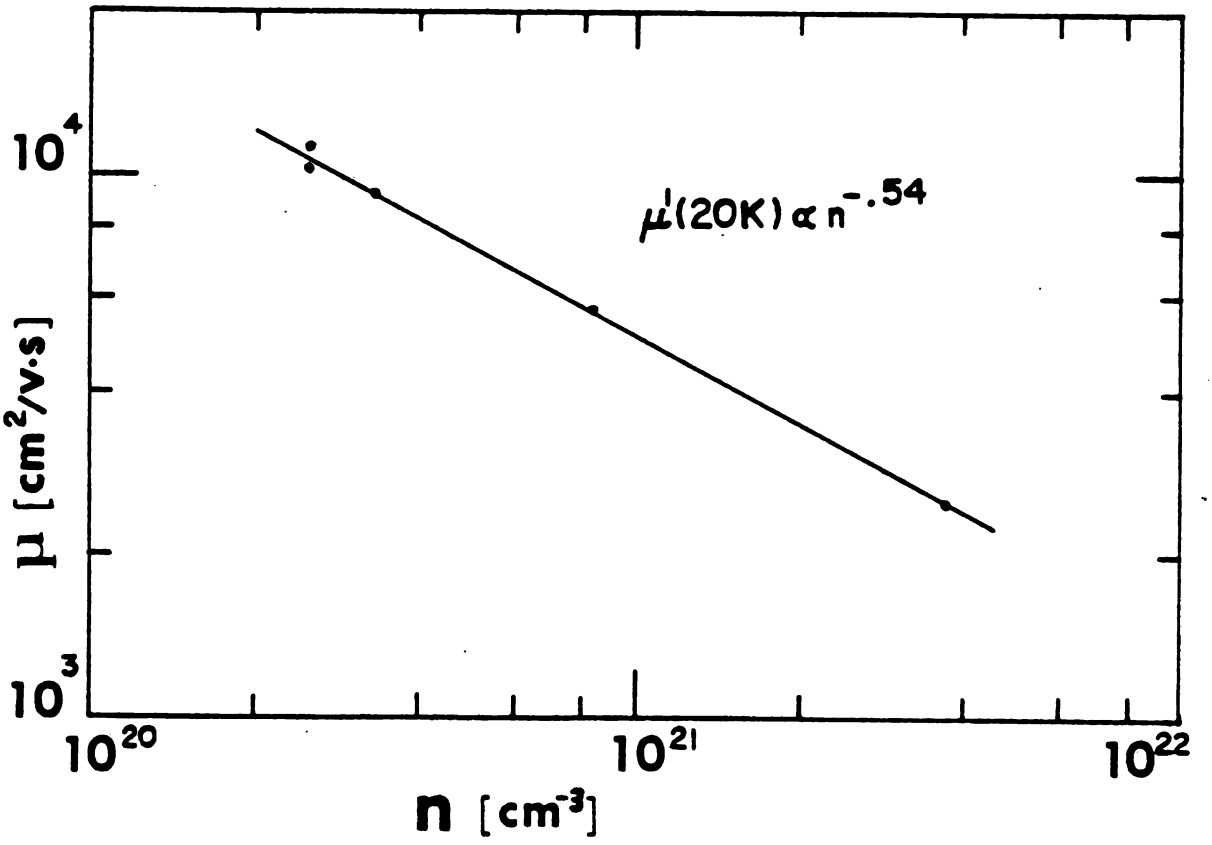

Figure 8.21 μ'(20 K) vs. n

APPENDICES

APPENDIX A

TENSORS IN A MAGNETIC FIELD

In this appendix it will be shown that if the applied magnetic field is along a 3-, 4-, or 6-fold symmetry axis of the system, then each of the transport tensors in Equation (2.1) has the form

$$\begin{bmatrix} \Sigma_{xx} & \Sigma_{xy} & 0 \\ -\Sigma_{xy} & \Sigma_{xx} & 0 \\ 0 & 0 & \Sigma_{zz} \end{bmatrix}$$

where the z-axis is along the field direction.

Consider a crystal in a magnetic field applied along a symmetry direction, the z-axis. The other Cartesian directions (x and y) are arbitrary. Now consider a new coordinate system {x',y',z'} that is related to the original system {x,y,z} by a rotation through an angle θ about the z-axis. Using the transformation matrix

$$\overleftrightarrow{T} = \begin{bmatrix} \cos\theta & \sin\theta & 0 \\ -\sin\theta & \cos\theta & 0 \\ 0 & 0 & 1 \end{bmatrix} \tag{A.1}$$

any vector $\vec{b}$ in {x,y,z} becomes $\vec{b}'$ in {x',y',z'} where $\vec{b}' = \overleftrightarrow{T}\, b$. Similarly for a second rank tensor $\overleftrightarrow{\Sigma}$

$$\overleftrightarrow{\Sigma}' = \overleftrightarrow{T}\,\overleftrightarrow{\Sigma}\,\overleftrightarrow{T}^{-1} \tag{A.2}$$

If the amount of rotation θ corresponds to a symmetry operation of the crystal, then each of the components of the physically relevant tensor in the new coordinate system must be equal to its counterpart in the old system. That is,

$$\Sigma'_{ij} = \Sigma_{ij} \tag{A.3}$$

for each i and j. By performing the indicated algebra of Equations (A.1-A.3) it is easily shown that for any physically relevant second rank tensor $\overleftrightarrow{\Sigma}$,

$$\overleftrightarrow{\Sigma} = \begin{bmatrix} \Sigma_{xx} & \Sigma_{xy} & 0 \\ \Sigma_{yx} & \Sigma_{yy} & 0 \\ 0 & 0 & \Sigma_{zz} \end{bmatrix}$$

if the applied magnetic field is along a 2-fold symmetry direction; and that if the field is along a 3-, 4-, or 6-fold symmetry direction then

$$\overleftrightarrow{\Sigma} = \begin{bmatrix} \Sigma_{xx} & \Sigma_{xy} & 0 \\ -\Sigma_{xy} & \Sigma_{xx} & 0 \\ 0 & 0 & \Sigma_{zz} \end{bmatrix} .$$

APPENDIX B

SAMPLE ALIGNMENT

The samples investigated in this thesis were aligned relative to the magnetic field of a superconducting solenoid using an optical technique. Basically the method consists of shining a laser beam onto a microscope cover slide which is attached to a planar surface and using the reflected beam as a reference to the normal of the surface. In this way, planar faces can be adjusted to be parallel to a very high degree.

We will now outline the specific steps that were followed in aligning samples in the particular cryostat used in these experiments, however, the principles behind these steps are more general and may be applied to other systems.

1. The cryostat was inserted into the magnet support structure and "jammed" into the bore of the solenoid in the same position that it would occupy during an experimental run.

2. The cryostat was securely fastened to the support structure in such a way as to allow the magnet and the cryostat's vacuum can to be removed without changing the cryostat's position.

3. A small piece of a microscope cover slide was "attached" to the bottom planar face of the solenoid using a small drop of water. A laser beam was then shown onto this cover slide and the position of the reflected beam was recorded.

4. The magnet and the vacuum can were then removed to expose the inner workings of the cryostat.

5. A piece of cover slide was "attached" to the sample's planar face and the sample soldered into the cryostat while making sure that its reflection was in the same position as that recorded in step #3. (Between steps 4 and 5 the laser was moved vertically using a lab jack. Checks must be made to insure that the laser beam moves parallel to itself over this displacement.)

6. The can was carefully replaced and the reflection off its bottom face was also recorded. (This position is not related to that in step #3.)

7. The magnet was put back in place while monitoring the can's reflection (step #6) to insure that its position remained unchanged, which meant that the sample's reflection was also unchanged.

8. Finally, after the magnet was firmly attached, its reflection was rechecked with its old position recorded in step #3.

With some practice and some care, the differences between all the recorded positions could be made less than 1/10°. We have claimed that our alignments with respect to the magnetic field direction were within ¼°. The main uncertainties lie in the assumptions that the field of the solenoid is perpendicular to its bottom face and that the cryostat's position inside the solenoid is reproducible after each time the cryostat is removed from the dewar.

APPENDIX C

CHOPPERS WITH FEEDBACK

Electronics	(see Figure 4.5 for a circuit schematic)
R_T, R_f	Brass standard resistors with nominal resistances of 80×10^{-6} Ω at 4.2 K.
R_F	Room temperature resistor (~9.9×10^3 Ω)
Modulator	~1 inch of bare NbTi wire. ~1 foot of Evanohm wire (418 Ω/ft); doubled before winding around the NbTi in a monolayer. This assembly was inserted into a piece of glass capillary tubing filled with Apiezon grease.
T_1	4.2 K transformer consists of two identical transformers wound oppositely to reduce pick-up. Cores: Teflon, Length 0.225 in., Diameter 0.25 in. Primary: 3 mil NbTi, 40 turns, monolayer. Secondary: AWG 46 copper wire, 2,000 turns.
T_2	Room temperature transformer
Amplifier	Low-Noise Amplifier; Princeton Applied Research Model CR4-A
PSD	Phase Sensitive Detector; Princeton Applied Research Model 124A with Model 116 Differential Preamplifer
Oscillator	Krohn-Hite Model 4100
Frequency Doubler	Frequency doubler consists of a resistor and a diode in series. Lock-in detects the first harmonic in the voltage drop across the diode.

Isolation Amplifier	Isolation amplifier built in-house by Electronics Shop, MSU Physics Department.
Filter	Krohn-Hite Model 3750

Chopper Circuit Analysis

A straightforward analysis of the chopper circuit diagram reveals that the ratio of the feedback current I_F to a test signal current I_T is

$$\frac{I_F}{I_T} = \frac{R_T[A - R_f/R_{sum}]}{[AR_f + R_F - R_f^2/R_{sum} + R_f]} \qquad (C.1)$$

where R_{sum} is the summation of all the resistances in the low temperature network including an effective input impendance R_{in} of the amplifying network. That is $R_{sum} = R_T + R_f + R_{s(sample)} + R_{in}$. The open loop gain of the system A is defined as the output of the system $V^o_{R_F} = R_F I^o_F$ (with the feedback current disconnected from the low temperature feedback resistor R_f) divided by an input signal $V^o_T = R_T I^o_T$. That is $A = V^o_{R_F}/V^o_T$. With the switch in the feedback circuit, A can be experimentally determined if desired. Typically the system was operated with a value of $A \approx 3\times10^{10}$. Because $R_f/R_{sum} \lesssim 1$ and $R_f << R_F$ then Equation (C.1) becomes

$$\frac{I_F}{I_T} = \frac{R_T A}{[AR_f + R_F]} \qquad (C.2)$$

The effective gain A_F of the system with feedback, given by $A_F = V_{R_F}/V_T = R_F I_F/R_T I_T$ is then

$$A_F = \frac{R_F}{R_f}\left[1 + \frac{R_F}{R_f}\frac{1}{A}\right]^{-1} \qquad (C.3)$$

(This result is given in the paper by Fletcher and Stinson.[16]) In our system if $A \simeq 10^{10}$ then $R_F/AR_f \simeq 0.012$, so

$$A_F \simeq \frac{R_F}{R_f} \tag{C.4}$$

to within 1.2%. The fact that Equation (C.4) is not valid to a high precision is not important since A_F is experimentally determined. The real benefit of using feedback is in the stability of the system's gain. From Equation (C.3) it can be seen that any change in the open loop gain of the system corresponds to a much smaller change in the feedback gain. For example, a 10% change in A (for $A \simeq 10^{10}$) corresponds roughly to a 0.12% change in A_F. Thus the gain of the chopper with feedback is much more resistant to changes in time and/or magnetic fields than is the basic chopper.

According to Fletcher and Stinson, another benefit of feedback is that the input impedance of the chopper system increases by the factor A/A_F. This result can be deduced by considering the change in the gain due to a small change δR_s in the sample resistance. From Equation (C.3) the change in the feedback gain of the system would be

$$\delta A_F = \frac{R_F}{R_f}\left(1 + \frac{R_F}{R_f}\frac{1}{A}\right)^{-2}\left(\frac{R_F}{R_f}\frac{1}{A^2}\,\delta A\right)$$

$$\simeq \left(\frac{R_F}{R_f}\right)^2 \frac{1}{A^2}\,\delta A$$

or

$$\delta A_F \simeq \left(\frac{A_F}{A}\right)^2 \delta A \tag{C.5}$$

where δA is the change in the gain of the system with no feedback. The percentage change in the gain of the feedback system is then given by

$$\frac{\delta A_F}{A_F} \approx \left(\frac{A_F}{A}\right) \frac{\delta A}{A} \tag{C.6}$$

which is related to the input impedance R_{in} of the chopper by

$$\frac{1}{A_{(F)}} \frac{\delta A_{(F)}}{\delta R_S} \approx (R_T + R_f + R_S + R_{in}^{(F)})^{-1} \tag{C.7}$$

Provided the resistances in the low temperature chopper circuit are much less than the input impedance of the chopper, i.e. $R_T + R_f + R_S \ll R_{in}$, then equations (C.6) and (C.7) imply that

$$R_{in}^F \approx \left(\frac{A}{A_F}\right) R_{in} \tag{C.8}$$

Thus the input impedance of the chopper using feedback is roughly increased by the factor $A/A_F \sim 100$. Several tests were conducted on the chopper system used in this study to ensure that the system was operating correctly.

With values of A between 1×10^8 and 1.6×10^{10}, Equation (C.3) was obeyed to within 1%. In the Fletcher-Stinson system, the agreement was within their experimental error ($\lesssim$0.2%). Presumably our results would have been similar had more effort been exerted to improve the uncertainty level.

Checks on the system's gain were made during the course of the thermopower experiments. It was found that the gain was independent of time and magnetic field strengths to within experimental uncertainty of $\lesssim$0.3% over times of ~6 hours and magnetic fields up to 50 kG.

Finally, measurements of the system's gain, with and without feedback, were conducted as a function of the sample resistance. Shown in Figure C.1, plotted as a function of the sample resistance R_S, are our results for the percentage change in the gain of the system $\Delta A/A$. (That is $\Delta A = A(R_S) - A(R_S = 0)$.) As can be seen, the magnitude of the changes $\Delta A/A$ produced by increasing R_S, were reduced using feedback by the factor ~0.011 which compares favorably with the experimental values of A_F/A ranging from ~0.005 to 0.013. (See Equation (C.6).) Using Equation (C.7) we estimated the values of the system's input impedances, with and without feedback, to be 0.1 Ω and 0.001 Ω respectively.

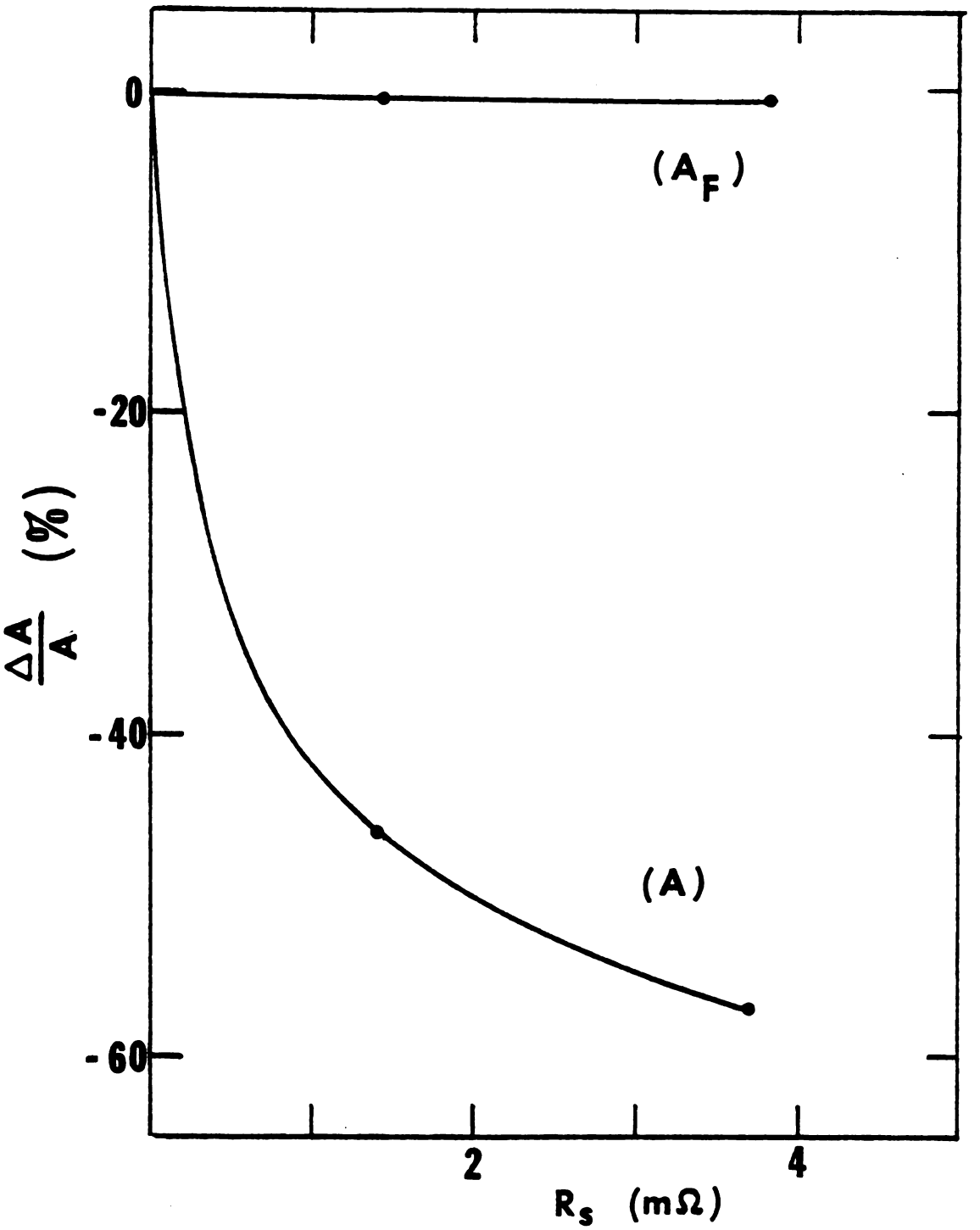

Figure C1 Chopper loading

APPENDIX D

MEASUREMENT PROBE MISALIGNMENT

Consider a perfectly aligned crystal, i.e. one for which its potential probes 1,2,3,4 (see Figure D 1a) form a coordinate system with one axis aligned along the heat current $\vec{U}$ direction. The heat current is assumed to be uniform. The thermopower is defined as $S^a = E_x/\frac{\partial T}{\partial x}$ and the Nernst-Ettinghausen coefficient is defined as $Q^a = -E_y/\frac{\partial T}{\partial x}$. These are experimentally determined by measuring the voltage differences generated by the heat current between the probes. The voltage differences are given by

$$V_2 - V_1 = -\int_1^2 E_x dx \tag{D.1}$$

and

$$V_4 - V_3 = -\int_3^4 E_y dy \tag{D.2}$$

Assuming linear response (i.e. operationally small temperature differences) the potential differences can be written as

$$V_2 - V_1 = -\int_1^2 S^a \frac{\partial T}{\partial x} dx$$

$$\simeq -S^a(T_{av})(T_2 - T_1) \tag{D.3}$$

and

$$V_4 - V_3 = \int_3^4 Q^a \frac{\partial T}{\partial x} dy$$

$$\simeq Q^a(T_{av}) \frac{(T_2 - T_1)}{\ell/w} \qquad (D.4)$$

where T_{av} is defined as $\frac{1}{2}[T_2 - T_1]$. Therefore

$$S^a(T_{av}) \simeq -\frac{(V_2 - V_1)}{(T_2 - T_1)} \qquad (D.5)$$

and

$$Q^a(T_{av}) \simeq \frac{\ell}{w} \frac{(V_4 - V_3)}{(T_2 - T_1)} \qquad (D.6)$$

But suppose probes 1,2 are misaligned with respect to the heat axis by an angle θ as shown in Figure D 1b. Then

$$V_2 - V_1 = -\int_1^a E_x dx - \int_a^b E_y dy - \int_b^2 E_x dx \qquad (D.7)$$

Now $\nabla T = -\overleftrightarrow{\Upsilon}\vec{U}$ where $\overleftrightarrow{\Upsilon}$ is the thermal resistivity tensor which implies that $\frac{\partial T}{\partial y} = -\Upsilon_{yx}U_x$. So $T_b - T_a = \int_a^b \frac{\partial T}{\partial y} dy = -\Upsilon_{yx}(T_{av})U_x \ell \tan\theta$. But $\Upsilon_{yx} << \Upsilon_{xx}$ for Cd and W and if $\tan\theta$ is small then to an excellent approximation $T_b = T_a$. Hence the right hand side of Equation (D.7) becomes $-\int_1^2 E_x dx - \int_a^b E_y dy$. Comparing the first term on the right hand side with Equations (D.1) and (D.3), and the second term with Equations (D.2) and (D.4)

$$V_2 - V_1 = -S^a(T_{av})(T_2 - T_1) + Q^a(T_{av}) \frac{(T_2 - T_1)}{\ell} p$$

where p is the distance between a and b, i.e.

$$V_2 - V_1 = -S^a(T_{av})(T_2 - T_1) + Q^a(T_{av})\ \tan\theta(T_2 - T_1)$$

Experimentally we measure

$$S^m(T_{av}) = -\frac{(V_2 - V_1)}{(T_2 - T_1)} = S^a(T_{av}) - Q^a(T_{av})\tan\theta \qquad (D.8)$$

Therefore

$$S^m(B) = S^a(B) - Q^a(B)\ \tan\theta \qquad (D.9)$$

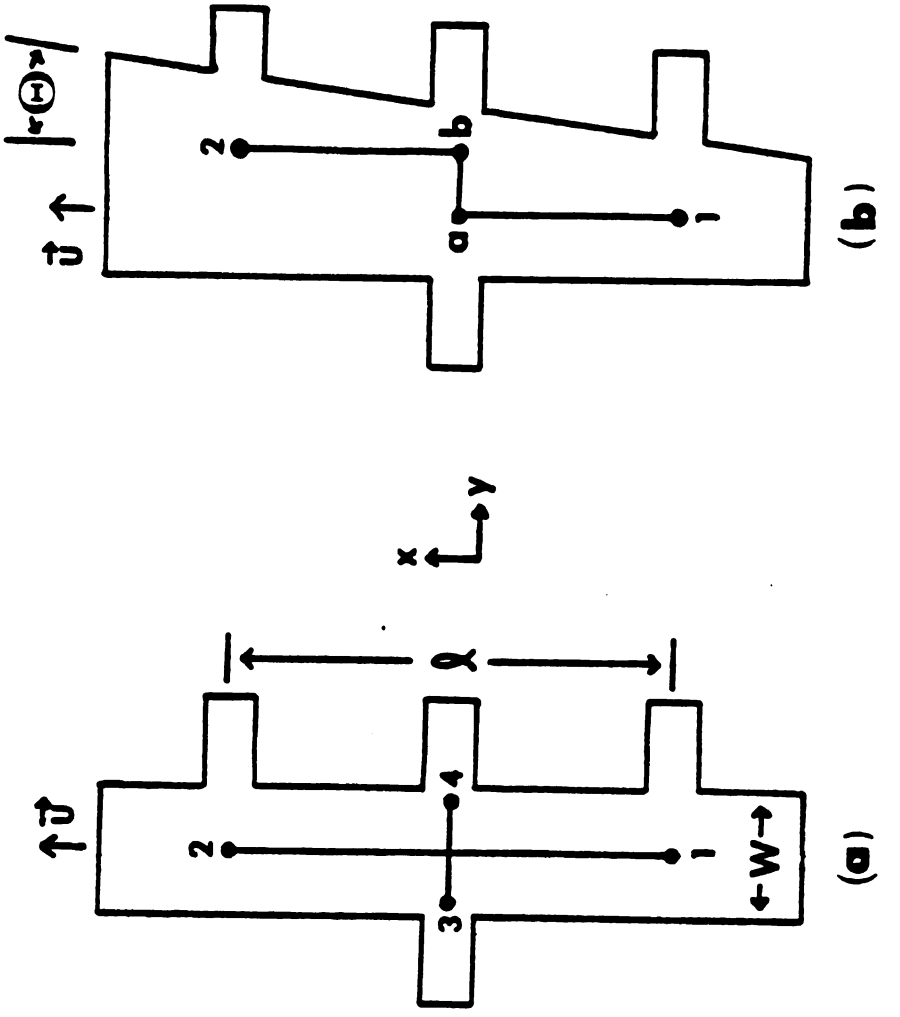

Figure D1 Alignment of measurement probes

APPENDIX E

SCATTER IN $\rho(T)$ DATA

As mentioned in Section 8.1, the scatter in our $\rho(T)$ data for $Ti_{1+x}S_2$ is significantly larger than is our level of precision. The aim of this appendix is to determine the source of this "noise."

During one experimental run for sample TS-12 B3 we took a lot of data in the low temperature range in the hopes of finding some characteristics of this "noise" with which to identify it. Our results, taken over a 24 hour period from 10 a.m. to 10 a.m., are shown in Figures E1 and E2 where plotted against time is a quantity δ, defined as the difference between the measured resistivity and the calculated cubic fit discussed in Section 8.1. That is,

$$\delta = \rho(T) - (\rho_o + aT^3) \qquad (E.1)$$

Also plotted in these graphs are the measured temperatures at which the points were taken. (Straight line segments were drawn connecting these temperature points for clarity and only in a very vague way do they represent dT/d(time).)

There are several mechanisms which readily come to mind that would cause non-zero δ's, however they can not explain the data.

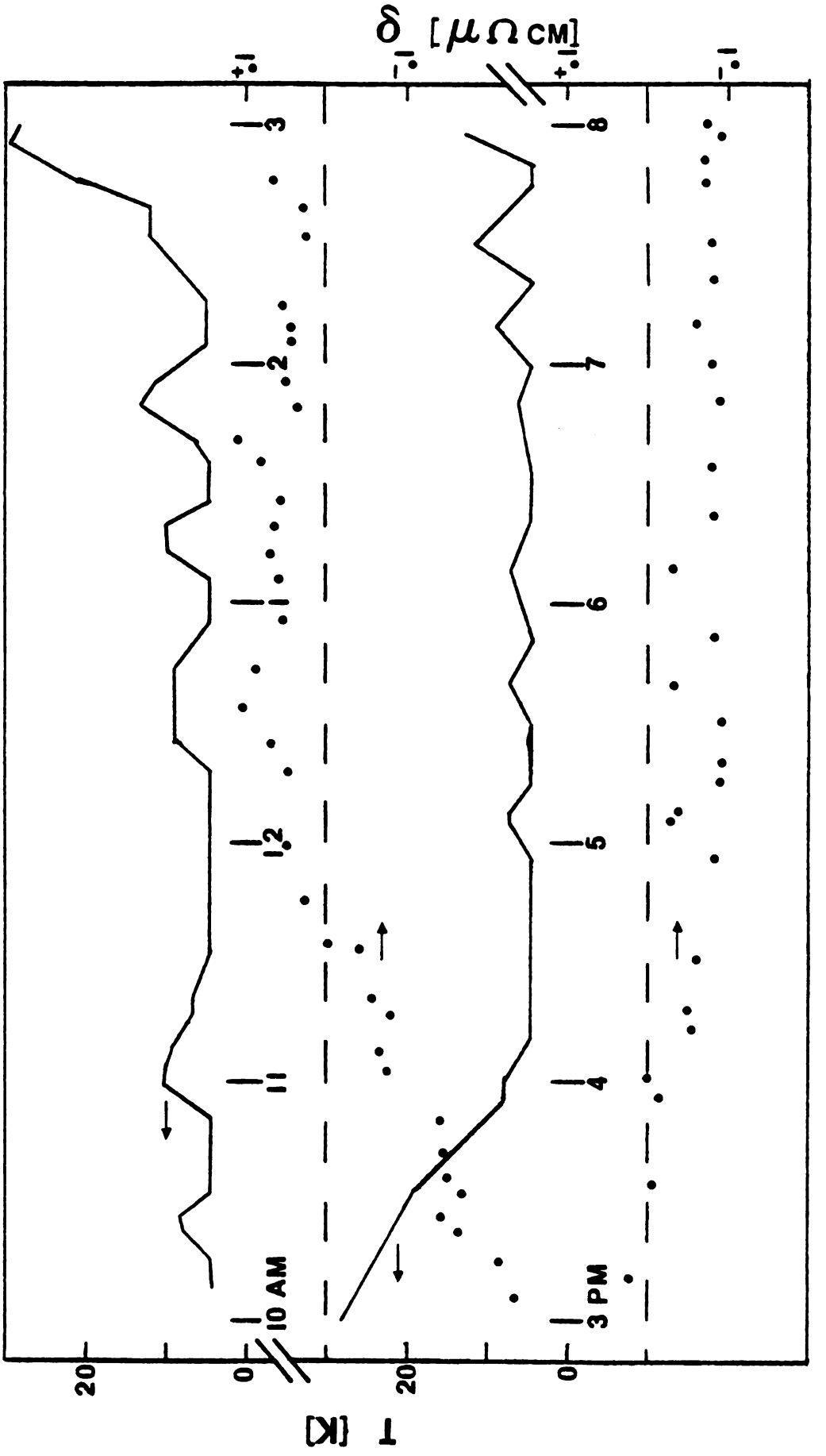

Figure E1 δ vs. time

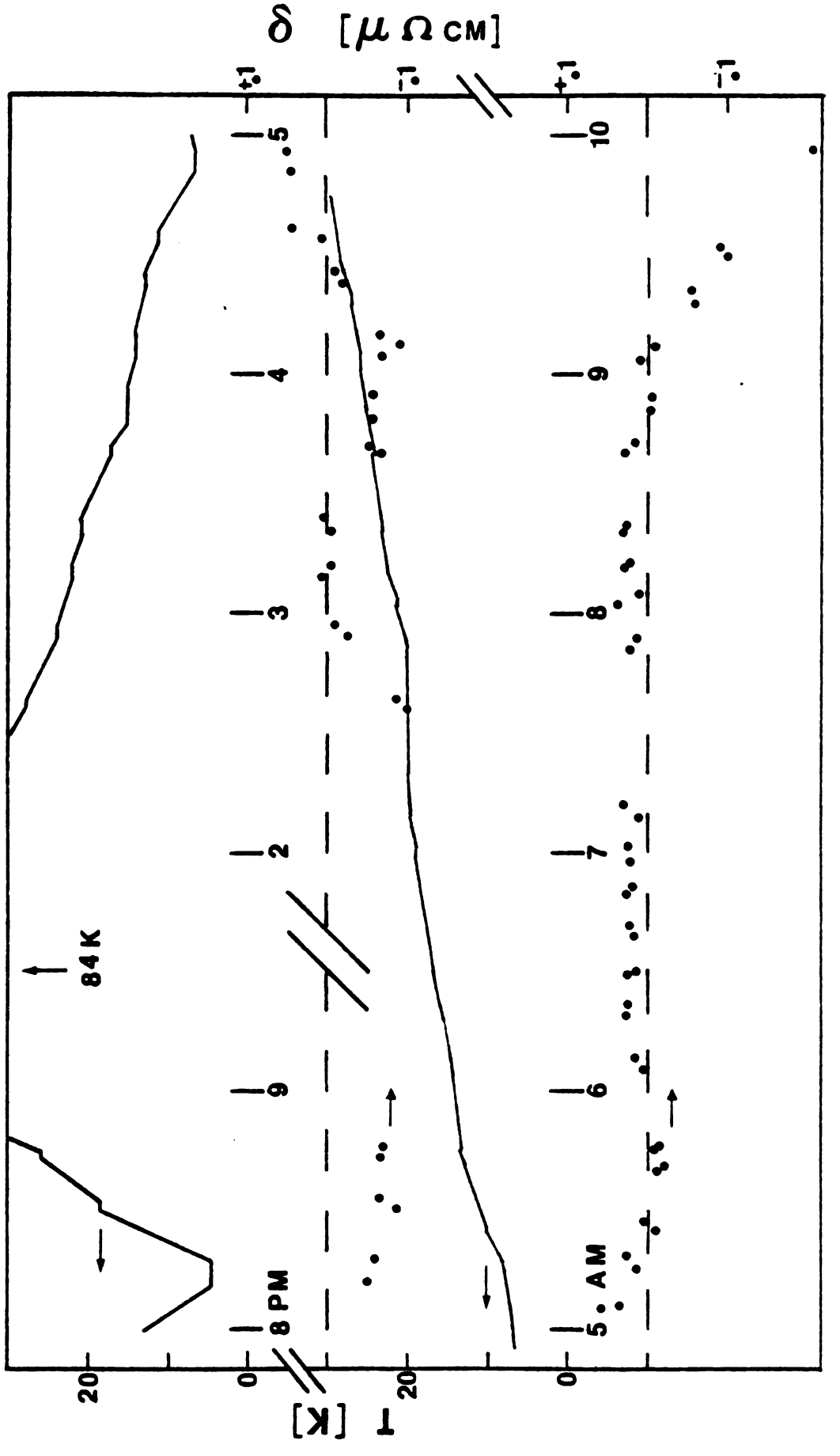

Figure E2 δ vs. time (cont.)

1. Noise

Any noise arising from imprecision of the measurements would result in a completely random scatter of δ about zero. Examining the data for random scatter between data points places a conservative estimate of the noise level at $\delta \lesssim 0.02$ μΩcm (or <0.02%), which is certainly much less than the changes in δ of the order of 0.1 μΩcm (or 1%), so noise can not be the source.

2. Fit Error

Since δ depends critically on the choice of the fit used, there are three sources of error which will contribute to non-zero δ's. They are:

a. If the chosen value of ρ_0 is incorrect then δ would be equal to a constant at all times and temperatures.

b. If the value of "a" is incorrect, δ should systematically increase (decrease) with increasing temperature if "a" is lower (higher) than its correct value.

c. If the functional form is wrong, that is, if the resistivity does not depend on the cube of the temperature but depends in some other way, then again δ should change with temperature in a systematic and consistent way.

Because none of these predictions are consistent with the data, fitting error can be ruled out as the source of the scatter in the δ data.

3. Finite Response Time

A possible source of non-zero δ's could be the failure to wait a sufficient time for the sample to reach an equilibrium temperature after a temperature change has been made before making a measurement. However,

this effect would be much too small. For a δ of 0.05 $\mu\Omega$cm to occur a difference of ~3 K would have to exist between the sample and the germanium resistance thermometer--a ridiculously large amount. Therefore, a finite response time of the system with respect to temperature changes can not be the source.

4. Thermopower

Associated with changes in temperature it is conceivable that the thermopower might contribute to our measurements, although it is hard to imagine given the geometry of the experimental situation how temperature differences could even arise across the sample. However, any generated thermal voltages would have a nearly D.C. frequency component associated with the relatively slow changes of ΔT with time which simply would not contribute to our A.C. measurements of ρ. Therefore, the thermopower can not be the source of non-zero δ's.

Having exhausted the simple experimental artifacts which would cause non-zero δ's, we must think of some other source. From an overall view, ignoring the early data from 10 a.m. to 12 p.m., the δ data appears to assume three (if not more) distinct values of approximately +0.06, 0.0 and -0.08 $\mu\Omega$cm. To see how this manifests itself in the resistivity results, we have replotted our data in Figure E3, where ρ is plotted against T^3 and the data assignable to these three δ values are designated x, o, and Δ respectively with $\bullet$ labeling unassigned data points. Drawn through these groups of data are three parallel straight lines 1, 2 and 3. (Line 2 is the T^3 fit to all the data shown in Figures 8.9 and 8.14).

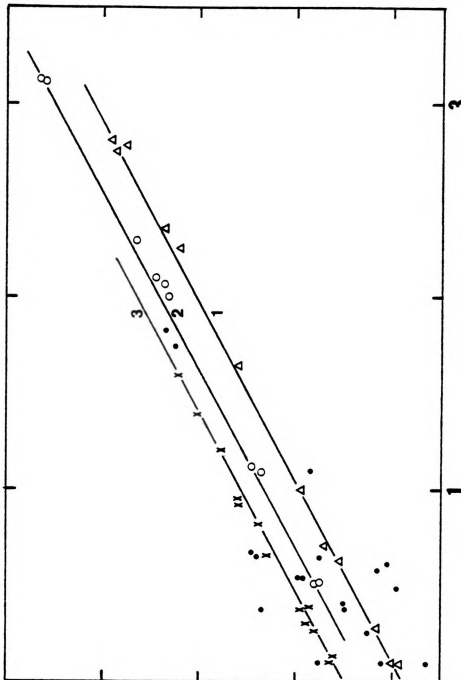

Figure E3 ρ vs. T^3: ρ_o shifts

The most likely source for these apparent shifts in ρ_o is the rather nebulus interface between the sample and the electrical leads mediated by the gold paste. It is not too unreasonable to believe that the contact area between the relatively low resistivity of the gold paste and the relatively high resistivity of the sample could change over time or because of stresses and strains caused by temperature cycling, thus changing in effect, the sample's effective size by a small amount.

In support of this idea is the observation that the largest δ's occur quite generally early in the experimental runs relatively near the He transfer as shown by the data in Figure E1 between 10 a.m. and 12 p.m. (10 a.m. is ~one hour and 20 minutes after the He transfer.) Also in support, a significant change in contact resistance was observed during the run of sample TS-40 B1 where a contact became quite resistive twice during the run and was restored by passing ~5 mA through the sample. This may account for the relatively larger "scatter" in the resistivity data for TS-40 B1.

This idea can be tested on a semi-quantitative basis by considering the change in the measured resistance of a planar specimen of area D^2 having a small zero resistant contact placed on its surface, effectively shorting out an area d^2. The change in the measured resistivity of this ficticous sample because of the contact would be[41]

$$\frac{\Delta\rho}{\rho} \simeq \left(\frac{d}{D}\right)^2 \frac{1}{\ell n 2}$$

This means that in order to produce changes of 0.2 to 0.4% (as seen in our $Ti_{1+x}S_2$ measurements) d/D would have to be 3.7 to 5.3%. However, for our $Ti_{1+x}S_2$ samples, the entire contact area amounted to only ~4

to 8% of the sample area. This means that to see changes in ρ_0 of 0.2 to 0.4%, 50 to 100% of the contact area must change, which is very unrealistic.

Also in opposition to the idea that contact area changes are the source of the non-zero δ's is the remarkable tracking with temperature excursions that δ maintains in the time periods 12 p.m. to 1:30 p.m. and 5 p.m. to 7 p.m.--it is just hard to imagine that changing contact areas could respond that consistently to such small temperature changes.

Even with these opposing arguments, we feel that the contacts are the most likely source for these apparent shifts in ρ_0 that occur over the duration of our experimental runs. Until the cause of these shifts are found, it will be useless to try to refine our measurements by either going lower in temperature or by improving our measurement precision.

APPENDIX F

$\rho(B)$ OF $Ti_{1+x}S_2$

In this appendix, we present our results for the magnetoresistivity of $Ti_{1+x}S_2$ in complete detail. Our results for samples TS-11 B164, TS-39 B164, TS-41 B6, and TS-40 B1 are shown in Figures F1-F4 respectively, where plotted aginst the field strength is the field dependence ρ_B of ρ, defined to be

$$\rho_B(T) = \rho(B,T) - \rho(B = 0,T) .$$

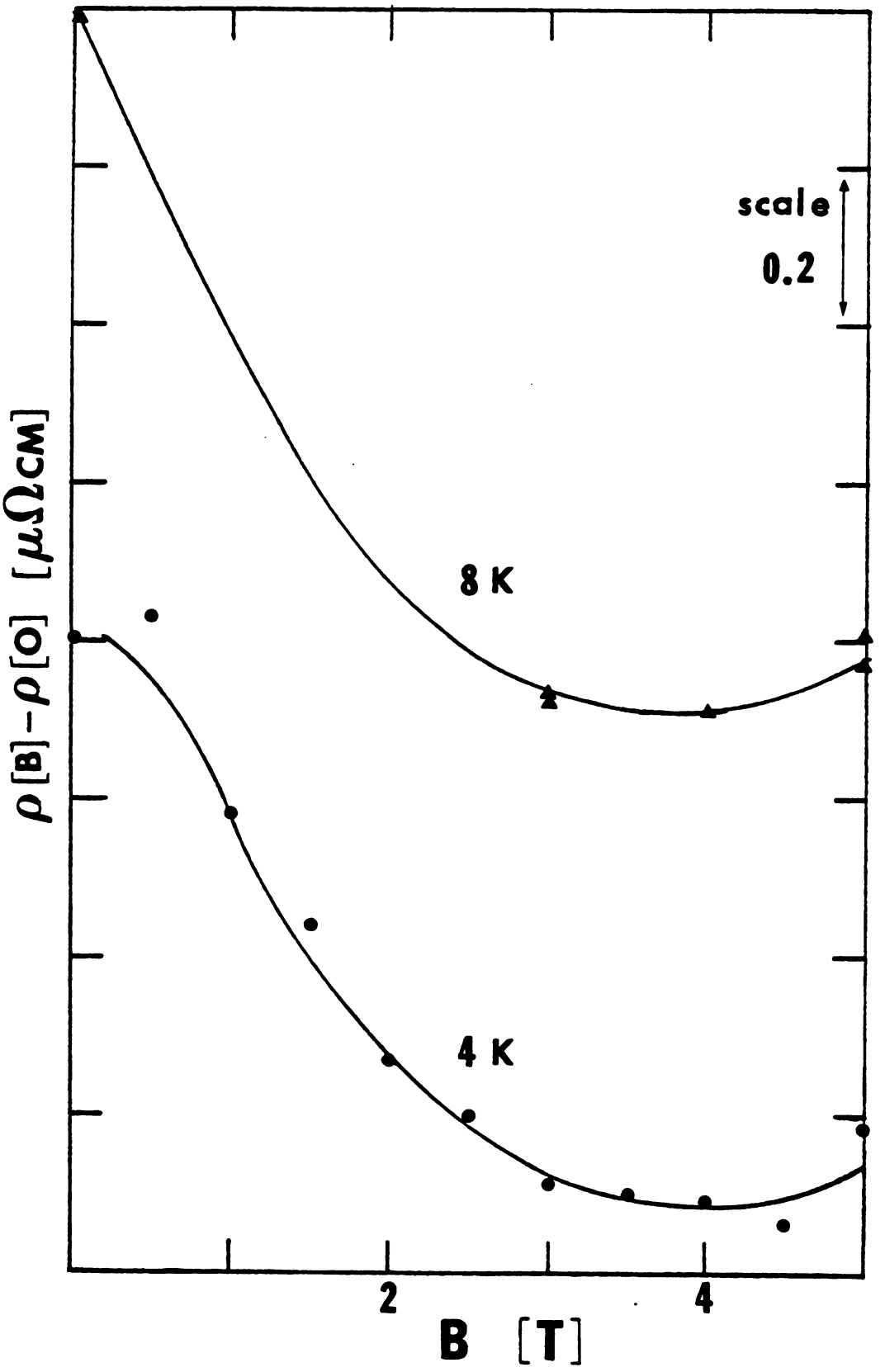

Figure F1 $\rho_B(T)$ for TS-11 B164

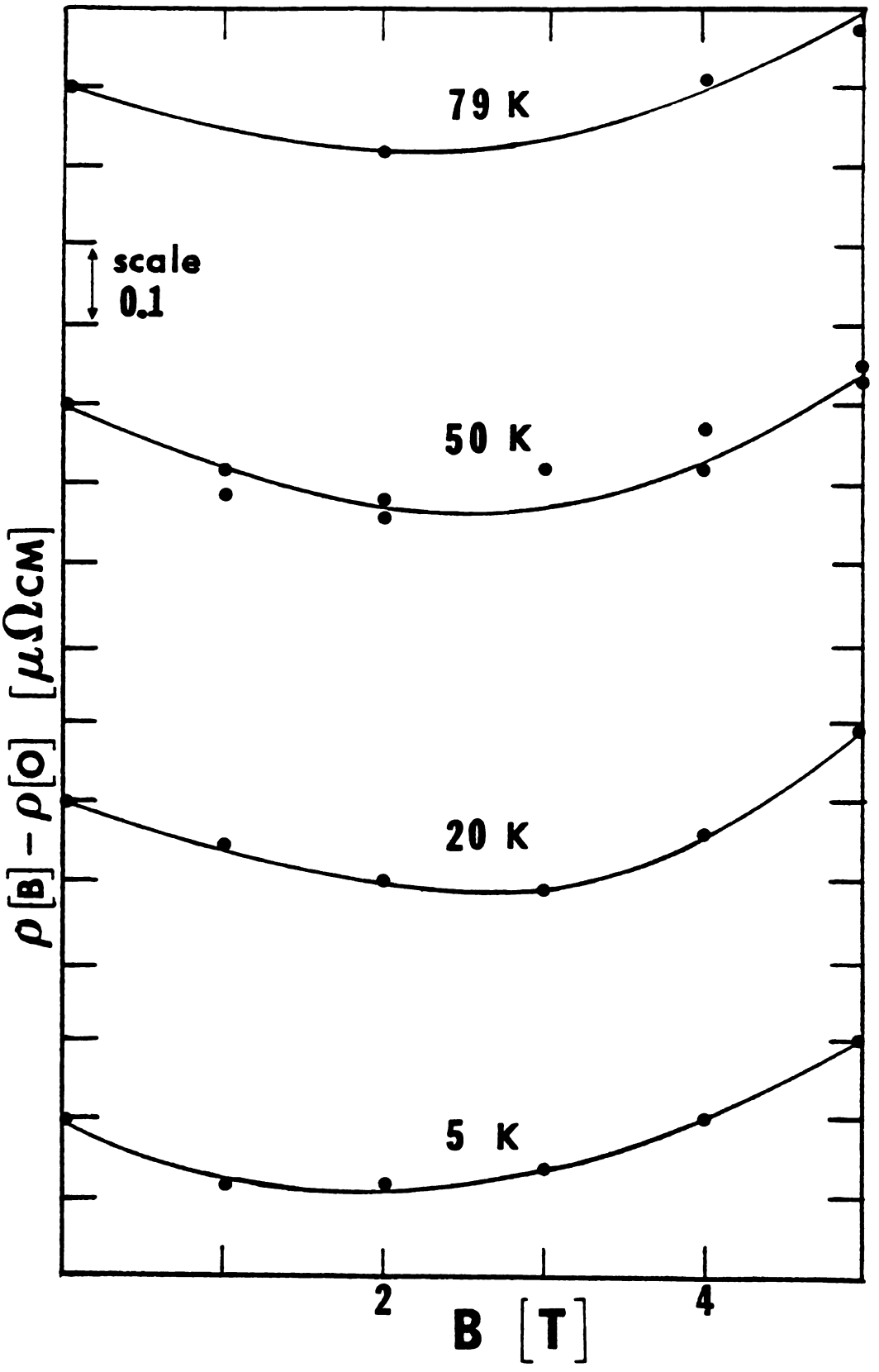

Figure F2 $\rho_B(T)$ for TS-39 B164

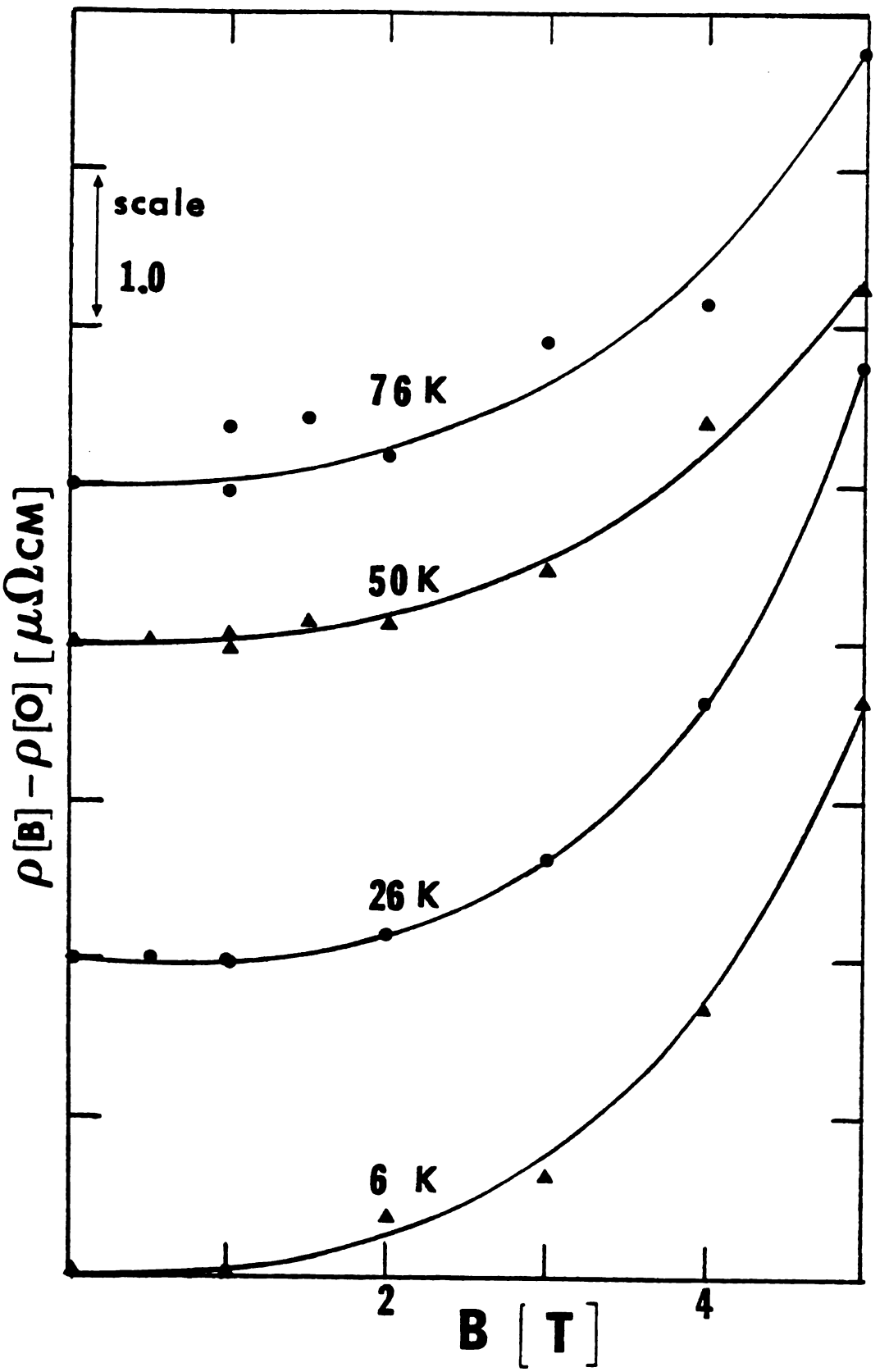

Figure F3 $\rho_B(T)$ for TS-41 B6

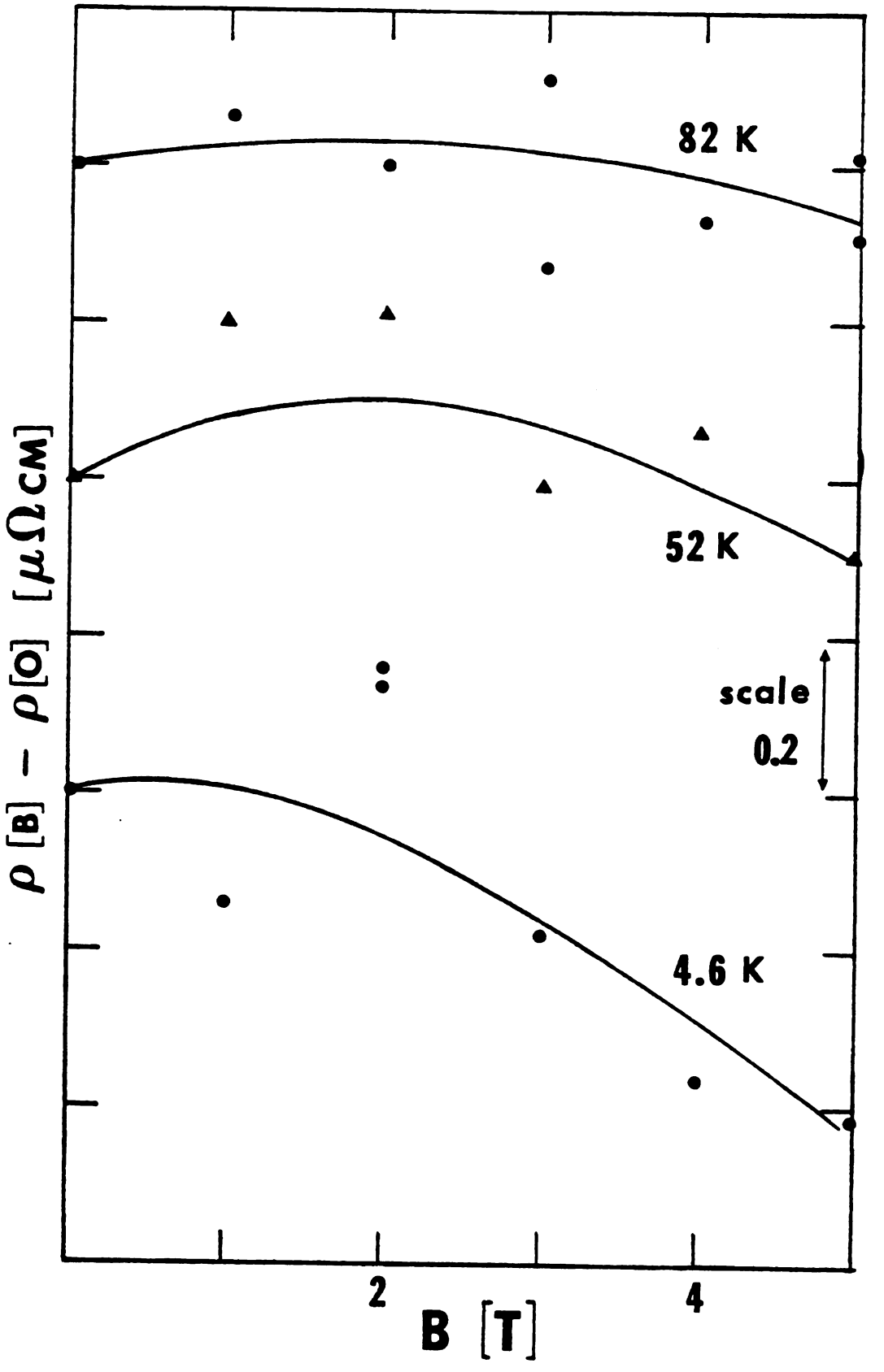

Figure F4 $\rho_B(T)$ for TS-40 B1

APPENDIX G

ELECTRICAL RESISTIVITY OF Al BELOW 1 K

In this appendix, we present the preliminary results of our investigation of the electrical resistivity of Al over the temperature range of ~0.08 to 4 K.

1. Introduction

In recent years, several observations at low temperatures of T^2 behavior of the electrical resistivity of the metals K,[43] Ag,[44] Cu,[45] and Al [46] have been reported as evidence for electron-electron scattering. One of the most recent studies of Ribot et al.[46] presented convincing evidence that the T^2 behavior in Al was due to electron-electron scattering by showing it to be independent of the residual resistivity of their samples. However, the temperature range over which this T^2 behavior was observed was very small. As in other systems, one must go to low temperatures to avoid electron-electron scattering contributions to the resistivity and since Al goes superconducting, one must stay above its superconducting transition temperature T_c. Thus investigations of electron-electron scattering in Al are restricted to the temperature range of 1.196 to ~2 K.

We believed that it might be possible to extend resistivity measurements of metals down below their superconducting transition temperatures

by destroying the superconducting state with a small applied magnetic field. We chose to study Al primarily because it has a low critical field (99 Gauss) which implies that measurements below T_c in small magnetic fields might be straightforwardly extrapolated to the zero field limit. Thus it was our hope to be able to investigate whether the T^2 behavior seen in Al extends down to our lowest obtainable temperature of ~0.08 K.

2. Experimental Technique

A. Al Sample

The Al sample was spark-cut from a block of polycrystalline stock which was represented as having a nominal resistance ratio of 13,000 by Cominco American Inc. (The sample was cut from a section which had no grain boundaries visible, so our sample may have been a single crystal.) The die for the spark-cutter was made by cutting 0.020" slots in a block of brass into which pieces of 0.020" stainless steel shim stock were soldered. The dimensions of the Al sample are shown in Figure G1. Current and potential leads were soldered to the Al sample using special solder from the Indium Corporation of America.* The residual resistance ratio (ρ(300 K)/ρ(4.2 K)) of the sample was measured to be 9,900.

B. Cryostat

The sample was soldered, via its center arm to minimize any thermopower generated emf's, to a copper support which could be inserted into a superconducting solenoid designed by J. Rowlands. To provide good

*Indalloy Solder #6, Indalloy Flux #3.

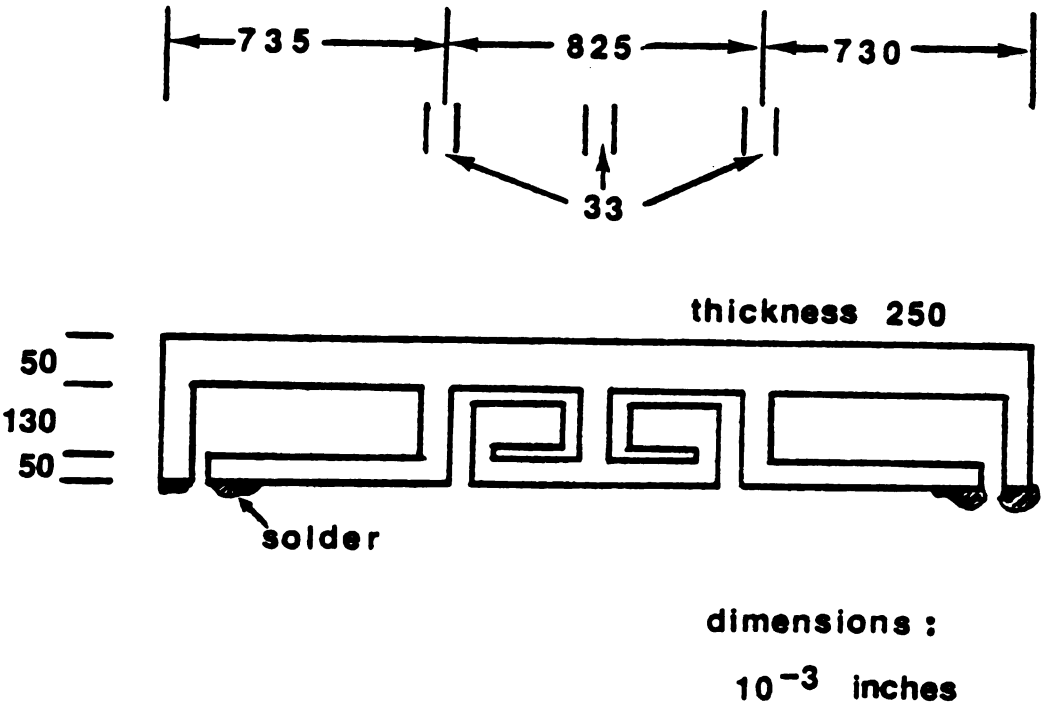

Figure G1 Al Sample

thermal conduction between the support and the sample, a special solder (Cd 82.5%, Zn 17.5%) was used which has a low superconducting transition temperature (estimated to be ~0.55 K). The magnet, sample and support structure are shown in Figure G2.

In our measurements, the magnet was operated in a persistent current mode using the persistent current switch attached to the magnet. This switch consisted of a free standing piece of NbTi wire shorting out the magnet. Superconducting connections were made by pressing the switch leads and the magnet leads against a block of NbTi using a washer coated with Pb-Sn solder. A current of ~0.6 mA through the heater (~400 Ω), made of Evanohm wire and wrapped directly on the NbTi wire, was sufficient to open the switch. The calibration of the magnet was made by noting that the critical current I_c needed to drive the Al sample normal was found to be $I_c = 0.1429 \pm 0.0002$ Amps at a temperature of 0.649 K. Assuming the critical field depends upon temperature with the form

$$B_c(T) = B_c(0)(1 - (T/T_c)^2)$$

where $B_c(0) = 99 \pm 1$ Gauss, the conversion factor for the magnet is 489 Gauss/Amp. (An "infinitely long solenoid" calculation gave an estimated value of 550 Gauss/Amp).

The entire magnet assembly was mountable into a dilution refrigerator designed by W. P. Pratt, Jr.[47] The magnet was supported from the mixing chamber using a support structure made of stainless steel tubing with a 50 μΩ multistrand filament of Ag wires providing the thermal link between the magnet and the refrigerator.

The measurement system and the measurement technique used are described in detail in the paper of Edmunds et al.[48] The measurements

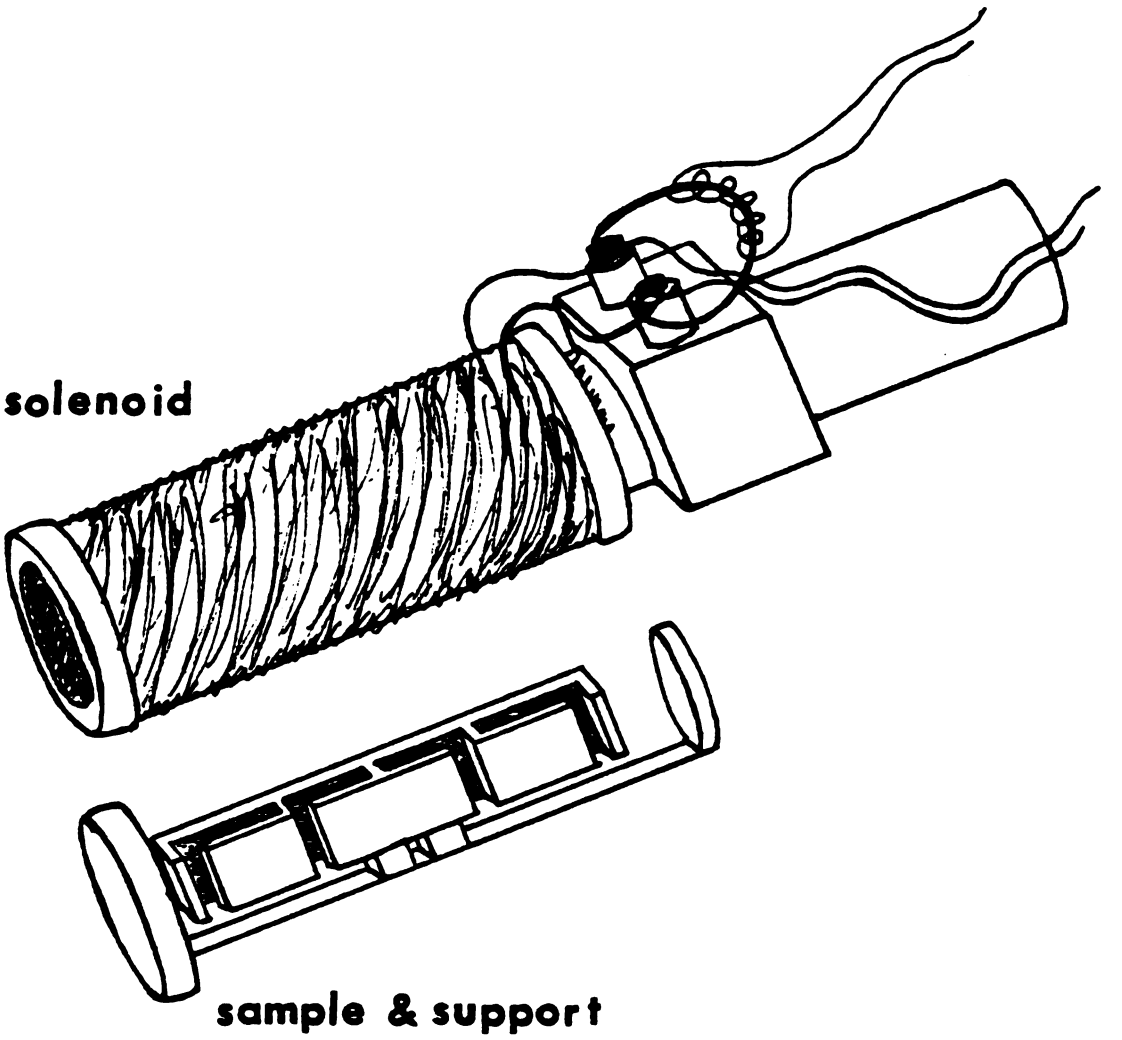

Figure G2 Solenoid and Sample

were made in the form of $\left(\frac{1}{\rho}\right)\frac{\Delta\rho}{\Delta T}$ where the difference in temperature ΔT is calculable using the Wiedemann-Franz law. ΔT can be determined from knowing the power used to raise the temperature of the sample and knowing the resistance of the thermal link, provided all the heat current flows through the heat link. Our calculations indicated that this last condition would be met because, at 2 K, the thermal conductance of the support structure is only ~1% of that of the thermal link. The calculated values of ΔT at ~2 K were within 5% of the experimentally measured values obtained using a germanium resistor attached to the magnet. Therefore, for our results using the dilution refrigerator, errors attributable to the ΔT calculations are ~5% at 2 K and become progressively smaller at lower temperatures.

Prior to the experiments conducted in the dilution refrigerator, some feasibility studies were conducted in a cryostat designed by S. D. Steenwyk.[49] This system was capable of making resistivity measurements directly, rather than its derivative, over the temperature range of ~1.0 to 4.2 K.

3. Results and Discussion

Our higher temperature results for the electrical resistivity of our Al sample at various magnetic field strengths are shown in Figure G3 where ρ is plotted against the square of the temperature. (The $T^2 = 0$ intercept of each field plot is completely arbitrary.) These results show that the T^2 behavior can only be the dominate temperature dependence below ~2 K.

Shown in Figure G4 are our lowest temperature results using the Steenwyk cryostat where we have plotted ρ against T^2 for temperatures

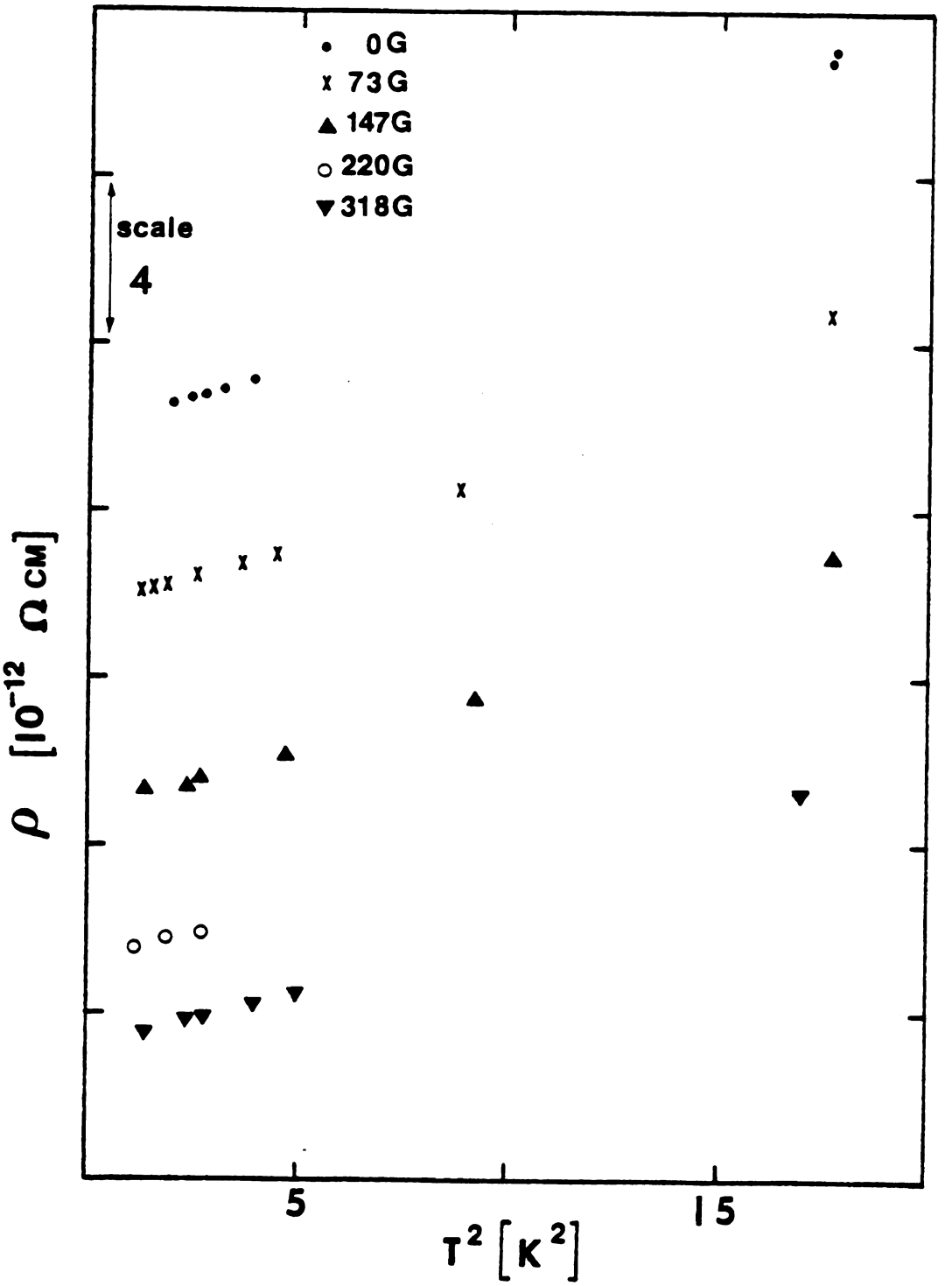

Figure G3 ρ vs. T^2

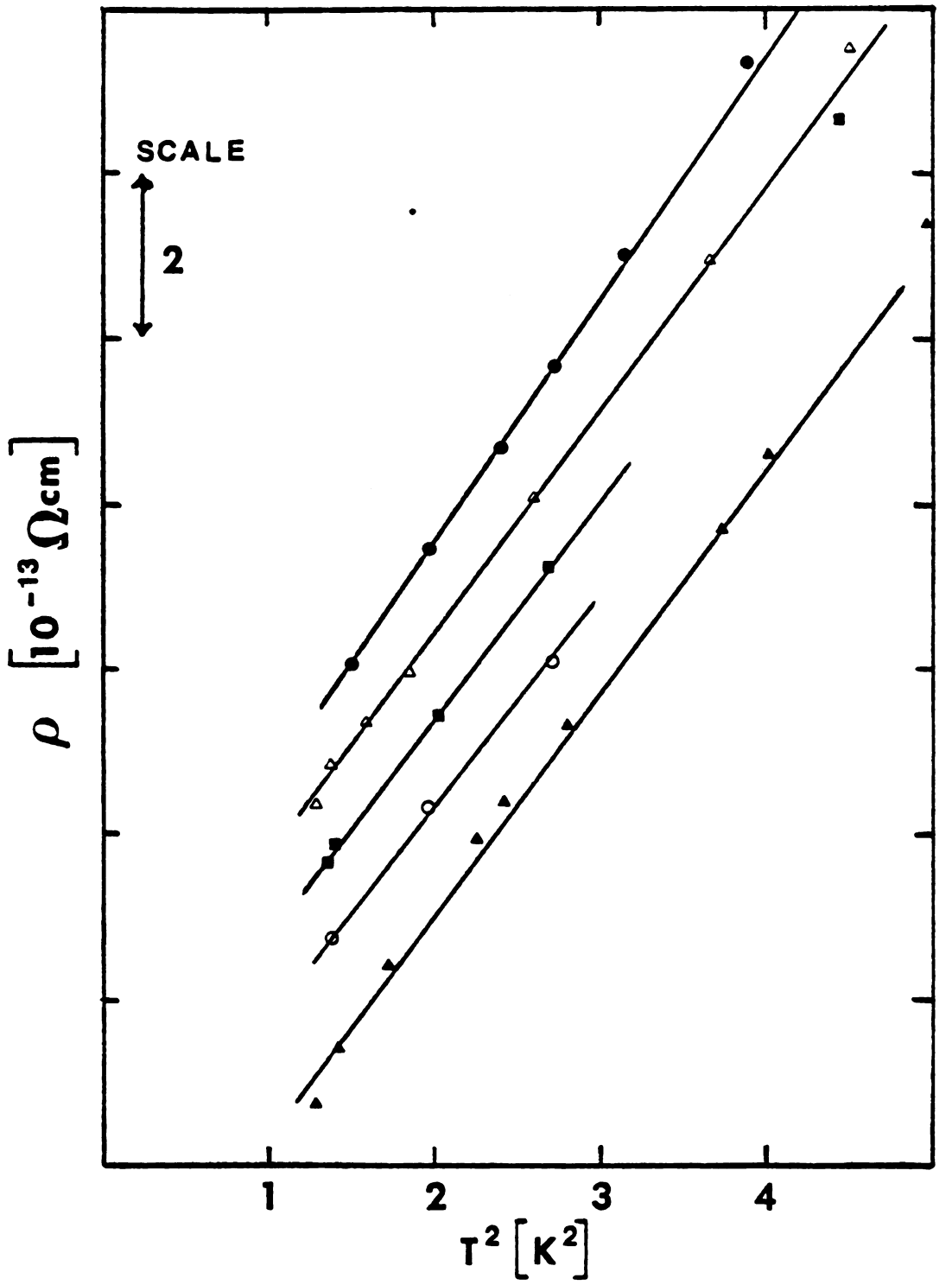

Figure G4 ρ vs. T^2 below 2.2 K

below ~2.2 K. (Again, the $T^2 = 0$ intercepts are arbitrary.) In this regime, the dominant form of the resistivity is

$$\rho \simeq \rho_0 + AT^2 \qquad (G1)$$

Our values for the coefficients ρ_0 and A are listed in Table G1.

The magnetic field dependence of the T^2 coefficient is shown in Figure G5. Our results for A, plotted against the magnetic field strength B, are internally consistent and show a negative magnetic field dependence. (The data point for B = 0.293 kG is taken from our results using the dilution refrigerator presented later.) Our results are also consistent with the zero field value for A of $2.9 \pm 0.1 \times 10^{-13}$ Ωcm K^{-2} given by Ribot et al.[46]

For completeness, we present in Figure G6 our results for the magnetoresistivity (longitudinal) of our Al sample, plotted against the field strength for various temperatures, including the results at zero temperature given by the values of ρ_0 in Table G1.

Table G1. $\rho = \rho_0 + AT^2$ Fits

B(Gauss)	$\rho_0(10^{-10}$ Ωcm)	$A(10^{-13}$ Ωcm $K^{-2})$
0	2.460	2.93
73	2.699	2.70
147	3.049	2.66
220	3.393	2.56
318	3.791	2.71

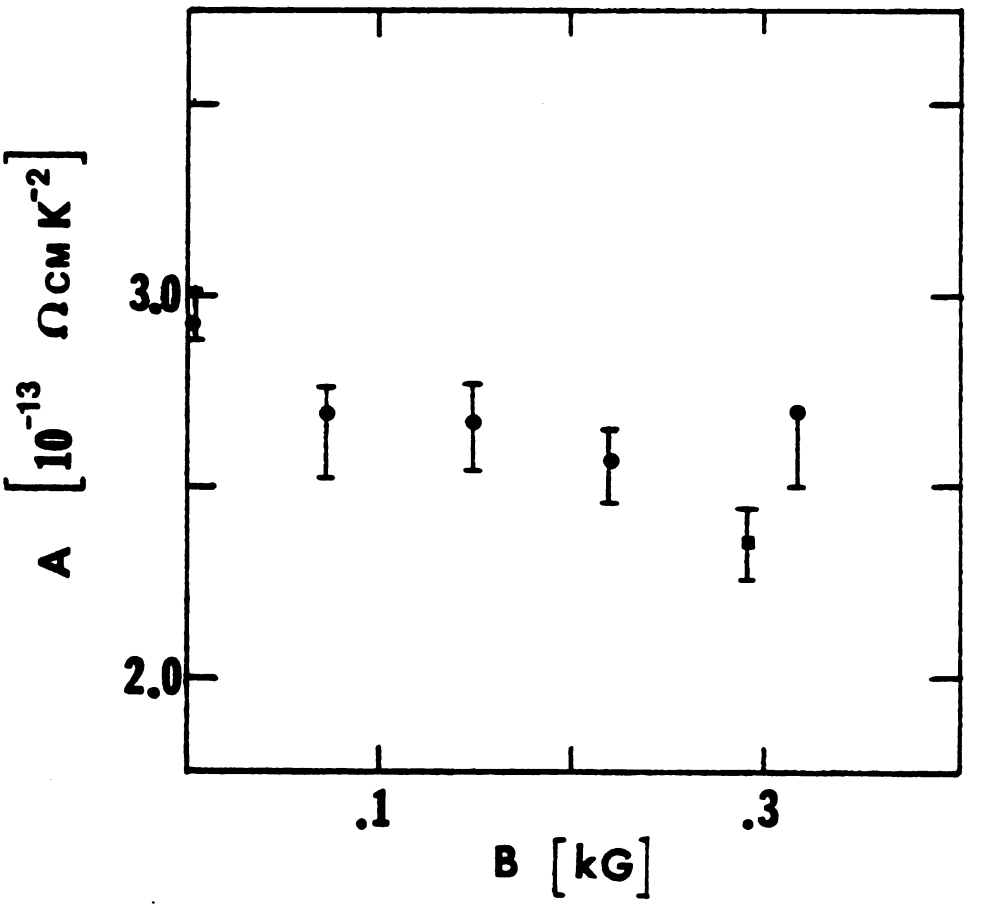

Figure G5 A vs. B

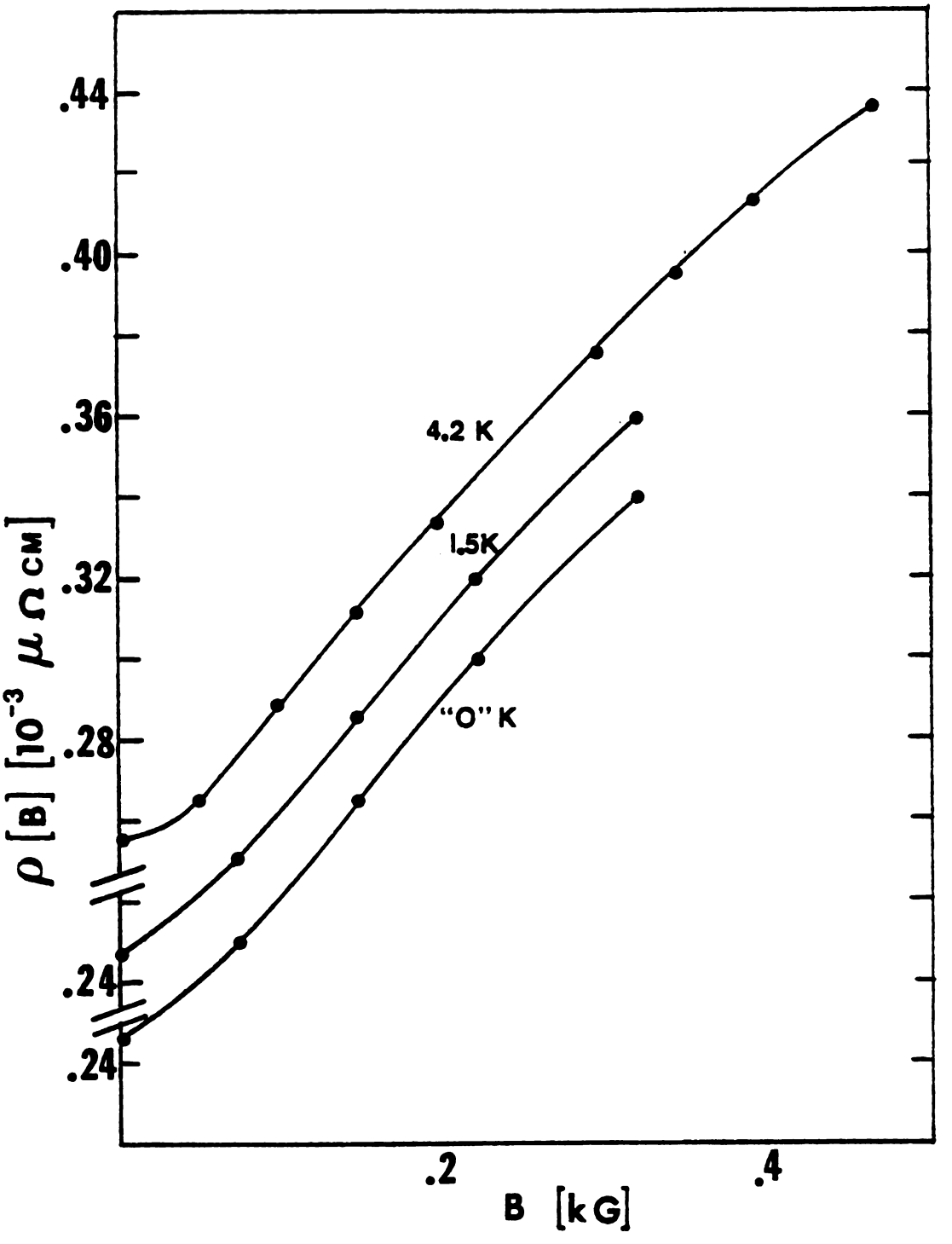

Figure G6 ρ vs. B

Encouraged by these results, we mounted the magnet assembly into the dilution refrigerator and continued our investigation to lower temperatures. Our results for a field of 293 G are shown in Figure G7 where plotted against T is our data in the form $\left(\frac{1}{\rho}\right)\frac{\Delta\rho}{\Delta T}$. For this largest field that we used, we find a continuation of the T^2 behavior in the resistivity down to ~0.2 K. However, the results for all smaller fields show anomolous behavior at low temperatures as can be seen in Figure G8. From this composite graph of all our data, we see deviations from a largely T^2 behavior at temperatures below ~0.9 K even though these fields are well above the zero temperature critical field of 99 G.

Summation

We have shown that for one sample and for one magnetic field strength of 293 G, that the T^2 behavior seen by Ribot et al.[46] in Al and attributed to electron-electron scattering extends down to ~0.2 K. We have also shown that the magnetic field dependence of the T^2 coefficient is negative and is ~-0.07% G/Amp over the field range of 0 to 300 G. This field dependence may prove to be another check on whether the T^2 behavior seen in Al is due to electron-electron scattering once a theoretical prediction for its dependence becomes known.

As stated earlier, these results are still considered tentative, not only because they are for a single sample but also because of the "funny" behavior observed in the resistivity for fields below 293 G. The next step in this investigation is to study another Al sample at these lower temperatures, which has a completely different geometry, as a check on which behavior is reproducible.

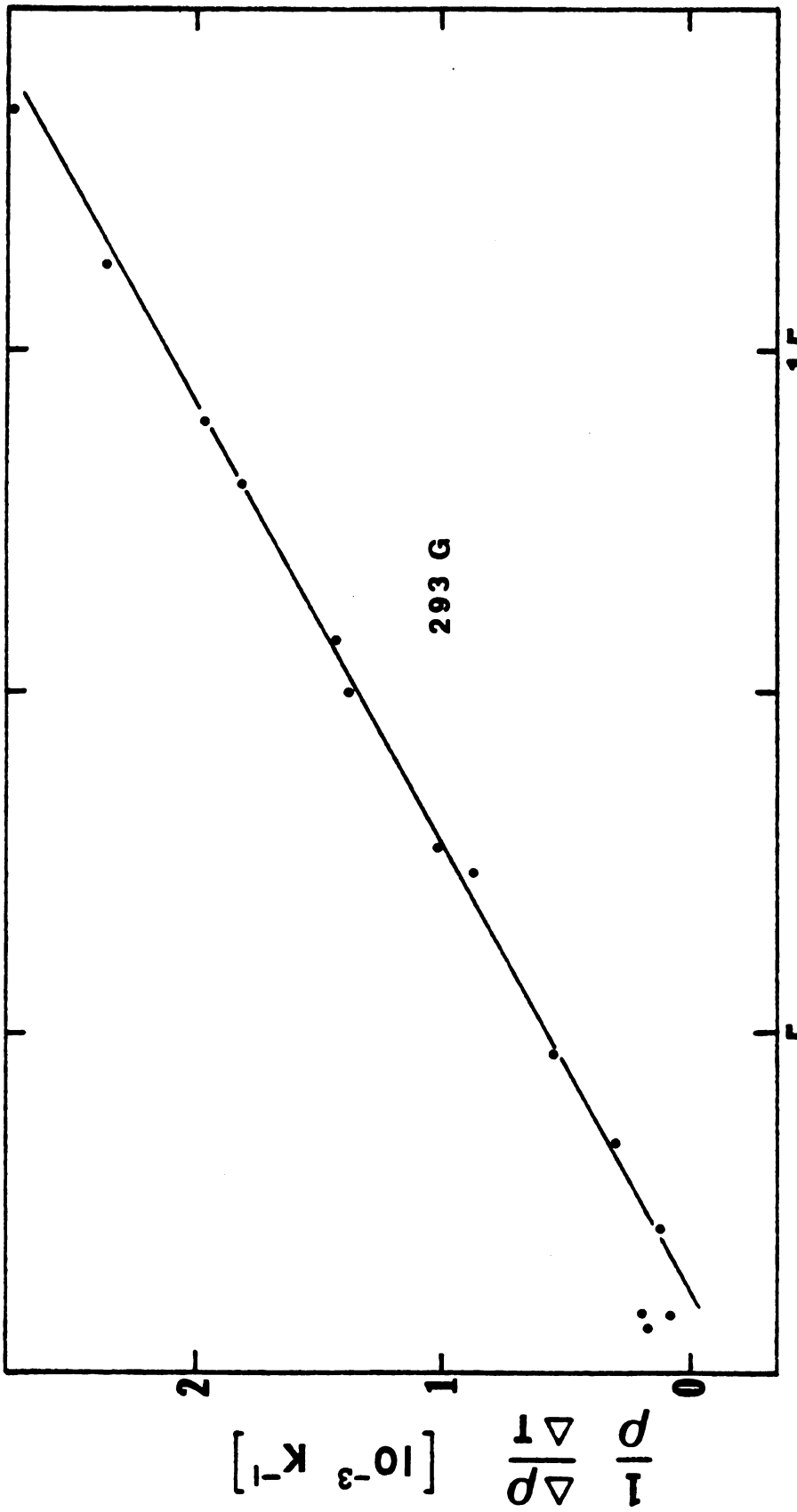

Figure G7 $\left(\frac{1}{\rho}\right)\frac{\Delta\rho}{\Delta T}$ vs. T at 235 G

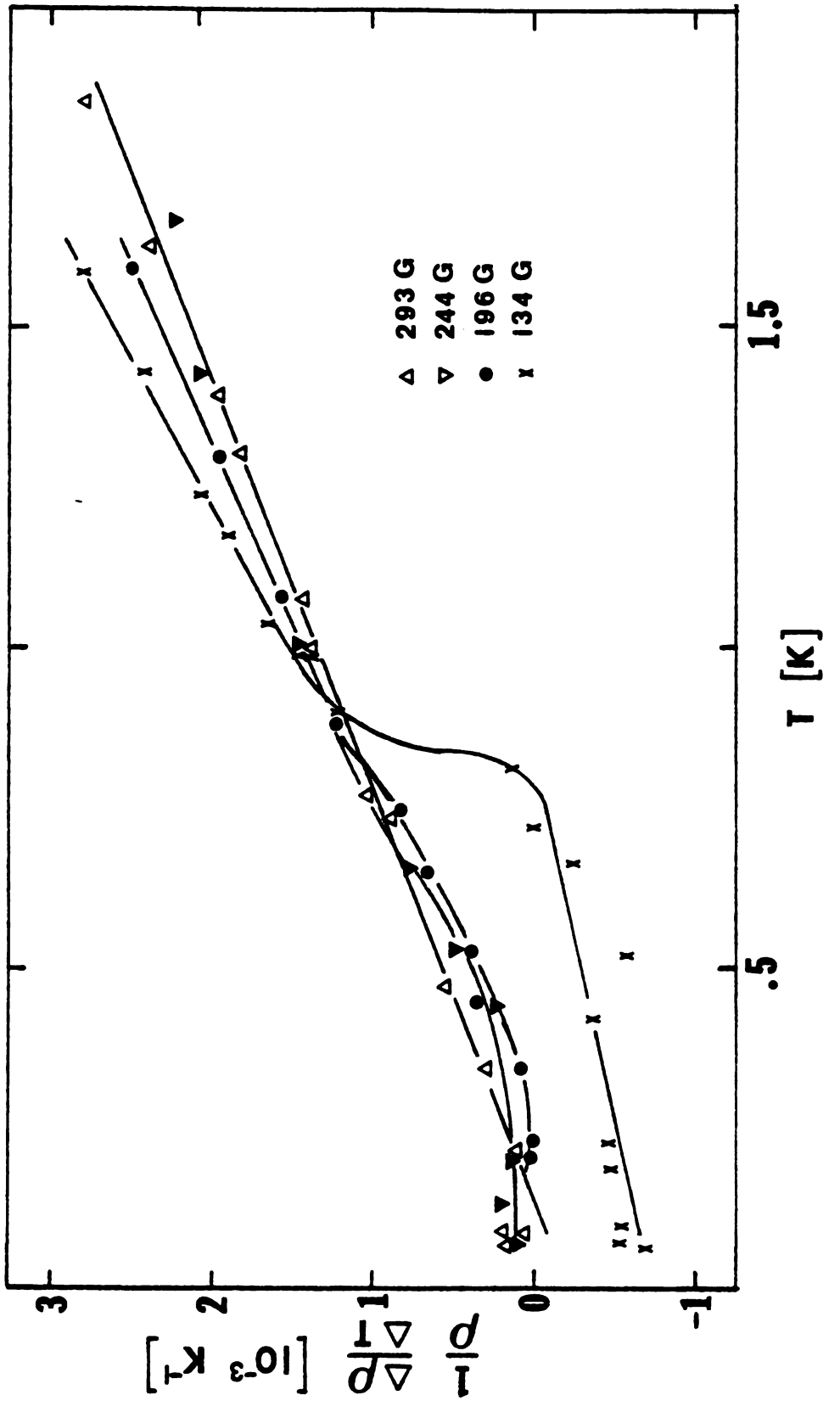

Figure G8 $\left(\frac{1}{\rho}\right)\frac{\Delta\rho}{\Delta T}$ vs. T at all fields

REFERENCES

REFERENCES

1. R. Fletcher, J. L. Opsal and B. J. Thaler, J. Phys. F 7, 1489 (1977).
2. I. M. Lifshitz, M. Ia. Azbel and M. I. Kaganov, Sov. Phys. JETP 4, 41 (1957).
3. I. M. Lifshitz, M. Ia. Azbel and M. I. Kaganov, Sov. Phys. JETP 5, 967 (1957).
4. R. Fletcher, J. Low Temp. Phys. 22, 39 (1976).
5. R. Fletcher, Phil. Mag. 32, 565 (1975).
6. R. J. Douglas and R. Fletcher, Phil. Mag. 32, 73 (1975).
7. J. M. Ziman, Electrons and Phonons (Oxford, 1960).
8. Frank J. Blatt, Physics of Electronic Conduction in Solids (McGraw-Hill, 1968).
9. R. S. Averback and D. K. Wagner, Solid State Commun. 11, 1109 (1972).
10. Techniques of Metals Research, Vol. 1, p. 1343, Techniques of Materials Preparation and Handling--Part 3, Ed. R. F. Bunshah (John Wiley and Sons, 1968).
11. A. C. Anderson, Rev. Sci. Instr. 39, 605 (1968).
12. J. R. Pernicone, Ph.D. Thesis, Michigan State University, 1973, p. 14.
13. L. Neuringer and Y. Shapira, Rev. Sci. Inst. 40, 1314 (1969).
14. J. R. Clement and E. H. Quinnel, Rev. Sci. Inst. 23, 213 (1952).
15. G. J. Edwards, J. Phys. E 4, 299 (1971).
16. R. Fletcher and M. R. Stinson, J. Phys. E 12, 92 (1979).

17. J. J. Higgins, Ph.D. Thesis, Michigan State University, 1977.

18. N. W. Ashcroft and N. D. Mermin, Solid State Physics (Holt, Rinehart and Winston, 1976) p. 268.

19. R. F. Girvan, A. V. Gold and R. A. Phillips, J. Phys. Chem. Solids 29, 1485 (1968).

20. D. M. Sparlin and J. A. Marcus, Phys. Rev. 144, 484 (1966).

21. M. S. Wittingham, Science 192, 1126 (1976).

22. F. K. McTaggert and A. B. Wadsley, Aust. J. Chem. 11, 445 (1958).

23. D. L. Greenway and R. Nitsche, J. Phys. Chem. Solids 26 1445 (1965).

24. S. Takeuchi and H. Katsuta, J. Jap. Inst. Metals 34, 758 (1970); and J. Jap. Inst. Metals 34, 764 (1970).

25. A. H. Thompson, F. R. Gamble and C. R. Symon, Mat. Res. Bull. 10, 915 (1975).

26. A. H. Thompson, Phys. Rev. Letters 35, 1786 (1975).

27. W. E. Lawrence and J. W. Wilkins, Phys. Rev. B 7, 2317 (1973).

28. Carl A. Kukkonen and Pierre F. Maldague, Phys. Rev. Letters 37, 782 (1976).

29. R. B. Murray and A. D. Yoffe, J. Phys. C 5, 3038 (1972).

30. H. W. Myron and A. J. Freeman, Phys. Rev. B 9, 481 (1974).

31. A. Zunger and A. J. Freeman, Phys. Rev. B 16, 906 (1977).

32. F. R. Sheperd and P. M. Williams, J. Phys. C 7, 4416 and 4427 (1974).

33. G. K. Wertheim, F. J. DiSalvo and D.N.E. Buchanan, Solid State Commun. 13, 1225 (1973).

34. C. H. Chen, W. Fabian, F. C. Brown, K. C. Woo, B. Davies, B. DeLong and A. H. Thompson, Phys. Rev. B 21, 615 (1980).

35. R. H. Friend, D. Jérome, W. Y. Liang, J. C. Mikkelsen and A. D. Yoffe, J. Phys. C 10, L705 (1977).

36. J. A. Wilson, Solid State Commun. 22, 551 (1977).

37. J. A. Wilson, Phys. Stat. Solidi 86, 11 (1978).

38. R. Fivaz, J. Phys. Chem. Solids 28, 839 (1967).

39. R. Fivaz and E. Mooser, Phys. Rev. 163, 743 (1967).

40. Carl A. Kukkon, E. M. Logothetis, W. J. Kaiser, B. J. Blumenstock, P. A. Schroeder, S. P. Faile, R. Colella and J. Gambold, (to be published).

41. L. J. van der Pauw, Philips Res. Repts. 13, 1 (1958).

42. R. P. Khosla and J. R. Fischer, Phys. Rev. B 2, 4084 (1970).

43. J. A. Rowlands, C. Duvvury and S. B. Woods, Phys. Rev. Letters 40, 1201 (1978).

44. M. Khoshnevisan, W. P. Pratt, Jr., P. A. Schroeder, S. D. Steenwyk and C. Uher, J. Phys. F 9, L1 (1979).

45. M. Khoshnevisan, W. P. Pratt, Jr., P. A. Schroeder and S. D. Steenwyk, Phys. Rev. B 19, 3873 (1979).

46. J.H.J.M. Ribot, J. Bass, H. van Kempen and P. Wyder, J. Phys. F 9, L117 (1979).

47. W. P. Pratt, Jr., C. Uher, P. A. Schroeder and J. Bass, "Thermoelectric Measurements at Millikelvin Temperatures", Thermoelectricity in Metallic Conductors, Eds. Frank J. Blatt and Peter A. Schroeder (Plenum Press, New York, 1978) p. 265.

48. D. L. Edmunds, W. P. Pratt, Jr. and J. A. Rowlands, Rev. Sci. Inst. 1980 (in press).

49. S. D. Steenwyk, Ph.D. Thesis, Michigan State University, 1980.